Force required for endocytic vesicle formation analyzed by FRET-based force sensors

Dissertation

zur Erlangung des Doktorgrades

der Naturwissenschaften

(Dr. rer. nat.)

des Fachbereichs Biologie
der Philipps-Universität Marburg

vorgelegt von

Marc Abella Guerra

aus Barcelona, Spanien

Marburg, Oktober 2020

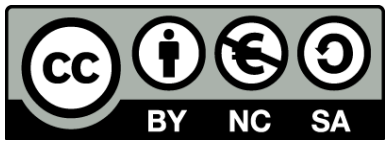

Die vorliegende Dissertation wurde von März 2017 bis Oktober 2020 am Max-Planck-Institut für terrestrische Mikrobiologie unter Leitung von Prof. Dr. Victor Sourjik angefertigt.

Vom Fachbereich Biologie

der Philipps-Universität Marburg (Hochschulkennziffer 1180)

als Dissertation angenommen am 26.11.2020

Erstgutachter: Prof. Dr. Victor Sourjik

Zweitgutachter: Prof. Dr. Roland Lill

Weitere Mitglieder der Prüfungskommission:

Prof. Dr. Uwe Maier

Dr. Michal Skruzny

Tag der Disputation: 11.12.2020

Erklärung

Ich versichere, dass ich meine Dissertation mit dem Titel

Force required for endocytic vesicle formation analyzed by FRET-based force sensors

selbstständig und ohne unerlaubte Hilfe angefertigt und ich mich dabei keiner anderen als der von mir ausdrücklich bezeichneten Quellen und Hilfsmittel bedient habe.

Diese Dissertation wurde in der jetzigen oder einer ähnlichen Form noch bei keiner anderen Hochschule eingereicht und hat noch keinen sonstigen Prüfungszwecken gedient.

Marburg, den 2. Oktober 2020

Marc Abella Guerra

Zum Zeitpunkt der Einreichung dieser Dissertation wird die folgende Originalpublikation vorbereitet, um die erzielten Ergebnisse zu veröffentlichen:

Abella M, Andruck L, Malengo G, Skruzny M. Force requirements of endocytic vesicle formation (submitted).

Weitere Veröffentlichungen:

Skruzny M, Pohl E, **Abella M** (2019). FRET microscopy in yeast. Biosensors (Basel). 9(4), 122.

Lizarrondo J, Klebl D, Niebling S, **Abella M**, Schroer MA, Mertens HD, Veith K, Svergun DI, Skruzny M, Sobott F, Muench S, Garcia-Alai M. Structure of the endocytic adaptor complex reveals the basis for efficient membrane anchoring during clathrin-mediated endocytosis (Nature Communications in review).

A la meva família i amics.

TABLE OF CONTENTS

SUMMARY **15**

ZUSAMMENFASSUNG **17**

INTRODUCTION **19**

Introduction to clathrin-mediated endocytosis 19

Initiation of endocytosis *21*

Maturation of the endocytic coat *22*

The actin cytoskeleton and clathrin-mediated endocytosis *23*

Mechanisms of membrane bending and vesicle scission during endocytosis *26*

Other membrane-remodeling factors *28*

Molecular basis for force transmission during endocytosis 29

Measuring force transmission during endocytosis by FRET-tension sensors *30*

RESULTS **35**

Construction and verification of Sla2 force sensor strains 35

Force of approx. 10 pN is transmitted over Sla2 protein during actin-driven endocytic vesicle formation 38

Contribution of individual endocytic proteins to endocytic force transmission 43

Modification of the physical conditions can alter the force required for endocytosis 47

DISCUSSION **55**

Measurement of actin-generated forces transmitted via Sla2 protein 55

Contribution of endocytic proteins to force generation and transmission 59

Role of physical conditions in endocytic force requirements 61

FRET-based endocytic force measurement limitations and project future directions 63

Concluding remarks 65

MATERIALS AND METHODS **67**

Yeast strains and plasmids 67

PCR protocols *69*

Recombinant DNA *70*

Preparation of competent E. coli cells *71*

Yeast transformation *71*

Microscopy 72

Ratiometric FRET *72*

Live-cell imaging *73*

Acceptor photobleaching FRET *73*

Statistics and reproducibility 74

REFERENCES.....**84**

SUPPLEMENTARY MATERIAL **93**

SUMMARY

Mechanical forces exerted by multiprotein machines are essential for many cellular processes. One of the best-studied examples is membrane reshaping during clathrin-mediated endocytosis, a principal vesicle trafficking route responsible for molecular uptake, signaling, and membrane homeostasis. During endocytosis, a small area of the plasma membrane reshapes from a flat sheet to a closed vesicle. This reshaping requires mechanical force, which is provided by multiple endocytic proteins and actin polymerization. Several theoretical models have been proposed to describe force requirements of endocytosis (Lacy et al., 2018). However, to understand force-dependent endocytic vesicle formation, applied forces need to be analyzed *in vivo* to report real force values and key involved factors.

To achieve that, we used FRET (Förster Resonance Energy Transfer) tension sensors (Freikamp et al., 2016), which allow the measurement of forces in the range of piconewtons (pN) *in vivo*, and inserted them into the yeast protein Sla2. Sla2 is part of the essential Sla2-Ent1 (Hip1R-epsin 1-3 in human) protein linker transmitting force of the polymerizing actin cytoskeleton to the plasma membrane during endocytosis (Skruzny et al., 2012, 2015). We followed forces transmitted over Sla2 in real time during individual endocytic events and measured force of approx. 10 pN per Sla2 molecule, hence 450-1330 pN per endocytic event.

Next, we analyzed the role of the actin cytoskeleton and followed force transmission in cells absent of the negative regulator of actin polymerization Bbc1. Despite the enlarged endocytic actin cytoskeleton, less force was transmitted over the force sensor prior to vesicle scission. We propose that an excess of dense actin meshwork in *bbc1Δ* cells directly physically remodel the long invaginating membrane. Finally, force transmission was followed in cells missing BAR-domain protein Rvs167 during unsuccessful endocytic events characterized by initial membrane bending followed by retraction back to the flat membrane profile. Only force similar to force of early membrane bending in wild-type cells was observed. This suggests that stabilization of the deeply invaginated membrane provided by BAR-domain proteins is essential to facilitate productive force transmission around the time of vesicle scission.

In addition, we analyzed the role of physical conditions in force-dependent steps of endocytosis. First, we counteracted the high turgor pressure of the yeast cytoplasm by exposing cells to hypertonic conditions. We observed an overall decrease in the force required for membrane invagination. Similarly, we reduced plasma membrane tension by incorporation of soluble lipid into the membrane and again detected less force transmitted over the Sla2 force sensor. We also analyzed the capacity of the endocytic force-generating machinery in hypotonic conditions, which should increase cell turgor opposing endocytosis. We exposed cells to increasing osmotic shifts and observed an increase in number of arrested endocytic sites. When we followed force transmission of remaining completed endocytic events, we detected force similar to untreated cells. The observed endocytic block and unchanged force transmission suggest that the actin cytoskeleton can provide only limiting force for endocytosis.

We believe that our data will form a base of biomechanical model of endocytic vesicle formation, essential to understand how the endocytic machinery works in physiological and pathological conditions. Moreover, our data could be highly valuable for the understanding of other force-dependent membrane remodeling processes in the cell.

ZUSAMMENFASSUNG

Mechanische Kräfte, die von Multiproteinkomplexen ausgeübt werden, sind für viele zelluläre Prozesse unerlässlich. Eines der am besten untersuchten Beispiele ist die Membranumformung während der Clathrin-vermittelten Endozytose, einem Hauptweg des Vesikeltransports, welcher für die molekulare Aufnahme, Signalübertragung und Membranhomöostase verantwortlich ist. Während der Endozytose formt sich ein kleiner Bereich der Plasmamembran von einer flachen Oberfläche zu einem geschlossenen Vesikel um. Diese Einstülpung erfordert mechanische Kraft, welche durch verschiedene endozytotische Proteine und die Polymerisation von Aktin bereitgestellt wird. Bislang wurden verschiedene theoretische Modelle vorgeschlagen, um die Kraftanforderungen der Endozytose zu beschreiben (Lacy et al., 2018). Zum tiefgreifenden Verständnis der kraftabhängigen Bildung endozytotischer Vesikel müssen jedoch die angewandten Kräfte *in vivo* analysiert werden, um reale Kraftwerte und die wichtigsten beteiligten Faktoren zu ermitteln.

Um dies zu erreichen, haben wir FRET (Förster-Resonanzenergietransfer)-basierte Spannungssensoren (Freikamp et al., 2016) verwendet, welche die Messung von Kräften in der Größenordnung von Pikonewton (pN) *in vivo* erlauben, und diese in das Hefeprotein Sla2 eingefügt. Sla2 ist Teil des essentiellen Proteinlinkers Sla2-Ent1 (Hip1R-epsin 1-3 beim Menschen), der die Kraft des polymerisierenden Aktin-Zytoskeletts während der Endozytose auf die Plasmamembran überträgt (Skruzny et al., 2012, 2015). Durch Verfolgung der über Sla2 vermittelten Kräfte in Echtzeit während verschiedener endozytotischer Vorgänge konnten wir eine Kraft von ca. 10 pN pro Sla2 Molekül ermitteln, was in etwa 450-1330 pN pro endozytotischem Ereignis entspricht.

Im Anschluss analysierten wir die Rolle des Aktin-Zytoskeletts und verfolgten die Kraftübertragung in Zellen, in denen der negative Regulator der Aktin-Polymerisation Bbc1 abwesend war. Vor der Vesikelspaltung wurde in diesen Zellen trotz des vergrößerten endozytotischen Aktin-Zytoskeletts weniger Kraft über den Sensor übertragen. Wir schlagen vor, dass ein Überschuss an dichtem Aktingeflecht in *bbc1*Δ Zellen direkt die lange invaginierende Membran physikalisch umbildet. Zum Abschluss wurde die Kraftübertragung erfolgloser endozytotischer Ereignisse in Zellen verfolgt,

denen das BAR-Domänenprotein Rvs167 fehlte. Diese Ereignisse waren gekennzeichnet durch anfängliche Membrankrümmung und anschliessendes Zurückziehen auf ein

flaches Membranprofil. Die hier beobachtete gerringe Kraft war ähnlich derjenigen, die bei früher Membrankrümmung in Wildtyp-Zellen gemessen wurde. Dies deutet darauf hin, dass die Stabilisierung der tief invaginierten Membran durch BAR-Domänenproteine wesentlich ist, um eine effektive Kraftübertragung zum Zeitpunkt der Vesikelspaltung zu ermöglichen.

Weiterhin analysierten wir die Rolle physikalischer Bedingungen bei kraftabhängigen Schritten der Endozytose. Nach Erniedrigung des hohen Turgordrucks des Hefezytoplasmas, herbeigeführt durch Inkubation der Zellen in hypertonischem Medium, beobachteten wir eine allgemeine Abnahme der für die Membraninvagination erforderlichen Kraft. In ähnlicher Weise reduzierten wir die Spannung der Plasmamembran durch Einlagerung von löslichen Lipiden in die Membran und maßen wiederum eine geringere Kraft, die über den Sla2-Sensor übertragen wurde. Außerdem anaylsierten wir die Kapazität der endozytotischen krafterzeugenden Maschinerie unter hypotonen Bedingungen, welche den Zellturgor erhöhen und damit die Endozytose erschweren sollten. Hierzu setzten wir die Zellen einer Veränderung der osmotischen Bedingungen aus und beobachteten eine Zunahme von arretierten endozytotischen Ereignissen. Eine Analyse der Kraftübertragung der verbliebenen abgeschlossenen Endozytosen ergab Kräfte, welche vergleichbar zu unbehandelten Zellen waren. Die beobachtete partielle Blockierung der Endozytose und die unveränderte Kraftübertragung deuten darauf hin, dass das Aktin-Zytoskelett nur eine begrenzte Kraft für die Endozytose bereitstellen kann.

Unserer Ansicht nach werden unsere Daten als Grundlage für ein biomechanisches Modell der endozytischen Vesikelbildung dienen, welches für ein Verständnis der Funktionsweise der endozytischen Maschinerie unter physiologischen und pathologischen Bedingungen unerlässlich ist. Darüber hinaus könnten unsere Daten sehr wertvoll für das Verständnis anderer kraftabhängiger Membranumbauprozesse in der Zelle sein.

INTRODUCTION

Introduction to clathrin-mediated endocytosis

Clathrin-mediated endocytosis is the principal trafficking route from the plasma membrane to the cytoplasm. It is essential for many processes including hormone and nutrient uptake, recycling of plasma membrane components (e.g. after neurotransmission), and regulation of many cellular signaling pathways (McMahon and Boucrot, 2011). Moreover, some pathogens such as viruses use the endocytic machinery to reach the intracellular compartments for infection and replication (Cossart and Helenius, 2014).

During endocytosis, a small region of plasma membrane reshapes from an initially flat sheet to a closed vesicle transporting membrane constituents and extracellular molecules into the cell. This process is accomplished by the sequential, highly orchestrated assembly of ~50 different endocytic proteins at the endocytic site, which assemble following a highly regulated timing of typically 60-120 seconds. After successful membrane invagination and vesicle scission, endocytic proteins are shed of the vesicle and plasma membrane to be recycled for another round of endocytosis.

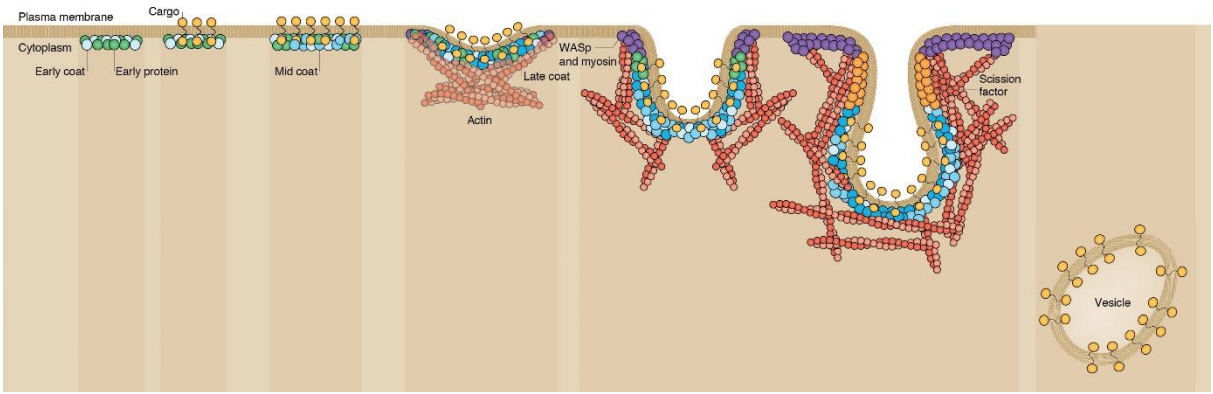

Figure 1 During endocytosis, a small region of plasma membrane reshapes from an initially flat sheet to a closed vesicle. The topology of main functional groups of endocytic proteins involved is indicated (adapted from Lu et al., 2016).

The endocytic machinery assembles at the endocytic site by recruitment of endocytic proteins present in the cytosol in a highly regular sequence in which proteins arrive and leave in a specific order and time. Based on their assembly dynamics and function,

endocytic proteins can be classified into several modules, although they interact within and between themselves to coordinate their assembly and functions.

Interestingly, recent superresolution imaging together with fluorescence microscopy and immunoelectron microscopy of the endocytic site in yeast found that these modules organize in different zones around the incipient vesicle according to their function (Idrissi et al., 2008; Idrissi et al., 2012; Picco et al., 2015; Mund et al., 2018). Besides, these functional modules are highly conserved among different organisms (Kaksonen and Roux, 2018).

The first protein module is the coat module or clathrin module. This module is responsible for initiation of endocytosis, cargo recruitment, and it is involved in the first steps of membrane bending in mammalian cells. Coat proteins initially assemble on the flat plasma membrane where they are thought to interact and concentrate extracellular cargo molecules. Some coat adaptors form a protein coat below the membrane that assists membrane reshaping and invagination, and provide the molecular scaffold for the other modules to be recruited to the plasma membrane at the endocytic site (e.g. proteins responsible to activate actin polymerization).

After the endocytic coat has assembled, actin polymerization initiates at the site of endocytosis. The actin module is essential for membrane bending and scission in yeast, and partially involved in mammalian cells. This second module can be divided into the actin cytoskeleton, and regulators of actin polymerization.

The third module is responsible for stabilizing the neck of the membrane invagination and its scission. Scission is the step of endocytosis in which the growing vesicle separates from the donor membrane. The vesicle size typically ranges 60-120 nm in radius in mammals. Yeast vesicles have an oval shape and are typically 30x60 nm in size. The scission step could differ between yeast and mammalian cells probably due to the difference in turgor pressure (and subsequent high and low membrane tension, respectively). In yeast cells, BAR-domain proteins Rvs161 and Rvs167 bind to the curved membrane when the invagination is formed and presumably stabilize the growing neck until the actin cytoskeleton provides sufficient force for vesicle scission. Contrary, mammalian cells can induce vesicle scission without actin polymerization. For this, homologous BAR-domain

proteins such as endophilin and amphiphysin cooperate with the GTPase dynamin to mediate scission.

The last module is the uncoating module. Chaperones, protein kinases and lipid phosphatases are included in this module and they are responsible for disassembling the endocytic proteins from the vesicle and recycle them for another endocytic event. This is also necessary to create a coat-free vesicle surface to allow contact and fusion with endosomes

Initiation of endocytosis

The first step of endocytosis in yeast is its initiation, and it starts with the clustering of the first endocytic proteins at the plasma membrane Ede1, Syp1, AP-2 complex, and Pal1 (Eps15, FCHo1/2, AP-2 complex in human; Stimpson et al., 2009; Carroll et al., 2012). Among all the endocytic modules, which temporal behavior is very regular, the length of the early coat is the most variant, ranging from 30 to 180 seconds, which might reflect a cargo checkpoint prior to the middle coat formation. Besides, deletion of most early coat proteins leads to no apparent phenotype and the mid and late coat are still able to assemble at the endocytic site (Brach et al., 2014). This raised several questions about the early coat proteins including their specific function, what triggers their recruitment to the plasma membrane and what defines their position. However, it is getting widely accepted that they form a seed where the endocytic coat can form in an effective manner, defining the location where the endocytic event will take place and in which frequency. In some cases, endocytosis appears to be initiated in random locations, probably due to stochastic accumulation of endocytic adaptor proteins at the plasma membrane. However, in other cases it is regulated and repeatedly occurs at certain regions of the cell, such as the budding daughter cell in yeast or neuron synapse. The non-random distribution of certain endocytic events suggests certain endocytosis-promoting properties, such as concentration of specific lipids or endocytic cargoes. For instance, many endocytic adaptors, including actin-binding adaptors Sla2 and Ent1, are recruited to the plasma membrane in a phosphatidylinositol 4,5-bisphosphate ($PI(4,5)P_2$)- dependent manner (Sun and Drubin, 2012). In addition, local differences in concentration of endocytic

cargoes also seem to contribute to localization of endocytosis, which could arise e.g. from localized exocytic activity (Kaksonen and Roux, 2018).

Maturation of the endocytic coat

Maturation refers to all events occurring between the end of the early coat formation and the beginning of the invagination phase. This phase typically takes about 30 seconds and its main function is to organize the endocytic coat for the onset of actin polymerization for membrane invagination and subsequent vesicle scission. The maturation process is tightly regulated to ensure the optimal endocytic coat structure (the endocytic coat is densely packed: around 50 different proteins, each one present in tens to hundreds of copies) and to prevent actin polymerization before the coat is formed. The maturation process includes the formation of the middle coat and late coat: the middle coat proteins function is to recruit cargo and clathrin, whereas late coat proteins are regulators of actin polymerization.

The middle coat proteins Yap1801, Yap1802, Sla2, Ent1, and Ent2 (AP180/CALM, Hip1R, epsins 1-3 in human) are thought to be recruited by the interaction with PIP_2 lipid and early coat adaptor proteins. Sla2, equally to its human homologue Hip1R, is a homodimer able to bind membranes with its N-terminal membrane-binding ANTH (AP180 N-terminal homology) domain (Yang et al., 1999). Also, epsins Ent1 and Ent2 are recruited to the endocytic coat through their N-terminal binding domain, ENTH (Epsin N-terminal homology). Sla2 and Ent1 have been implicated in force transmission, connecting the plasma membrane with the actin network at the endocytic site (Skruzny et al., 2012). Finally, two additional mid coat proteins Yap1801 and Yap1802, despite their precise temporal recruitment is still under debate, bind the membrane with their N-terminal ANTH domain. All mid coat proteins contain clathrin-binding motifs and deletion of Sla2 and epsins exhibit temperature-sensitive growth and endocytic defects (Maldonado-Baez et al., 2008).

The transition from mid to late coat is defined by the arrival of Pan1, End3 and Sla1 (supposedly intersectin-s in human), which have the ability to interact with several earlier endocytic adaptors (Sla2, Ent1/2, and Yap1801/2). These proteins form a

complex, which facilitates the arrival of actin nucleation-promoting factors (NPF) Las17 (WASP in human) and myosins Myo3 and Myo5 to the endocytic site. Specifically, Las17, main activator of the actin-nucleator complex Arp2/3, is recruited to the endocytic site by Sla1. Apart from its NPF activity, Las17 recruits Vrp1 (WIP in human), which can recruit the myosins as well and form the Myo5-Vrp1 complex also able to activate actin nucleation (Sun et al., 2006).

The actin cytoskeleton and clathrin-mediated endocytosis

Besides clathrin-mediated endocytosis, the dynamic polymerization of actin filaments plays a central role in other essential membrane-reshaping processes in eukaryotic cells. It is critical for the protrusion of lamellipodia and filopodia during cell migration, for cell division and differentiation, and for different forms of internalization such as other forms of endocytosis, phagocytosis, and macropinocytosis (Kaksonen et al., 2006).

The importance of actin polymerization in clathrin-mediated endocytosis was first observed using pharmacological agents perturbing the actin cytoskeleton. Studies performed in yeast *S. cerevisiae* showed that actin is required for successful progression of CME: both actin toxins latrunculin A, which binds to actin monomers and prevents polymerization, and jasplakinolide, which stabilizes actin filaments and prevents depolymerization, blocked endocytosis completely (Ayscough et al., 1997; Ayscough, 2000). Contrary, actin polymerization appeared to be less critical in mammalian cells. Cells treated with actin toxins showed inhibited endocytic uptake and formation of coated vesicles, but this effect seemed to be partial or cell-type specific (Gottlieb et al., 1993; Lamaze et al., 1997). Further experiments proved that actin is essential for endocytosis in mammals in cases when additional force is required e.g. to ingest larger cargoes or in cells with higher plasma membrane tension (Boulant et al., 2011). The different requirement for actin assembly at the endocytic sites between yeast and mammalian cells may be a consequence of the difference in turgor pressure. Yeast cells have significantly higher turgor pressure to that in animal cells, and therefore actin polymerization is essential to provide the extra force necessary for endocytic vesicle formation in yeast. In agreement, actin mutants in yeast proved that normal actin function is required for the internalization

step of endocytosis. The later trafficking steps of the endocytic pathway were not affected (Kübler and Riezman, 1993). The location of actin also indicates its major role in endocytosis. Actin-rich foci on the plasma membrane, called actin patches, are locations of clathrin-mediated endocytosis events in yeast. These structures are very easily observed in yeast cells because they lack cortical actin cytoskeleton. Similarly, live-cell imaging and electron microscopy studies showed that actin filaments are often associated with coated pits in mammalian cells (Merrifield et al., 2002; Shupliakov et al., 2002; Collins et al., 2011; Akamatsu et al., 2019). Moreover, many studies have shown a number of protein-protein interactions between the endocytic machinery and the actin cytoskeleton. These biochemical analyses indicate that multiple endocytic proteins can be linked to actin, either directly or indirectly (Qualmann et al., 2000). Taken together, actin polymerization has been recognized as a critical source of mechanical force required for the deformation and movement of the membrane during endocytosis.

Actin is a 42 KDa globular protein (G-actin), but its active form able to produce force and reshape membranes is in a polarized polymer that forms filaments (F-actin). Actin monomers contain an ATP molecule, which allows them to assemble to an existing filament. This assembly triggers the hydrolysis to ADP and release of a phosphate group. In order to produce force to reshape the membrane during endocytosis, actin polymerization is initiated at the plasma membrane and filaments seem to grow mainly perpendicular to the membrane towards the cytoplasm (Picco et al., 2015). Growing filaments connected to the plasma membrane transmit the force required to reshape the membrane and create the endocytic invagination. For this reason, actin polymerization regulators are essentially found at the base of the invagination (Kaksonen et al., 2003, 2005). This includes the actin nucleator complex Arp2/3, so far the only known actin nucleator able to create new actin filaments from the sides of existing "mother" filaments at a 70° angle (Mullins et al., 1998). Nucleation-promoting factors (NPFs) are also found at the base of the invagination, where they increase the ability of Arp2/3 to nucleate new branched actin filaments (Mooren, 2012). In yeast, Arp2/3 is able to nucleate actin in absence of NPFs, however with very low efficiency. Thus, the role of NPFs in yeast may be to localize, enhance or adjust the activity of Arp2/3 (Wen and Rubenstein, 2005). Four NPF proteins have been found to increase yeast Arp2/3 activity *in vitro*: Las17 (WASP in human), type IE myosins Myo3/5 in complex with Vrp1, Pan1, and Abp1. Las17 and Myo5

are categorized class I NPFs due to their ability to bind actin monomers (G-actin) and have strong NPF activity. Pan1 and Abp1, in contrast, can only bind filamentous actin (F-actin) and have weaker NPF activity (Sun et al., 2006). Las17 is the most important activator of the Arp2/3 complex, and therefore it is tightly regulated. Initially, Sla1 inhibits its activity to prevent actin polymerization before the endocytic coat is correctly formed. And later, when the membrane is already being invaginated, Bbc1 inhibits Las17 and myosins Myo3/5 to prevent further unnecessary Arp2/3-mediated actin nucleation (Rodal et al., 2003; Mochida et al., 2002).

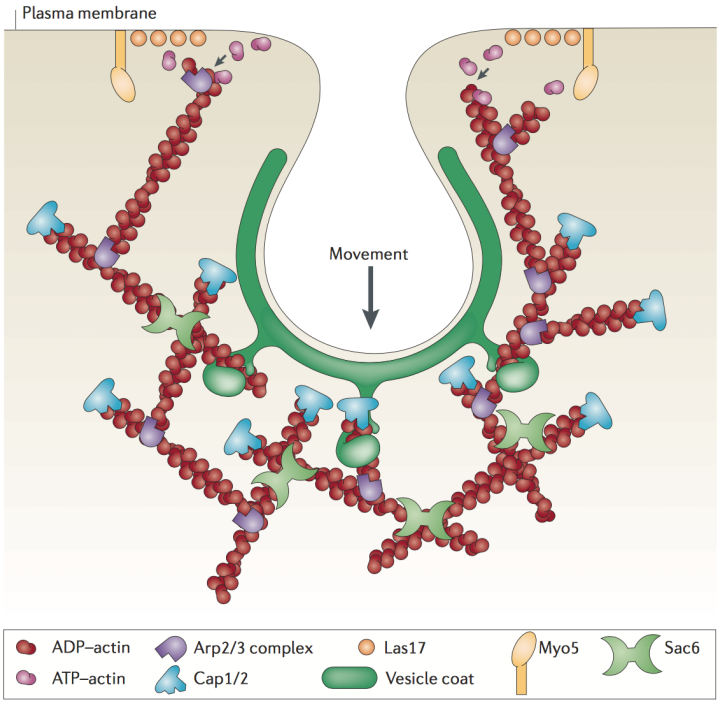

Figure 2 Current model for actin-driven membrane reshaping during endocytosis. Las17 and Myo5 localize at the base of the invagination to activate the Arp2/3 complex. Arp2/3 actin-nucleation complex creates new actin filaments forming 70°-degree angles. Cap1/2 proteins prevent lengthening of new filaments. Sac6, together with other proteins (see text), create a dense crosslinked actin network able to invaginate the membrane during endocytosis. The vesicle coat is responsible for transmitting actin-driven force to the plasma membrane (image from Kaksonen et al., 2006).

Once nucleated, new growing filaments are rapidly capped at their barbed ends by Cap1/2 proteins to restrict their length. These short actin filaments are crosslinked in a parallel, antiparallel and orthogonal manner to create a dense filaments network with distinct geometries and properties. Five crosslinking proteins are found in yeast, probably working at different stages to provide different properties to the actin cytoskeleton: Sac6 (fimbrin in human), Scp1 (calponin), Abp140, Crn1, and Tef1/2 (Goode et al, 2015).

Mechanisms of membrane bending and vesicle scission during endocytosis

Clathrin-mediated endocytosis involves a series of morphological changes in the membrane that are opposed to the membrane homeostatic state: cellular lipid bilayers composed of phospholipids are usually flat and therefore require energy to be reshaped. Membrane-bending stiffness and membrane tension, as well as cell turgor pressure, oppose endocytosis, making it an energetically high demanding process. The energy required to invaginate the membrane and create a vesicle depends therefore on the magnitude of these parameters.

Since turgor pressure is low in mammalian cells, the largest energetic barrier to overcome during endocytosis is cell membrane tension. Considering high membrane tension, around 0.5 pN/nm, computer simulations suggest around 100–200 pN force to pull the membrane into an elongated tube (Walani et al., 2015). This can be even reduced to tens of piconewtons by the action of membrane-remodeling endocytic factors. In case of low membrane tension, around 0.002 pN/nm, simulations suggest that endocytosis could be possible without applying any external force and that endocytic proteins could be sufficient to create a vesicle (Hassinger et al., 2017). In yeast, cell turgor pressure is high, around 0.4-0.8 MPa (Schaber et al., 2010), approximately 200-1000 times higher than for mammalian cells. Cell turgor therefore represents the major energetic barrier, which cannot be overcome without the pulling force of the actin cytoskeleton.

Several theoretical and computational studies have aimed to calculate the force required to invaginate the membrane during endocytosis (summarized in Table 1). They are often focused on endocytosis in yeast, where actin is essential for vesicle budding and where key protein players and membrane-shape profiles have been already established. Despite the efforts, there is still a significant variability between the results obtained, probably due to the different parameters considered for each of the simulations. However, simulations support the empirical observation that force required to invaginate the membrane in high turgor cells like yeast is significantly higher than in low turgor cells whose membrane invagination is predominantly hindered by membrane tension.

Table 1 Recent studies aimed to calculate the force required to invaginate the membrane during endocytosis in budding yeast.

Reference	Calculated force required for endocytosis
Zhang et al., 2015	Actin-driven force of 200 pN
Carlsson et al., 2014	Force of 400 pN required to counter turgor pressure
Wang and Carlsson, 2017	Actin-driven force of approx. 725 pN
Scher-Zagier and Carlsson, 2016	Polymerizing actin force of 1300 pN
Nickaeen et al., 2019	Actin-driven force of 2200-3000 pN
Dmitrieff and Nédélec, 2015	Force required for endocytosis of 1000-5000 pN

This difference in the energy required to invaginate the membrane might be an explanation to the main differences between endocytosis in yeast and mammalian cells. Yeast cells always require actin polymerization for successful endocytosis, whereas in mammalian cells it is only required in conditions of increased membrane tension (Boulant et al., 2011). Related to this, the mechanism of vesicle scission is also affected. While yeast cells use actin-driven mechanical force, mammalian cells require the action of the GTPase dynamin for vesicle scission. Despite the exact molecular mechanism of its action is not fully understood, dynamin assembles around the neck of the endocytic invagination forming a spiral oligomeric scaffold. Upon GTP binding, the oligomer changes conformation, reducing its radius of curvature to 10 nm, therefore compressing the invagination neck (Antonny et al., 2016). Contrary to that, the role of dynamin in yeast cells remains unclear. Whereas some studies suggest a role of dynamin yeast homologue Vps1 in clathrin-mediated endocytosis, some others conclude that Vps1 does not contribute nor localizes to the endocytic site. While more research is required, it might have a regulatory, yet not essential, role in scission (Kaksonen and Roux, 2018).

Other membrane-remodeling factors

Apart from the actin cytoskeleton polymerizing at the endocytic site, several other endocytic factors are directly involved in force production by actively deforming the membrane or indirectly by reducing the energy barrier for membrane remodeling or vesicle scission.

In yeast cells, some endocytic proteins have the ability to induce membrane curvature *in vitro*, such as BAR-domain proteins Rvs161/167, or the endocytic adaptors Sla2 and Ent1 (Youn et al., 2010; Skruzny et al., 2015). However, the cell turgor pressure is high, so their membrane-remodeling ability is most probably not sufficient to overcome the high energy demand, thus the membrane remains flat until actin polymerization starts *in vivo* (Kukulski et al., 2012). Contrary, endocytosis in mammalian cells depends on membrane curvature induced by endocytic adaptors to invaginate the membrane, especially in actin-independent endocytic events.

Clathrin triskelions, each composed of three heavy chains and three light chains, polymerize forming a cage that surrounds the endocytic vesicle. Despite not being completely required, clathrin has the ability to induce membrane curvature and probably it contributes to it. Besides, several endocytic proteins contain membrane-binding BAR domains, which can both sense and induce membrane curvature. At low protein concentrations, most BAR domains only bind to bent membranes of their preferred curvature. This changes when they are present at high concentration, then they are also able to generate membrane curvature. During clathrin-mediated endocytosis several early coat proteins contain F-BAR domains, which have preference for moderate curvature. Proteins involved in the membrane scission module contain highly curved N-BAR domains, such as Rvs161/167 in yeast or endophilin and amphiphysin in mammals (Fricke et al., 2010). Other domains present in endocytic factors are also able to induce membrane curvature, including the membrane-binding domains ENTH present in epsins Ent1/2 (epsin 1/2/3 in human), or ANTH domain present in Sla2 (Hip1R in human) and Yap1801/2.

Apart from specific membrane-remodeling activity present in some endocytic proteins, membrane reshaping can also occur due to steric clashes of bulky membrane-associated

proteins. This effect, known as molecular crowding, can induce tabulation and scission of membranes *in vitro* (Mim et al., 2012).

Altogether, the total force required for endocytosis is provided by several mechanisms: (1) by the action of membrane-remodeling endocytic factors (ANTH-, ENTH-, and BAR-domain proteins, etc.); (2) by the formation of the clathrin coat; (3) by the oriented polymerization of the actin cytoskeleton; (4) by the crowding effect of bulky endocytic adaptors; and (5) by the mechanoenzyme dynamin (Kaksonen et al., 2006; Dannhauser and Ungewickell, 2012; Daumke et al., 2014). These mechanisms work at different stages of endocytosis and their functional role vary depending on the force required to invaginate the membrane, especially when comparing endocytosis in yeast and mammalian cells.

FORCE TRANSMISSION DURING ENDOCYTOSIS

Molecular basis for force transmission during endocytosis

During endocytosis, the force of polymerizing actin has to be transmitted via the endocytic coat to the plasma membrane. For this purpose, actin filaments are nucleated and polymerized at the base of the invagination towards the cytoplasm and physically coupled to endocytic adaptors (Fig. 2).

Physical coupling of the actin cytoskeleton to the membrane is required to transmit the force necessary to reshape the membrane. Sla2 and Ent1, yeast homologues of human Hip1R and epsin, were identified as the molecular linker between the plasma membrane and the actin cytoskeleton of the endocytic site (Skruzny et al., 2012). First, the N-terminal membrane-binding domain of Sla2 and Ent1, ANTH and ENTH, respectively, seem to form a highly organized coat on the membrane essential for endocytosis. Disruption of the ANTH-ENTH coat by point mutations in either of these domains induces a strong growth defect and endocytosis arrest (Skruzny et al., 2015). Second, their C-terminal actin-binding domains, THATCH and ACB, respectively, redundantly bind actin to allow the

transmission of mechanical force for membrane invagination (Fig. 3). Deletion of both THATCH and ACB domains induces strong endocytic arrest accompanied by actin polymerization occurring at the endocytic site, indicating that actin polymerization can be activated but its polymerizing force cannot be properly transmitted to the plasma membrane for membrane invagination (Skruzny et al., 2012). Importantly, other studies suggest that the homologous proteins operate identically in mammalian cells (Messa et al., 2014).

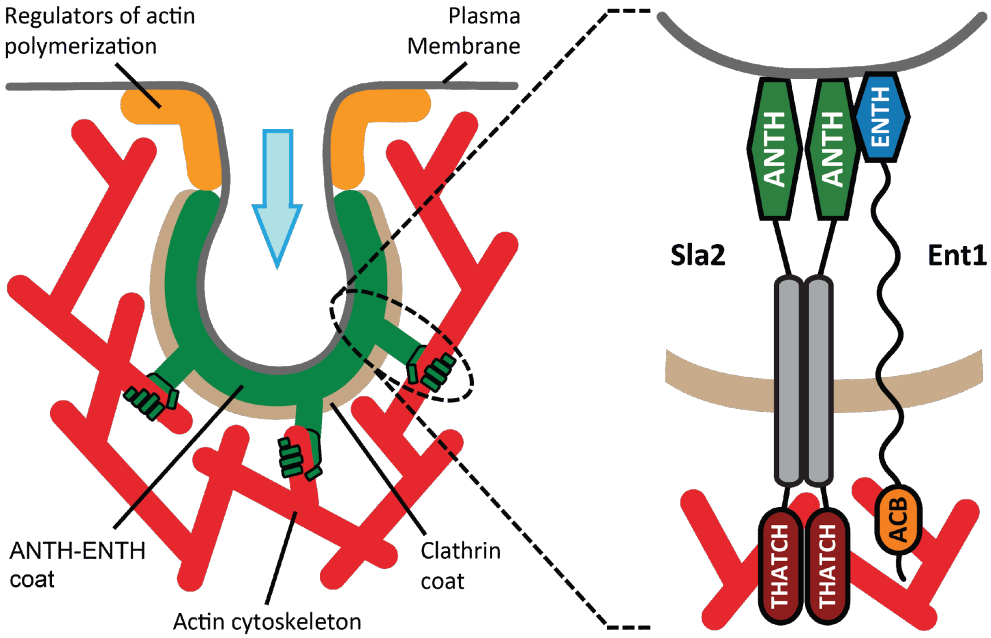

Figure 3 Scheme of actin-driven endocytic internalization in yeast. (Left) Sla2-Ent1 coat (in green) couples actin filaments to the membrane and transmits the force of actin polymerization for membrane invagination. (Right) ANTH and ENTH domains of Sla2 and Ent1, respectively, form a regular coat to distribute and withstand pulling forces provided by the actin cytoskeleton. THATCH and ACB domains interact with the actin filaments and link thus physically the actin cytoskeleton to the plasma membrane (adapted from Skruzny et al., 2012).

Measuring force transmission during endocytosis by FRET-tension sensors

To mechanistically understand force-dependent endocytic vesicle formation, applied forces need to be analyzed in the cellular context to report real force values and to assess the contribution of other endocytic factors to force transmission. To achieve this, we here aim to measure the force required for endocytic vesicle formation in live cells of yeast *Saccharomyces cerevisiae*. For this purpose, we will use Förster resonance energy transfer (FRET) biosensors that allow the measurement of forces *in vivo*.

FRET microscopy is a powerful fluorescence method that allows the study of nanoscale organization of multiprotein complexes, as well as the monitoring of biophysical and biochemical processes at the molecular level. FRET is an electromagnetic phenomenon by which the energy of a light-excited fluorophore molecule (donor) is transferred to another molecule (acceptor) by dipole-dipole coupling. When the acceptor is also a fluorophore, FRET leads to its excitation and subsequent acceptor fluorescence emission.

FRET efficiency depends on the orientation of donor and acceptor dipole moments, the quantum yield of the donor, the extinction coefficient of the acceptor, integral overlap between the normalized donor emission and acceptor excitation spectra, and, most importantly, the sixth root of the distance between donor and acceptor molecule (Fig. 4). Because of this distance dependency, FRET usually occurs only between molecules separated by less than 10 nm. This makes FRET a unique nanometer-sensitive method suitable to study distances, proximities and interactions of molecules, both *in vivo* and *in vitro* (Ishikawa-Ankerhold et al., 2012; Stryer, 2003; Teunissen et al., 2018).

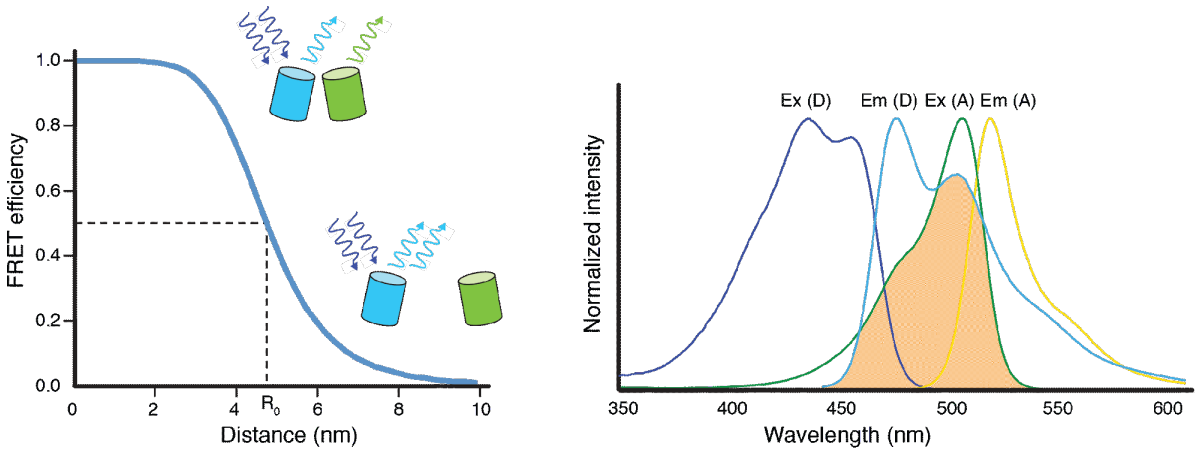

Figure 4 Basics of FRET. (Left) Dependence of FRET efficiency on the distance R between donor and acceptor molecules. Förster radius R_0 is the distance at which half of the energy of the excited donor is transferred by FRET. (Right) Excitation/absorption (Ex) and emission (Em) spectra of mTurquoise2 donor (D) and mNeonGreen acceptor FRET pair. Spectral overlap between mTurquoise2 emission and mNeonGreen excitation spectra is highlighted in orange (adapted from Skruzny et al., 2019).

In order to measure the force transmitted during endocytosis, we will use FRET-based tension sensor modules (TSMs) that allow the measurement of mechanical forces *in vivo* (Freikamp et al., 2016). TSMs consist of two fluorophores undergoing efficient FRET connected by a mechanosensitive peptide, which reversibly extends at low piconewton

(pN) forces. Under no tension, the two fluorophores are close in space allowing high FRET transmission from donor to acceptor. When force is applied, the sensor peptide stretches and separates the fluorophores, therefore inducing a decrease in FRET. Similarly, when force is released, the linker returns to its initial folded conformation (Fig. 5). Therefore, TSMs report about applied forces by changes in FRET.

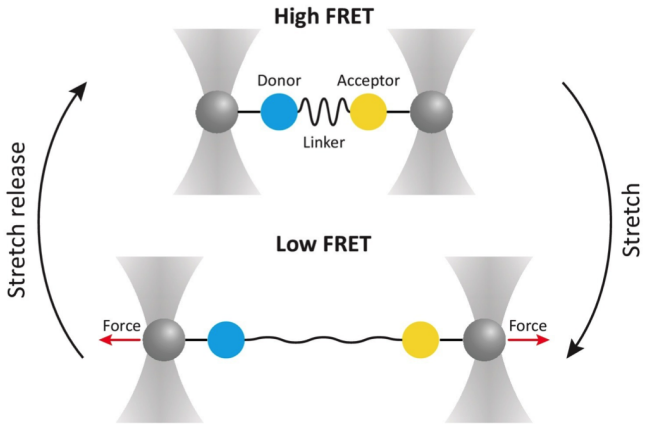

Figure 5 Functioning of FRET-based tension sensor modules *in vitro*. Under no tension, donor and acceptor fluorophores are close in proximity and FRET efficiency is high. When force is applied, the peptide linker stretches, inducing a decrease in FRET. Upon relaxation, the linker recovers its initial conformation and FRET increases again (adapted from Freikamp et al., 2016).

To determine the force produced during endocytosis, we plan to use several peptide linkers sensitive to different force ranges. Among the available calibrated sensor peptides, we will use F40, HP35, and HP35st peptides for covering a wider spectrum of forces and therefore potentially provide better force resolution (Table 2; Fig. 6).

Table 2 FRET-based TSM peptide linkers used in this study.

Name	Peptide linkers	Force Sensitivity	Reference
F40	Flagelliform peptide $(GPGGA)_8$	1-6 pN	Grashoff et al., 2010
HP35	WT villin headpiece peptide	6-8 pN	Austen et al., 2015
HP35st	Stabilized villin headpiece peptide	9-11 pN	Austen et al., 2015

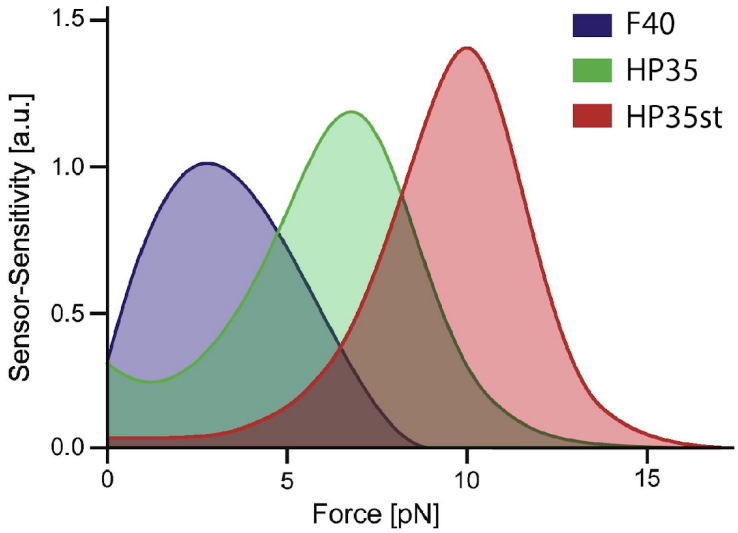

Figure 6 Sensor sensitivities reflecting FRET-force relationship for the three force-spectroscopy calibrated TSM linkers used in this study (adapted from Freikamp et al., 2017).

Altogether, we aim to construct TSMs and insert them into the essential force-transmitting endocytic protein Sla2. In order to measure all actin-dependent force transmitted during endocytosis, we will channel all force through the Sla2 force sensor (Sla2 FS) by deleting the functionally redundant actin-binding domain of Ent1 in all strains (*ent1ΔACB* background). We will follow force transmitted in real time by measuring FRET changes of Sla2 force sensors during the progression of endocytosis. We will analyze FRET changes by recording of donor and acceptor fluorescence during individual endocytic events, by technique called ratiometric FRET. Here, ratio of acceptor and donor emissions is followed simultaneously using an image splitter during a biological process. Changes in FRET ratio during the experiment will indicate, in our system, force applied over Sla2 FS (Fig. 7).

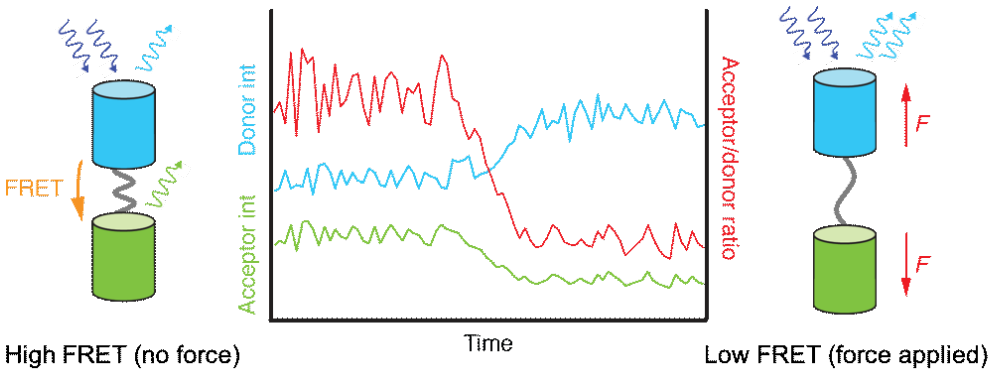

Figure 7 Ratiometric FRET method applied to measure force transmitted over TSM sensor. Initially, donor (blue) and acceptor (green) fluorophores are close in proximity due to folding of the peptide linker, resulting in high FRET accompanied by lower donor fluorescence intensity and higher acceptor fluorescence intensity (left). The application of force separates the fluorophores, yielding a decrease in FRET and in acceptor/donor intensities ratio (red, right) (adapted from Skruzny et al., 2019).

Besides measuring total force applied during endocytosis, we will assess the contribution of individual membrane-reshaping proteins to force-dependent steps of endocytosis. For that, we will follow FRET changes over our Sla2 FS in deletion strains of selected endocytic factors. We aim to delete specific i) components of the force generation machinery (myosin Myo5), ii) membrane-remodeling proteins of the BAR-domain family (Rvs167), and iii) regulators of actin polymerization at the endocytic site (Bbc1). Finally, we will investigate the relevance of several external physical cues in endocytic force requirements by following force transmission under modified environmental conditions. We will focus on changes in osmolarity, which will affect turgor pressure of yeast.

Altogether, the implementation of molecular biosensors reporting the forces required for endocytic vesicle formation will represent a substantial methodological advance towards our mechanistic understanding of the endocytic process. Quantifying the force required to invaginate the membrane during endocytosis is crucial to understand the mechanobiology of the endocytic pathway and will certainly help to better comprehend other essential membrane reshaping processes in the cell. Moreover, the knowledge of force contributions of individual endocytic factors and the effect of the environmental cues will provide insights in force generation and transmission during endocytosis and how yeast cells regulate these processes in various external conditions.

RESULTS

Construction and verification of Sla2 force sensor strains

In order to measure the force required to invaginate the membrane during endocytosis in yeast, we decided to use tension sensor modules (TSMs) that allow the measurement of mechanical forces *in vivo* (Freikamp et al., 2016). For this purpose, we employed several TSMs containing a specific tension-sensitive peptide separated by two fluorophores that undergo efficient FRET. Under no tension, the two fluorophores are close in proximity allowing high FRET from donor to acceptor fluorophore. When force is applied, the sensor peptide stretches and separates the fluorophores, therefore inducing a decrease in FRET (Fig. 5 of Introduction).

We prepared TSMs containing the two fluorophores mTurquoise2 and mNeonGreen, which have been proved to constitute a very efficient FRET donor-acceptor pair (Mastop et al., 2017). In order to quantify the force required for endocytosis, we covered a wide spectrum of forces and used three peptide linkers sensitive to different force ranges: F40 (1-6 pN), HP35 (6-8 pN), and HP35st (9-11 pN) (Freikamp et al., 2016).

We then created plasmids coding for the Sla2 force sensor (Sla2 FS) constructs with the force sensor modules inserted in Sla2 protein between the central dimerization coiled-coil domain and the C-terminal actin-binding domain (THATCH). We also generated Sla2 no force control constructs (Sla2 no force control, Sla2 NF), where force cannot be transmitted over the force sensor because it is located in Sla2 after the actin-binding domain. In addition, in our strains we deleted the actin-binding domain of Ent1, ACB, in order to channel all actin-dependent force through our tension sensor and therefore measure all force transmitted from the actin cytoskeleton to the membrane during endocytosis (Fig. 8).

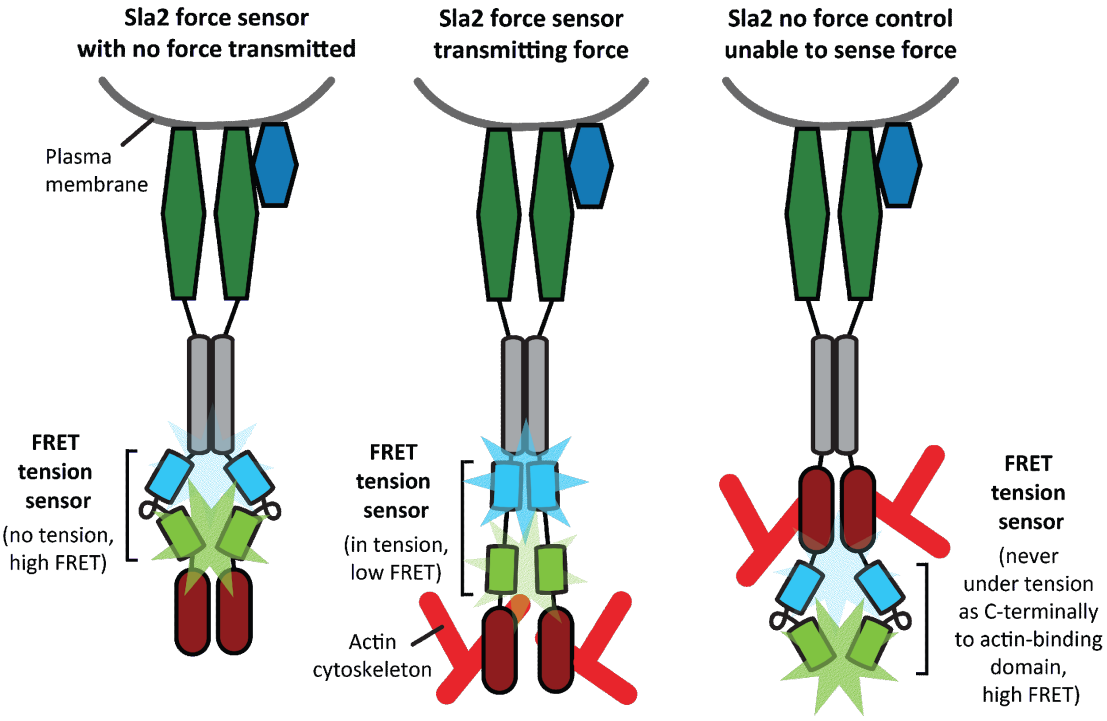

Figure 8 Principles of FRET-based Sla2 force sensors used in this study. (Left) When force is not transmitted, FRET between mTurquoise2 and mNeonGreen fluorophores inserted into Sla2 protein is high. (Middle) Upon force applied by the actin cytoskeleton, the tension sensor stretches and therefore FRET decreases. (Right) No force is transmitted over the FRET sensor when its fluorophores are located after the actin-binding THATCH domain of Sla2 constituting thus a no force control to discern force-dependent and force-independent FRET signal variations.

First, Sla2 force sensor constructs were tested for their functionality by growth assays in Sla2-deleted cells, where they showed full functional complementation of growth defect of Sla2 deletion (Fig. 9A).

Next, we integrated Sla2 FS and Sla2 NF constructs into *SLA2* locus in *ent1ΔACB* background and tested whether the dynamics of the endocytic process and modified Sla2 protein were altered. For this, we monitored endocytosis by live-cell imaging following Sla2 dynamics. No significant difference was observed in lifetime at the endocytic site between C-terminally-tagged Sla2 (Sla2-mNG) and Sla2 FS (Sla2 lifetime 46.6 ± 4.2 s and 51.5 ± 3.7 s, respectively; 91.2% and 84.0% of endocytic events completed during 4 min, respectively; Fig. 9B).

In addition, we evaluated the maximum FRET that mTurquoise2 and mNeonGreen pair could undergo in our *in vivo* system. For this purpose, we measured FRET efficiency in cells treated with Latrunculin A (LatA), drug that inhibits actin polymerization and arrests endocytic events in the flat membrane stage, where the endocytic coat is formed. With no

actin present, the FRET in the force sensor should be therefore maximum. To measure the FRET efficiency between mTurquoise2 and mNeonGreen fluorophores, we used acceptor photobleaching FRET, a simple and reliable technique based on the inactivation of the acceptor fluorophore. The inactivation of the FRET acceptor performed by photobleaching with a suitable laser induces an increase in the donor fluorescence emission, which can be easily recorded, and FRET efficiency can be therefore calculated as the percentage increase of donor fluorescence after acceptor photobleaching. We observed very high FRET values, above 50%, for all three constructs, indicating the suitability of this FRET pair to be used *in vivo* in yeast cells (Fig. 9C).

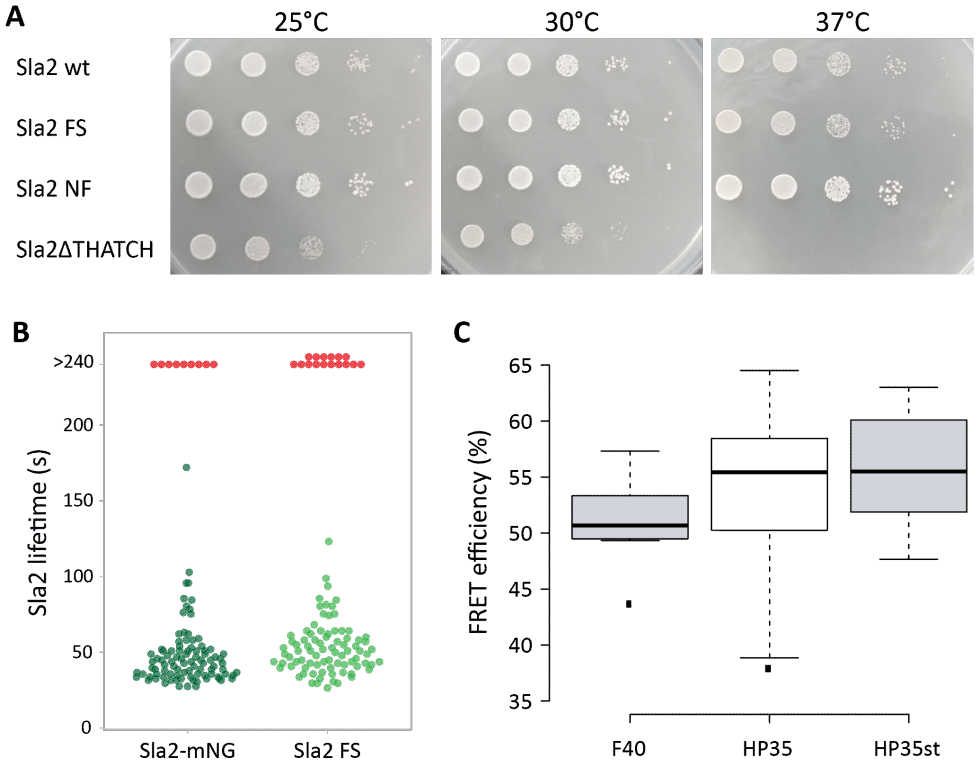

Figure 9 Sla2 force sensors complement Sla2 function. (A) Ten-fold serial dilutions of *sla2Δ, ent1ΔACB* strain expressing indicated proteins from *URA3 CEN* plasmid were incubated on SD-Ura plates for 1.5-2 days at indicated temperatures. Sla2ΔTHATCH construct unable to bind actin was used as negative control. (B) Lifetimes of Sla2-mNG and Sla2 FS at the endocytic sites prior to vesicle scission (Sla2-mNG n=102, Sla2 FS n=100). Red-colored dots indicate endocytic patches with lifetime longer than 4 min. Imaging settings to acquire mNeonGreen emission were identical for both constructs. (C) FRET efficiency of mTurquoise2-mNeonGreen pair in Sla2 FS constructs separated by indicated peptide linkers measured in yeast cells after LatA treatment. FRET values of multiple endocytic patches of several cells (n=10, 18, and 25). Centre, top, and bottom lines of the box plots show the median, 25th, and 75th percentiles of individual datasets, respectively. Whiskers extend to data points 1.5 times the interquartile range from the 25th and 75th percentiles.

Force of approx. 10 pN is transmitted over Sla2 protein during actin-driven endocytic vesicle formation

To follow forces applied over Sla2 force sensors (manifested by changes of their FRET signal, see Fig. 8), we monitored mTurquoise2 and mNeonGreen fluorescence signals during individual endocytic events. Endocytic events were imaged and manually tracked (with 1 second time resolution) and their mNeonGreen/mTurquoise2 fluorescence ratios were calculated to obtain the FRET ratio profile. Decrease of the FRET ratio mNeonGreen/mTurquoise2 indicated force applied on the force sensors (see Fig. 7 for details). For the alignment of endocytic events, the time of vesicle scission, characterized by rapid cytoplasmic movement of the fluorescence signal, was used and considered as time 0 seconds.

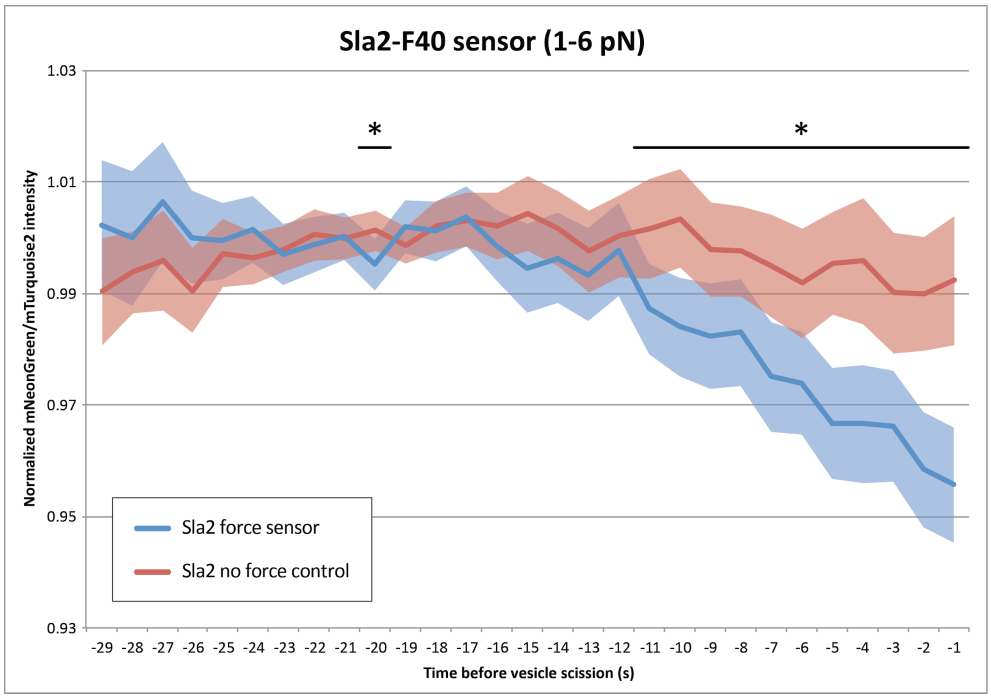

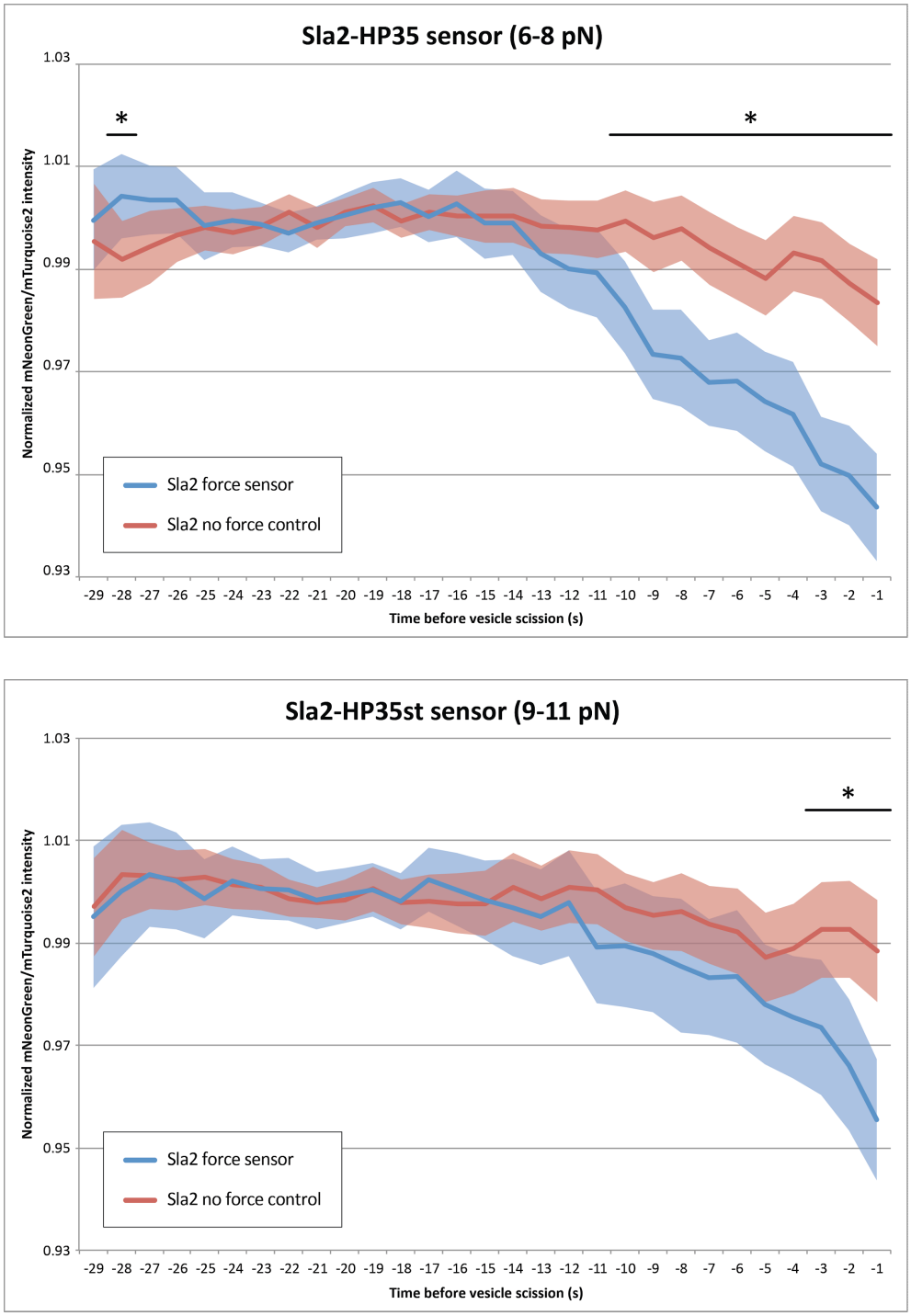

Figure 10 FRET ratio signal of indicated Sla2 force sensors (blue) and respective Sla2 no force controls (red) before vesicle scission (time 0 s). Average ± 95% confidence intervals of Sla2-F40 force sensor (n=92), Sla2 no force control F40 (n=58), Sla2-HP35 force sensor (n=108), Sla2 no force control HP35 (n=82), Sla2-HP35st force sensor (n=93), Sla2 no force control HP35st (n=61) are shown. * Indicates statistically significant difference between indicated datasets ($p<0.05$) evaluated using two-tailed Welch's t-test. Complete data provided in Supplementary Tables S1, S2, and S3, respectively.

A sequential decrease of FRET ratio of all three Sla2 FS suggested force exertion over Sla2 molecules starting approximately 13 seconds before vesicle scission (Fig. 10). This timing coincided very well with the appearance of Abp1-mScarlet-I actin marker at the endocytic site (average appearance ± SD: 12.7 ± 2.6 s before vesicle scission; Fig. 11), suggesting a strong correlation between force applied over the Sla2 force sensors and initiation of actin polymerization at the endocytic site.

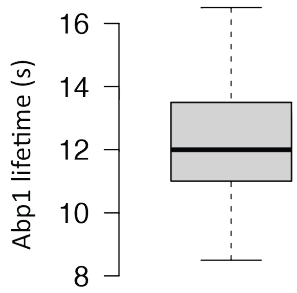

Figure 11 Abp1-mScarlet-I lifetime at the endocytic sites prior to vesicle scission measured in Sla2-HP35 strain (n=45). Centre, top, and bottom lines of the box plots show the median, 25th, and 75th percentiles of individual datasets, respectively. Whiskers extend to data points 1.5 times the interquartile range from the 25th and 75th percentiles.

Interestingly, we observed similar FRET profiles of Sla2-F40 and Sla2-HP35 force sensors despite the different force required for their extension: this indicates that actin-dependent force during endocytosis might be sufficiently high to extend both sensors similarly. Contrary, Sla2-HP35st force sensor, which requires the highest force to be extended, 9-11 pN, showed a reduced decrease in FRET (Fig. 10). HP35 and HP35st are both 35-amino acids long peptide linkers that only differ in two residues and therefore can extend to similar maximal length (Ringer et al., 2017). Direct comparison between Sla2-HP35 and Sla2-HP35st showed a significant difference in their FRET profiles prior to vesicle scission (Fig. 12). This strongly suggests that actin-driven force during endocytosis is not sufficient to extend HP35st tension sensor completely, and that force applied over Sla2 therefore lies inside HP35st force range, being roughly 10 pN.

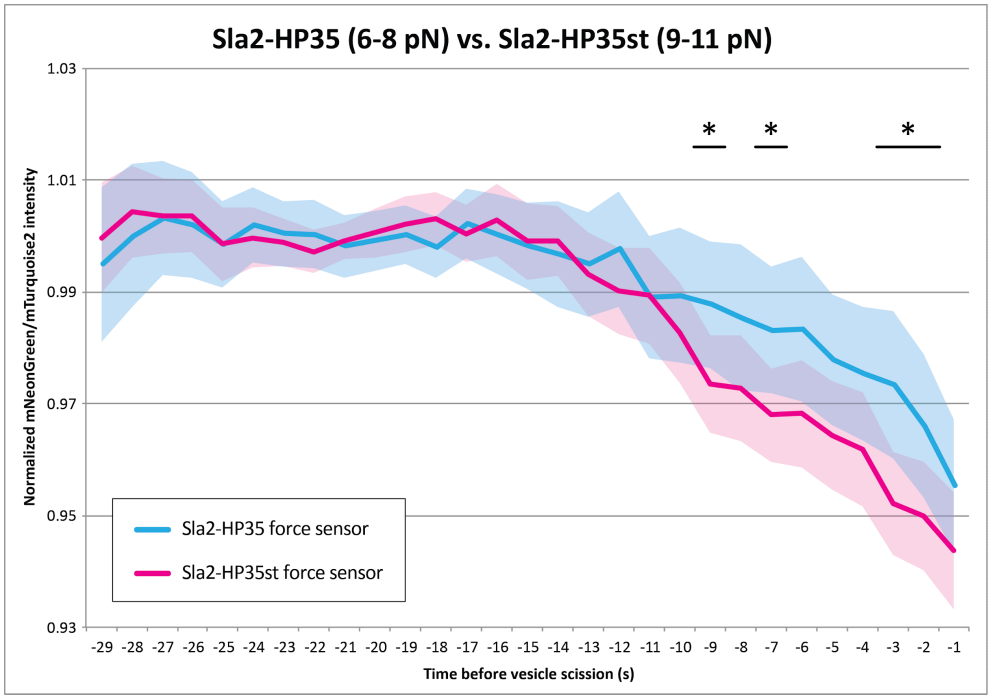

Figure 12 Comparison of FRET ratio signal between Sla2-HP35 and Sla2-HP35st force sensors before vesicle scission (time 0 s). Average ± 95% confidence intervals of Sla2-HP35 force sensor (n=108) and Sla-HP35st force sensor (n=93) are shown. * Indicates statistically significant difference between indicated datasets ($p<0.05$) evaluated using two-tailed Welch's t-test. Complete data provided in Supplementary Table S4.

Taken altogether, the use of various tension sensors sensitive to different force ranges suggests an approximate force of 10 pN transmitted per Sla2 molecule. Considering the recently calculated number of Sla2 molecules at the endocytic site, roughly between 45-133 molecules (Picco et al., 2015; Sun et al., 2019), a force of ~ 450-1330 pN is therefore transmitted over Sla2 during endocytic vesicle formation.

Besides, the decrease of FRET ratio observed for all three Sla2 force sensors occurred similarly in a stepwise manner starting from the onset of actin polymerization to vesicle scission. This suggests sequential harnessing of individual Sla2 molecules to the growing actin cytoskeleton at the endocytic site (see Discussion for details).

Additionally, we decided to implement another FRET control to discard the possibility that observed FRET ratio change is caused by the different position of the TSM in Sla2 FS and Sla2 NF constructs. For this purpose, we created a Sla2 no force control sensor with the TSM placed after the central dimerization coiled-coil domain but deleted from the subsequent THATCH domain (Sla2 NF ΔTHATCH). To restore endocytic vesicle formation

in this strain, Ent1 protein was left intact to channel actin-dependent force over its actin-binding ACB domain.

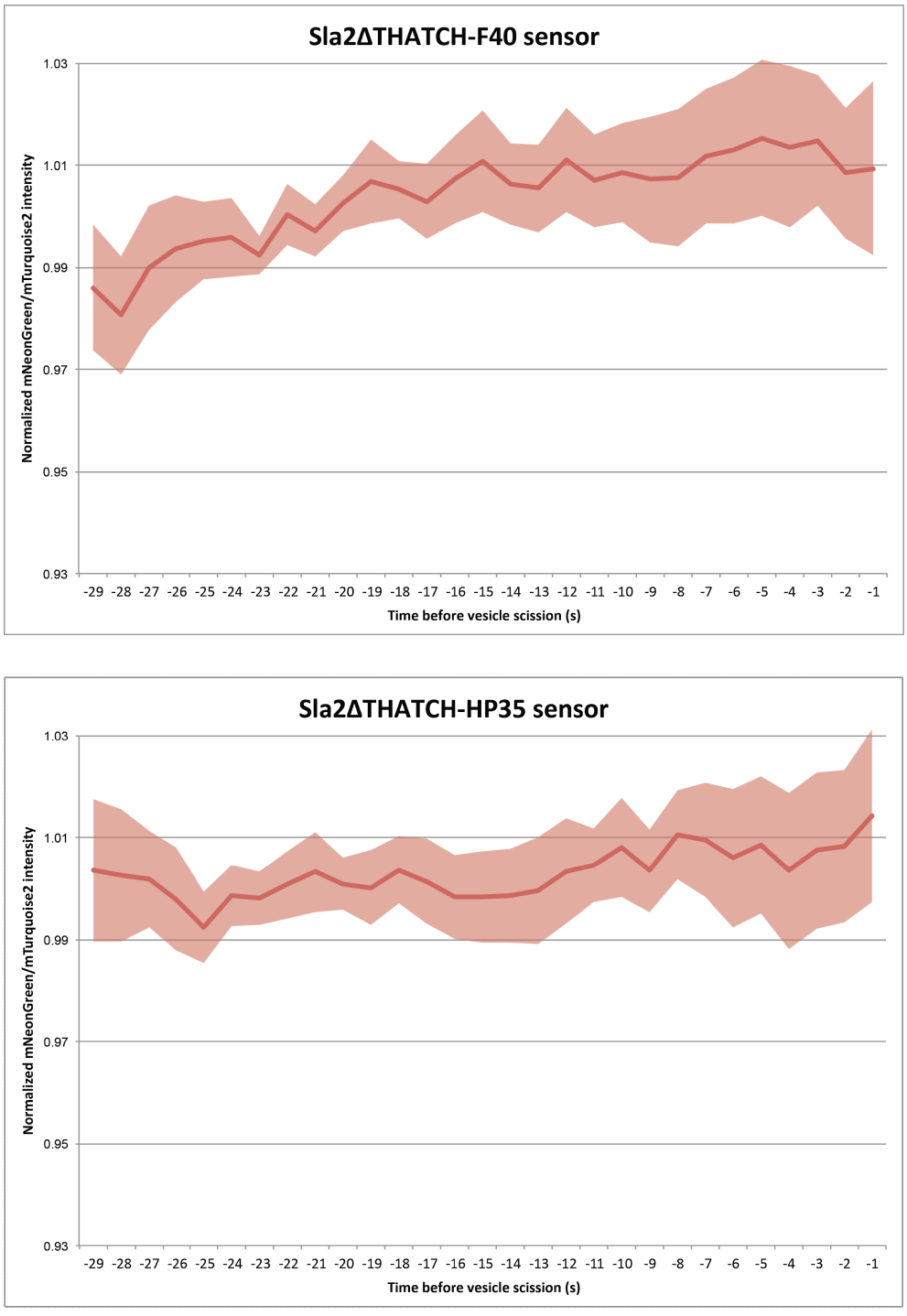

Figure 13 FRET ratio signal of indicated Sla2ΔTHATCH no force controls before vesicle scission (time 0 s). Average ± 95% confidence intervals of Sla2ΔTHATCH-F40 no force control (n=26), Sla2ΔTHATCH-HP35 no force control (n=31) are shown. Complete data provided in Supplementary Table S5.

FRET imaging showed no decrease in the FRET ratio during membrane invagination for Sla2ΔTHATCH-F40 and Sla2ΔTHATCH-HP35 controls (Fig. 13). The absence of FRET ratio

drop strongly supports that FRET changes specifically observed in Sla2 FS strains can be assigned to force-dependent processes applied on Sla2 FS molecules, and not to their conformational or intermolecular FRET changes eventually occurring during endocytic membrane invagination.

Contribution of individual endocytic proteins to endocytic force transmission

Having FRET-based endocytic force measurements established, we next decided to determine the contribution of several endocytic proteins to force-dependent steps of endocytosis. For this purpose, we followed FRET changes of Sla2-F40 or Sla2-HP35 force sensors in strains deleted of selected endocytic proteins proposed to be involved in endocytic force transmission: i) force generator and actin polymerization activator type IE myosin Myo5, ii) membrane-sculpting BAR-domain protein Rvs167, and iii) actin polymerization inhibitor Bbc1.

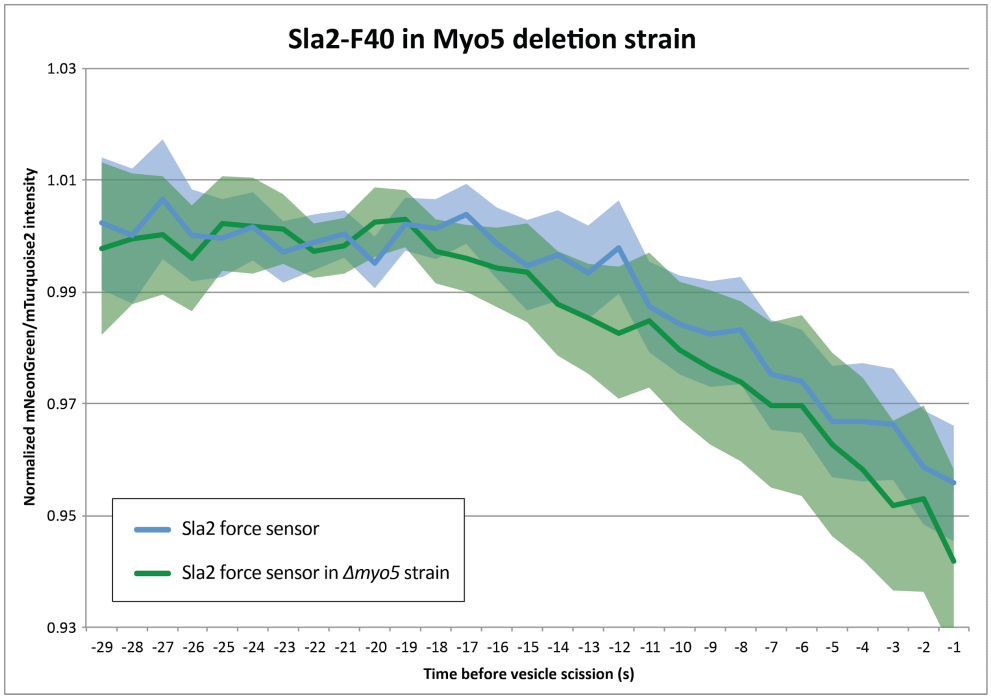

Figure 14 FRET ratio signal of Sla2-F40 force sensor in strain deleted of Myo5 protein (green) before vesicle scission (time 0 s). Average ± 95% confidence interval for Sla2-F40 force sensor in *myo5Δ* cells (n=67) is shown. FRET ratio signal of the respective Sla2-F40 force sensor measured in wild-type cells (blue) is the same as in Fig. 10A. Complete data provided in Supplementary Table S6.

First, we decided to follow Sla2-F40 sensor in cells absent of force-generating protein myosin Myo5. Myosin Myo5 has a motor domain that uses ATP hydrolysis to move on actin filaments. Besides, it anchors to the membrane through its TH1 domain and, together with Vrp1, it activates Arp2/3-mediated actin polymerization at the endocytic site (Lewellyn et al., 2015). However, as shown in Fig. 14, force transmitted through Sla2-F0 force sensor in *myo5Δ* cells did not significantly differ from the force profiles measured in wild-type cells. Yeast *Saccharomyces cerevisiae* contains two type IE myosins, Myo5 and Myo3, both of them involved in yeast endocytosis (Manenschijn et al., 2019). Our data thus suggest that Myo3 is able to fully substitute Myo5 function in endocytic force transmission or generation. As deletion of both myosin proteins leads to complete endocytic arrest (Geli and Riezman, 1996), their common contribution to force transmission cannot be studied by our system without a generation and test of specific partial loss-of-function mutants.

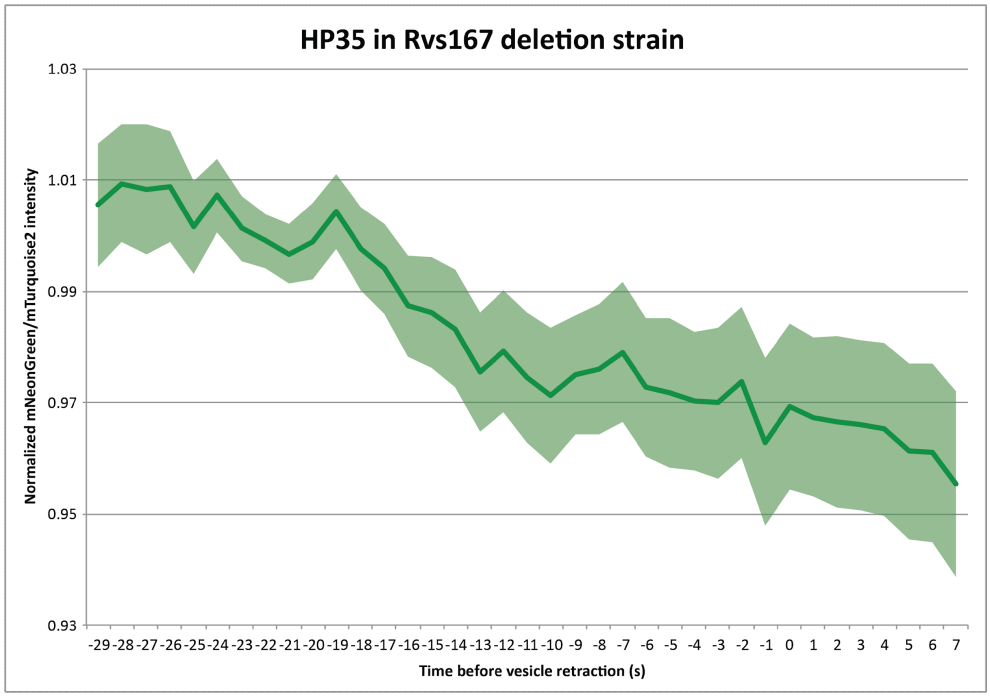

Figure 15 FRET ratio signal of Sla2-HP35 force sensor in strain deleted of Rvs167 protein (green). Time 0 indicates the furthest point of Sla2-HP35 sensor moving into the cytoplasm (see the text for details). Average ± 95% confidence interval for Sla2-HP35 force sensor in *rvs167Δ* (n=59) is shown. Complete data provided in Supplementary Table S7.

Deletion of membrane-remodeling BAR-domain protein Rvs167 induces the occurrence of retracting events, during which the membrane is presumably initially invaginated inwards but as this intermediate is not stabilized by Rvs161/167 heteropolymeric ring, it retracts back to the initial flat conformation without vesicle scission (Kaksonen et al., 2005; Kishimoto et al., 2011). We followed these events considering time 0 seconds as the

time point in which the membrane starts the retraction. During imaging, this point correlates to the time point when the Sla2 fluorescence is most remote from the cell cortex. During retractions, FRET ratio first decreased to values similar to values of wild-type cells until some 5 seconds before vesicle scission, indicating normal force transmission until this point. Then, FRET ratio plateaued even after the retraction occurred. This suggests that despite force is normally produced and transmitted over Sla2 during early membrane invagination, a proper membrane conformation and stabilization provided by BAR-domain proteins Rvs161 and Rvs167 is critical for productive force transmission prior to vesicle scission. Moreover, the absence of relaxation of Sla2-HP35 sensor after retraction suggests that the Sla2 molecules remain under tension bound to the actin cytoskeleton, which continues to polymerize after the abortive retraction (Fig. 15).

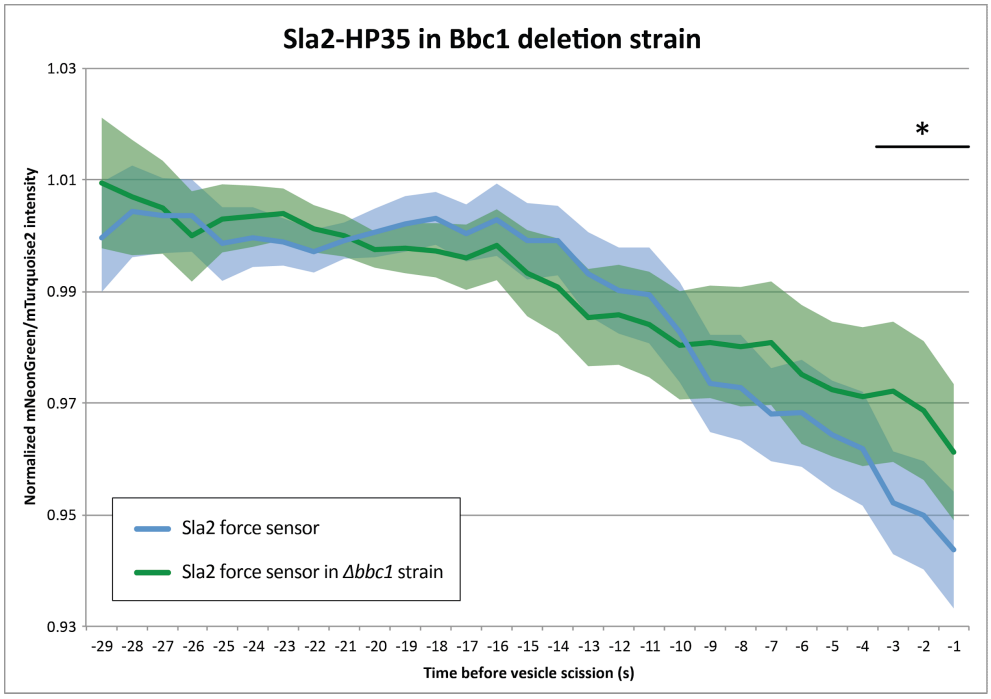

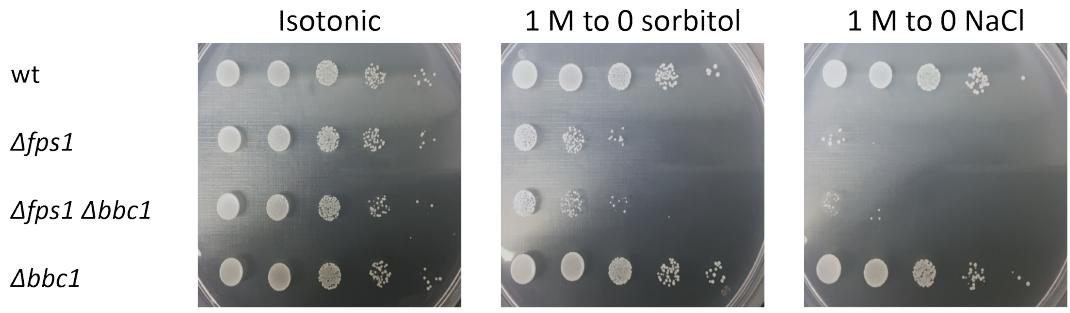

Figure 16 Role of Bbc1 protein in endocytic force transmission. (Top) FRET ratio signal of Sla2-HP35 force sensor in strain deleted of Bbc1 protein (green) before vesicle scission (time 0 s). Average ± 95% confidence interval for Sla2-HP35 force sensor in *bbc1Δ* (n=62) is shown. FRET ratio signal of respective Sla2-HP35 force sensor measured in wild-type cells (blue) is the same as in Fig. 10B. * Indicates statistically significant difference between indicated datasets ($p<0.05$) evaluated using two-tailed Welch's t-test. Complete data provided in Supplementary Table S8. (Bottom) Growth assays of *bbc1Δ* cells under hypotonic conditions. Ten-fold serial dilutions of strains containing indicated deletions were incubated on SD plates containing 1 M sorbitol (isotonic) and 1 M salt (not shown), or no sorbitol and no salt, respectively, for 1.5-2 days at 37°C degrees.

We also analyzed the role of the organization of the actin cytoskeleton in force transmission by following Sla2-HP35 in cells deleted of Bbc1. At the endocytic site, Bbc1 negatively regulates the activity of Las17, main actin nucleation-promoting factor in budding yeast. Deletion of Bbc1 induces increased actin polymerization at the endocytic site, causing faster and more distant release of the endocytic vesicle after scission (Picco et al., 2018). We followed force transmission in *bbc1Δ* cells and intriguingly detected less force transmitted over Sla2-HP35 force sensor compared to wild-type cells, specifically in the last phase of the endocytosis (Fig. 16A). This suggests that the enlarged dense endocytic actin cytoskeleton caused by Bbc1 deletion might directly physically remodel the invaginated membrane in a Sla2-independent manner. Consequently, lower force might be transmitted over the Sla2 force sensor.

Considering that Bbc1 deletion induces an enlarged actin network at the endocytic site, we decided to test whether this could be used by the endocytic machinery to generate extra force in specific situations. For this purpose, we performed growth assays with cells absent of Bbc1 under hypotonic conditions, which should intensify cell turgor pressure opposing endocytosis and therefore increase the force necessary to invaginate the membrane. We grew yeast cells on 1 M sorbitol and 1 M NaCl and then shifted to media containing no sorbitol or salt, inducing thus a hypotonic shock and increasing requirement of endocytic force. Additionally, we deleted the FPS1 gene to prevent the

adaptation to the hypotonic conditions. Yeast cells accumulate compatible solutes, glycerol mainly, as a general mechanism for cellular osmoregulation. These compatible solutes can be accumulated or secreted in order to adapt to changes in external osmolarity. Under hypotonic conditions, yeast cells open certain transmembrane channels and secrete these compatible solutes outside of the cell to reduce internal pressure. *Fps1Δ* cells are absent of the aquaglyceroporin channel, preventing thus the adaptation to hypotonic conditions by glycerol efflux (Tamás, 2002).

As shown in Fig. 16B, no difference in growth was observed between *fps1Δ* and the double mutant *fps1Δ, bbc1Δ* when shifted to media containing no sorbitol or salt, indicating that the excess of actin at the site of endocytosis induced by the absence of Bbc1 is not able to produce more mechanical force under hypotonic conditions.

Modification of the physical conditions can alter the force required for endocytosis

Next, we decided to study the importance of physical cues on force-dependent steps of endocytosis. Yeast cells have huge turgor pressure (0.4-0.8 MPa; Schaber et al., 2010), which represents the main mechanical barrier counteracting endocytic membrane reshaping. We aimed to counteract the high turgor pressure and therefore decrease the force required to invaginate the membrane during endocytosis by increasing the osmolarity of the medium. For this purpose, we followed force transmission during endocytosis on Sla2-HP35 after addition of hypertonic medium containing 250 mM or 500 mM sorbitol.

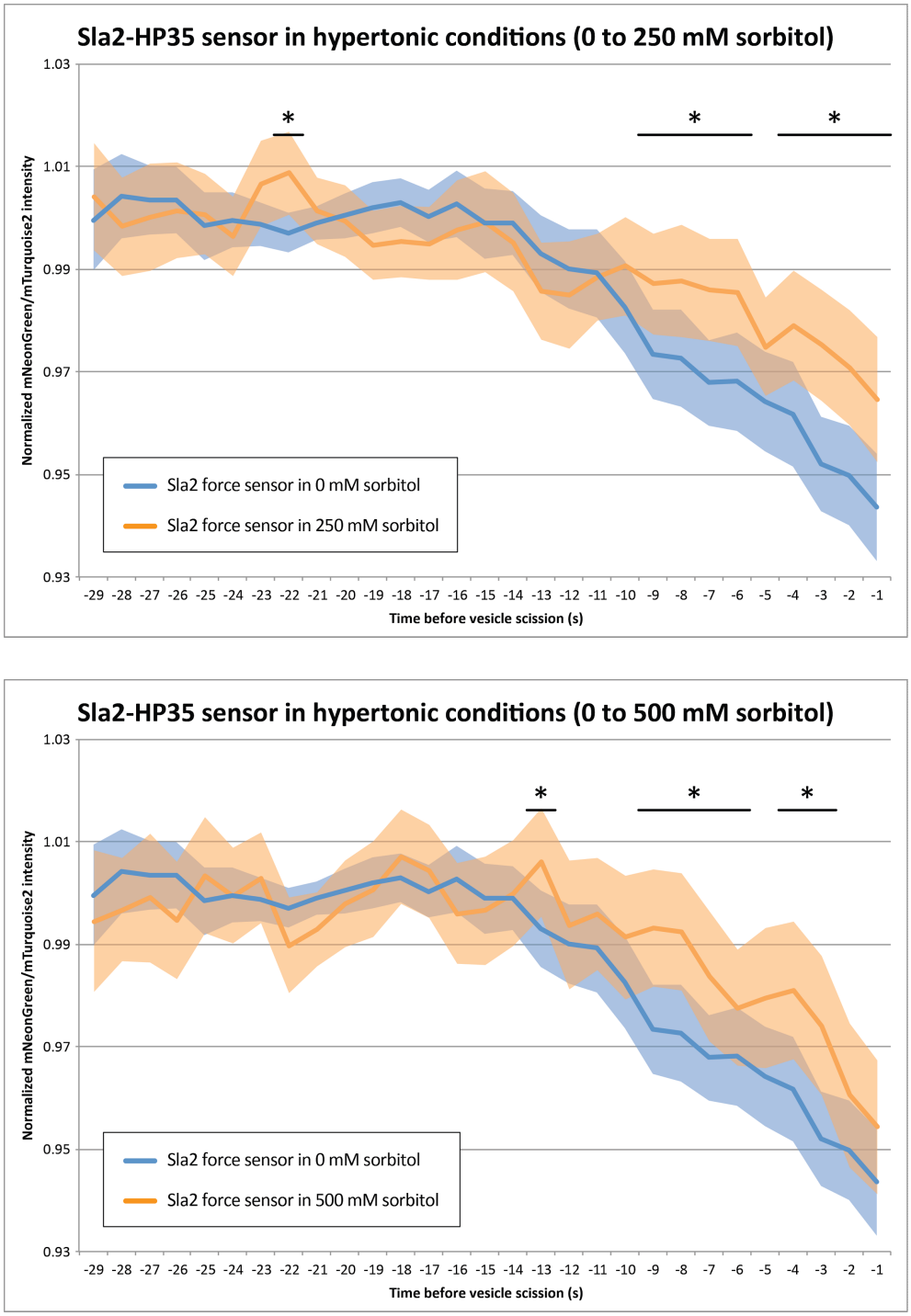

Figure 17 FRET ratio signal of Sla2-HP35 force sensor in indicated hypertonic conditions (orange) before vesicle scission (time 0 s). Average ± 95% confidence interval for Sla2-HP35 force sensor in 250 mM sorbitol (n=101) and in 500 mM sorbitol (n=80) are shown. FRET ratio signal of respective Sla2-HP35 force sensor measured in untreated cells (blue) is the same as in Fig. 10B. * Indicates statistically significant difference between indicated datasets ($p<0.05$) evaluated using two-tailed Welch's t-test. Complete data provided in Supplementary Tables S9 and S10, respectively.

Force transmitted through Sla2-HP35 force sensor was significantly reduced under conditions of reduced cell turgor established by addition of 250 mM sorbitol (Fig. 17A). This indicates that the high turgor pressure of yeast can be partially buffered by increased

external osmotic pressure and that force required for endocytosis can be reduced when a lower osmotic gradient is established across the plasma membrane. Similar results were obtained when we followed force transmission on Sla2-HP35 force sensor after addition of 500 mM sorbitol (Fig. 17B).

To support the observation that less force is required for endocytosis in cells with reduced turgor pressure, we employed a recently described approach to directly reduce yeast plasma membrane tension. We incubated yeast cells with palmitoylcarnitine (PalmC), a soluble lipid able to incorporate into the plasma membrane and reduce thus its tension (Riggi et al., 2018). Similarly to the sorbitol treatment, force transmission during actin-dependent steps of endocytosis was significantly reduced after incubation with 5 µM PalmC (Fig. 18). This suggests that force applied during endocytosis is also required to counter the high plasma membrane tension of yeast cells and that reduction of this tension eases force-dependent membrane reshaping during endocytosis.

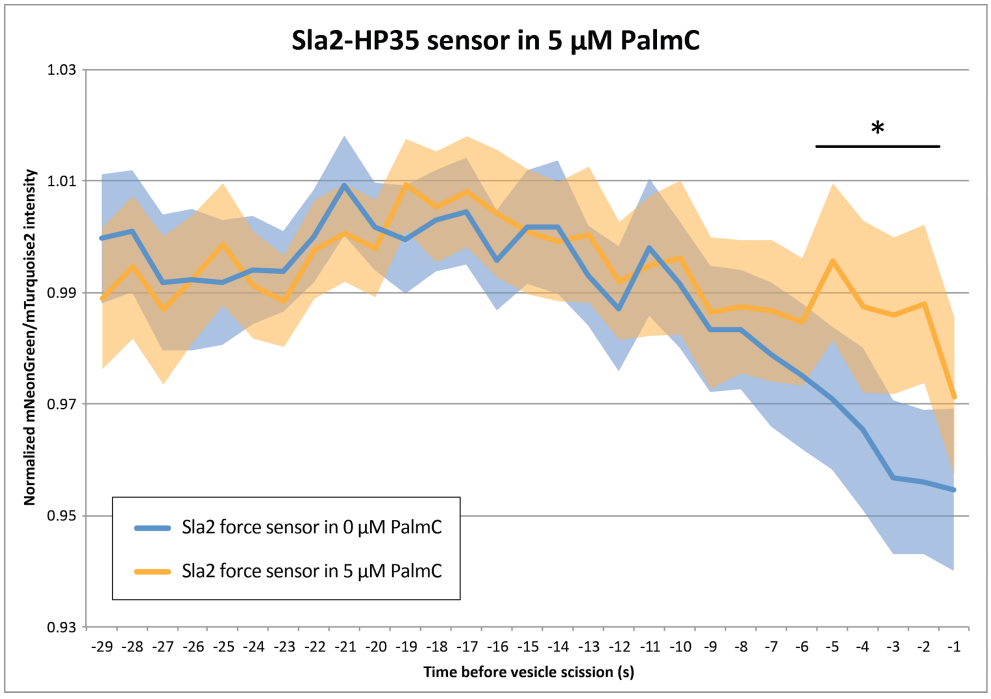

Figure 18 FRET ratio signal of Sla2-HP35 force sensor in reduced plasma membrane tension condition (orange) before vesicle scission (time 0 s). Average ± 95% confidence interval for Sla2-HP35 force sensor in 5 µM PalmC solution in DMSO (n=99), Sla2-HP35 force sensor HP35 in DMSO only (n=87) are shown. * Indicates statistical significance between indicated datasets ($p<0.05$) evaluated using two-tailed Welch's t-test. Complete data provided in Supplementary Table S11.

Altogether, cell turgor pressure and plasma membrane tension constitute important mechanical barriers to reshape the membrane during endocytosis in yeast cells and their reduction induced a decrease in force required for endocytic vesicle formation.

Finally, we decided to test the capacity of the endocytic force-generating machinery under hypotonic conditions, which should intensify cell turgor pressure opposing endocytosis. For this purpose, we exposed *fps1Δ* cells grown in medium with 1 M sorbitol to osmotic shifts made by exchange to media with lower osmolarity. As already mentioned, *fps1Δ* cells are absent of the aquaglyceroporin channel, preventing the adaptation to hypotonic conditions by glycerol efflux (Tamás et al., 1999). First, we tested dynamics of endocytosis in Sla2-HP35 cells incubated with 1 M sorbitol, which showed only slightly extended lifetime of Sla2 sensors compared to cells grown in medium without sorbitol (Sla2 FS lifetime 63.3 ± 3.5 s vs. 51.5 ± 3.7 s in medium without sorbitol; 83.5% of endocytic events completed during 4 min; Fig. 19). Then, we shifted cells to media of lower osmolarity containing only 0.5 M, 0.4 M and 0.25 M sorbitol and followed Sla2 lifetime and force transmission during endocytic events by Sla2-HP35 and Sla2-HP35st, respectively.

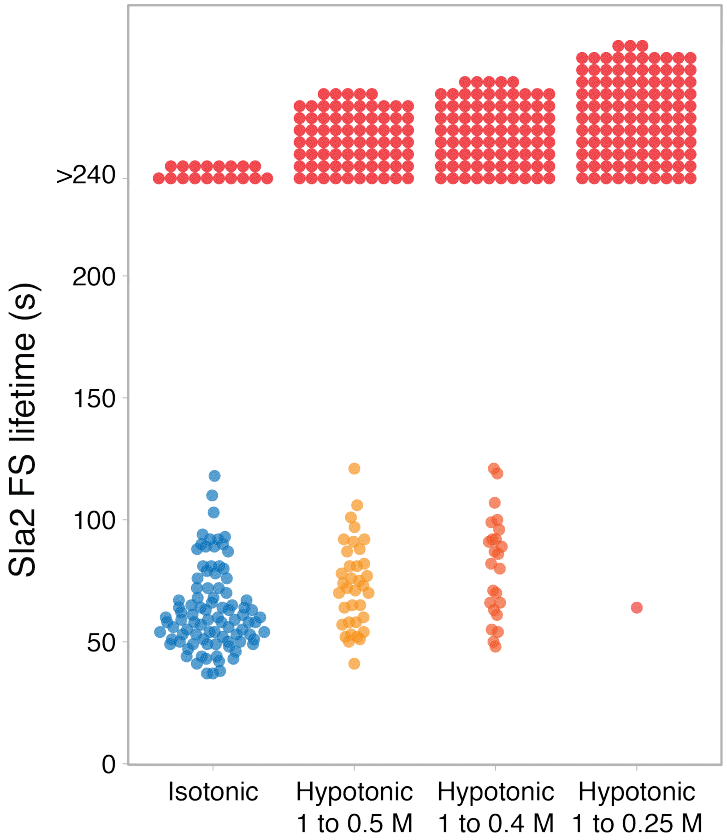

Figure 19 Lifetime of Sla2-HP35 at the endocytic site prior to vesicle scission on indicated conditions. Lifetimes in text as average ± 95% confidence interval of Sla2-HP35 in 1 M sorbitol n=109, Sla2-HP35 shifted from 1 to 0.5 M sorbitol n=111, Sla2-HP35 shifted from 1 to 0.4 M sorbitol n=109, Sla2-HP35 shifted from 1 to 0.25 M sorbitol n=114. Red-colored dots indicate endocytic events with lifetime longer than 4 min. Imaging settings to acquire mNeonGreen emission were identical for all constructs.

Cells shifted to 0.5 M sorbitol medium showed clear increase of stalled endocytic events with lifetime extending 4 min (32.4% of endocytic events completed during 4 min; Sla2 FS lifetime 73.2 ± 6.1 s; Fig. 19). When we focused on successful endocytic events in cells expressing Sla2-HP35st force sensor, likely not fully extended during endocytosis under normal conditions, we did not observe any difference in its FRET ratio in comparison to 1 M sorbitol medium (Fig. 20A). Same results were observed when we followed the FRET ratio of Sla2-HP35 under the same conditions (Supplementary Fig. S1). In comparison, Sla2-HP35st cells shifted to 0.4 M sorbitol medium showed slightly bigger, yet not significant, FRET ratio decrease compared to non-shifted cells incubated in 1 M sorbitol (Fig. 20B). At the same conditions, Sla2-HP35 lifetime increased and a higher percentage of endocytic events remained stalled during at least 4 min (Sla2 FS lifetime 81.0 ± 8.8 s; 22.0% of endocytic events completed during 4 min; Fig. 19). Finally, we aimed to follow

force transmission after shift to medium containing only 0.25 M sorbitol but the vast majority of endocytic events were stalled (>99% of endocytic events longer than 4 min; Fig. 19), preventing the potential FRET-based force analysis with Sla2-HP35st.

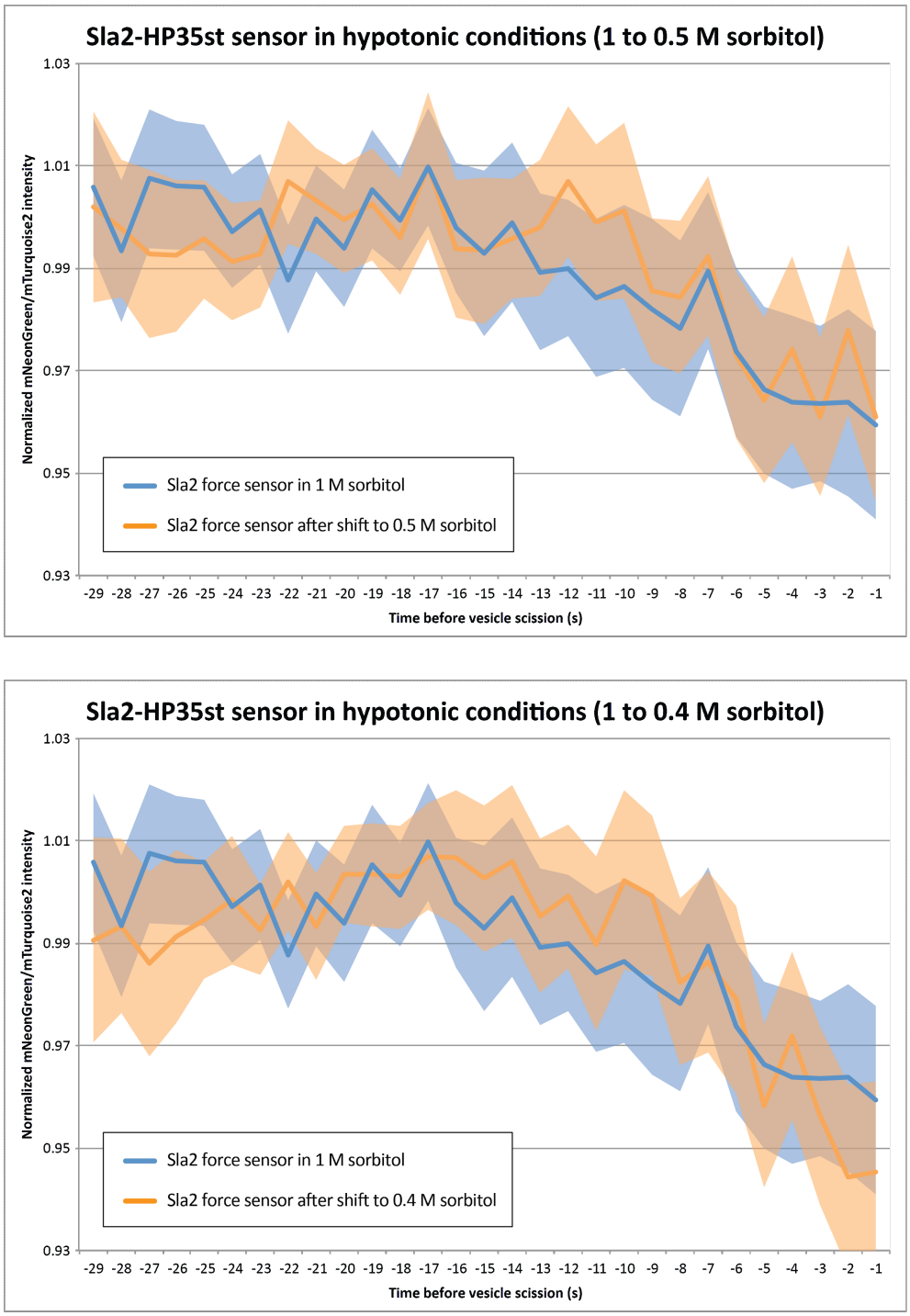

Figure 20 FRET ratio signal of Sla2-HP35st force sensor in cells incubated in 1 M sorbitol medium (blue) and after indicated osmotic shift (orange) before vesicle scission (time 0 s). Average ± 95% confidence intervals of Sla2-HP35st force sensor in cells incubated on 1 M sorbitol (n=64), Sla2-HP35st force sensor after 1 to 0.5 M shift (n=61), Sla2-

HP35st force sensor after 1 to 0.4 M shift (n=72) are shown. Complete data provided in Supplementary Tables S12 and S13, respectively.

Taken together, we observed a gradual increase of stalled endocytic events and no difference of force detected by Sla2-HP35st sensor after increased osmotic difference between the cell and the medium. This suggests that the polymerizing actin cytoskeleton cannot transmit more force under hypotonic conditions with increased force requirements.

DISCUSSION

The main goal of this project was to measure actin-generated forces required for endocytic vesicle formation in yeast *Saccharomyces cerevisiae*. This goal was achieved by the implementation of genetically-encoded FRET-based tension sensors F40, HP35, and HP35st into Sla2 protein, an essential molecular linker transmitting force from the actin cytoskeleton to the plasma membrane during endocytosis. These sensors allowed us to quantify a force around 10 pN transmitted over Sla2 protein during endocytic vesicle formation. Considering the number of force-transmitting Sla2 molecules per endocytic event, we could calculate the force provided by the actin cytoskeleton to be in range of 450-1330 pN per endocytic event.

Moreover, we followed force requirements of yeast endocytosis in strains absent of force-generator and actin polymerization activator myosin Myo5, endocytic membrane-sculpting protein Rvs167, and actin regulator Bbc1. We found that BAR-domain protein Rvs167 is critical for proper force-transmission in late stages of endocytosis and that the enlarged actin cytoskeleton induced by Bbc1 deletion might transmit force in a Sla2-independent manner, while it cannot produce more force under hypotonic conditions.

Remarkably, we also analyzed the force-dependent steps of endocytosis under various environmental conditions and found that force required for endocytosis can be lowered by decreasing cell turgor pressure and by reducing plasma membrane tension. Finally, experiments performed under hypotonic conditions indicated that the endocytic machinery and actin cytoskeleton can provide only limiting force for endocytosis in yeast.

Measurement of actin-generated forces transmitted via Sla2 protein

Insertion of FRET-based tension sensors F40, HP35, and HP35st into Sla2 protein made it possible to monitor forces applied on Sla2 protein during the course of endocytosis. Force appeared to be first applied some 13 seconds before vesicle scission, which correlated very well with the onset of actin polymerization at the endocytic site shown by the arrival of Abp1-mScarlet-I actin marker. This strongly supports the hypothesis that actin polymerization is responsible for force production during endocytosis.

All three force sensors, Sla2-F40, Sla2-HP35, and Sla2-HP35st, showed a similar starting point of FRET ratio change, which seemed to gradually decrease during the last 13 seconds before the pinching of the endocytic vesicle off. Since they sense different force ranges *in vitro*, this simultaneous beginning of gradual decrease in FRET ratio starting around 13 seconds before vesicle scission indicates that force is sufficiently high to extend all sensors from the onset of actin polymerization and also suggests that Sla2 molecules bind to the actin cytoskeleton in a stepwise manner during the growth of the polymerized actin cytoskeleton.

Sla2-F40 and Sla2-HP35 sensors, sensitive to 1-6 pN and 6-8 pN, respectively, showed an almost identical FRET ratio decrease, indicating that actin-driven force transmitted during endocytosis over Sla2 is sufficient to extend both sensors in a similar manner (higher than 8 pN per Sla2 molecule). Sla2-F40 extended to a lesser extend compared to Sla2-HP35, which could be explained by its shorter contour length resulting in lower dynamic range or by its force sensitivity to low force causing some Sla2-F40 molecules to be likely stretched even before actin-driven pulling force is applied (Fig. 6). Contrary, Sla2-HP35st force sensor, which requires the highest force to be extended, showed a lower decrease in FRET ratio. The almost identical characteristics of HP35 and HP35st (same fold, same contour length, and almost identical sequence; Ringer et al., 2017) allowed the direct comparison of their FRET profiles, which showed a significant difference in extension prior to vesicle scission between them. This strongly suggests that actin-driven force during endocytosis is not sufficient to extend HP35st sensor completely. HP35st is the sensor with the highest force required to extend, around 9-11 pN, and therefore sets the approximate value of force transmitted over Sla2 molecule during endocytosis. Considering that it showed approximately half drop in FRET ratio in comparison to Sla2-HP35, which we assumed to be extended completely, we calculated a force of 10 pN over Sla2 molecule. Taking into account the recently calculated number of Sla2 molecules per endocytic site to be between 45-133 molecules (Picco et al., 2015; Sun et al., 2019), around 450-1330 pN force is transmitted over Sla2 molecules during endocytosis. Moreover, considering the tip of the invagination as a hemispherical structure with an approximate radius of 12 nm (Kukulski et al., 2012), a simple calculation (pressure = force / surface) can estimate the pressure applied on the membrane during

invagination. In this case, a pressure between 0.25 and 0.73 MPa is applied on the invagination tip, in very good agreement with the range of calculated turgor pressure of yeast cells (0.4-0.8 MPa; Schaber et al., 2010) and therefore sufficient to invaginate the membrane.

It is important to note that our results are not in agreement with several computational studies suggesting that the highest pulling force during endocytosis is required for the initial stage of membrane bending, and then decreases over the growth of the invagination and subsequent neck stabilization. Later, force required increases again for vesicle scission (Walani et al., 2015; Dmitrieff and Nédélec, 2015). In contrast, our results indicate that actin-driven pulling force gradually increases, reaching the maximum force for vesicle scission (Fig. 10), further supporting our approach to measure forces required for endocytosis in the real cellular context.

In addition, the simultaneous start of gradual decrease in FRET ratio observed for all three force sensors suggests that the Sla2 molecules bind to actin gradually. A homogeneous population with all Sla2 molecules bound to the actin cytoskeleton from the start of actin polymerization and experiencing increasing pulling force from polymerizing actin would induce a delay in the start of the FRET ratio decrease between the force sensors used, which was not observed. Therefore, it is likely that only a small subset of Sla2 proteins is bound to the actin cytoskeleton at the beginning of force transmission 13 seconds before vesicle scission and that the amount of engaged transmitting proteins increases during the growth of the actin cytoskeleton until the vesicle pinches off, when presumably the majority of Sla2 molecules might be under the pulling force.

Despite the successful quantification of actin-driven force transmitted during endocytosis, all applied force sensors only cover a limited range of forces (1-11 pN). A force sensor sensitive to forces higher than 11 pN would provide better and more accurate resolution to quantify forces applied during endocytosis as well as other force-dependent cellular processes requiring higher force. In addition, this sensor would be the optimal non-extension force control.

In order to obtain high-quality FRET data, it is essential to select appropriate controls because FRET efficiency is not exclusively sensitive to the distance between the

fluorophores, but also to fluorophore orientation, temperature, pH, and other parameters (Ishikawa-Ankerhold et al., 2012). Therefore, not having correct controls can lead to inaccurate interpretation of experimental results.

In the case of FRET-based force measurements, three strategies can be applied to design proper no force controls. First, TSMs can be N- or C-terminally inserted into the protein of interest, preventing forces to be transduced to the TSM. However, the different insertion site compared to the force-sensing construct can potentially lead to different behavior of the TSM and therefore misinterpretation of the results. Second, the TSM can be inserted in the same position as in the force construct but truncating the rest of the protein after the insertion site, thus removing the force-transmitting domain of the protein of interest. This can only be achieved if the truncation does not impair the protein function, but guarantees the same microenvironment for the TSM. Finally, a third strategy consists of introducing point mutations or small deletions sufficient to abolish force transmission. In this control, the TSM is also exposed to the same microenvironment, and has the additional advantage that the protein structure might remain unaltered. However, it requires detailed understanding of the protein of interest (Cost et al., 2019). We applied the first and second strategies by designing Sla2 no force control and Sla2 no force ΔTHATCH control, respectively. FRET imaging showed no decrease in FRET ratio during endocytosis for none of both constructs, strongly suggesting that FRET ratio changes observed in Sla2 force sensor strains can be assigned to force-dependent FRET changes, and not conformational or intermolecular FRET changes eventually occurring during endocytic membrane invagination. In order to apply the third strategy, point mutations could be introduced into the actin-binding THATCH domain of Sla2 to prevent F-actin binding and thus force transmission. However, since actin-dependent force transmission is critical for endocytosis (Skruzny et al., 2012), this would require the presence of Ent1 ACB domain to restore membrane invagination at the endocytic site similarly to Sla2 no force ΔTHATCH control. Moreover, though *in vitro* studies revealed amino acids responsible for actin binding in human Hip1R THATCH domain (Brett et al., 2006), it remains unknown if the same residues in yeast Sla2 THATCH domain would perform the same function. Considering that this question is beyond the scope of this project, we implemented Sla2 no force ΔTHATCH control. In conclusion, a peptide linker sensitive to higher forces or a fully non-extensible peptide of similar contour length would provide

the optimal TSM for a no force control. With this hypothetic TSM, force could be still transmitted over Sla2 THATCH domain and no changes in FRET should be detected.

Contribution of endocytic proteins to force generation and transmission

In this study we also aimed to determine the contribution of selected endocytic proteins to force-dependent steps of endocytosis. For this, we followed force transmission by Sla2 FS in strains deleted of the force generator and actin polymerization activator Myo5, the membrane-sculpting BAR-domain protein Rvs167, and the actin polymerization inhibitor Bbc1.

Deletion of myosin Myo5 did not cause a significant difference in FRET ratio profile of Sla2 FS in comparison to wild-type cells. Yeast *Saccharomyces cerevisiae* contains two type IE myosins, Myo5 and Myo3, both of them involved in yeast endocytosis (Manenschijn et al., 2019). Our data suggests that the other myosin Myo3 alone is able to supply the role of both myosins in force-dependent endocytic steps. Since deletion of both myosins induces complete endocytic arrest (Geli and Riezman, 1996), a partial loss-of-function mutant of Myo3 in *myo5Δ* strain, or vice versa, could provide more details to better understand the role of myosins in force production/transmission.

In Rvs167-deleted cells, real-time imaging of endocytic markers suggests a significant fraction of endocytic sites starting to internalize but then retracting back to initial flat conformation without vesicle scission (so called retracting events; Kaksonen et al., 2005; Kishimoto et al., 2011). We followed Sla2 FS FRET ratio during retracting events upon deletion of the membrane-sculpting BAR-domain protein Rvs167 and observed a FRET ratio decrease similar to values observed in Sla2 FS in wild-type cells until some 5 seconds before vesicle scission. Then, the FRET ratio of Sla2 FS in *rvs167Δ* cells plateaued at this value, even after the retraction occurred and fluorescence signal bounced back to the plasma membrane. We hypothesize that while similar forces are applied over Sla2 during initial membrane bending and early invagination, proper membrane conformation provided by BAR-domain proteins is critical for productive force transmission prior to

vesicle scission. This might be in agreement with computational studies suggesting that the polymerization of BAR-domain proteins Rvs161 and Rvs167 around the invagination neck reduces the force required to invaginate the membrane (Walani et al., 2015). Therefore, actin-driven force might not be sufficient in some endocytic events of Rvs167-absent cells for vesicle scission, failing in pinching off and finally retracting to a flat membrane conformation. Moreover, our results suggest that the actin cytoskeleton is still bound and pulls on Sla2 after retraction. This hypothesis could be further confirmed by precise visualization of actin markers during retracting events.

At the endocytic site, Bbc1 is a negative regulator of actin polymerization. It contains a SH3 domain and a polyproline (PP) motif, which induce the inhibition of the Arp2/3-complex activators Las17 and Myo3/5 by interaction with their PP motifs and SH3 domain, respectively (Rodal et al., 2003; Mochida et al., 2002). Its deletion has been shown to induce enhanced larger actin nucleation during endocytosis, resulting in enlarged actin network and further movement of the formed endocytic vesicle into the cytoplasm after its scission, although the time required to create a vesicle does not change (Picco, 2018). FRET measurement in *bbc1Δ* strain unexpectedly showed less force transmitted over Sla2 force sensor compared to wild-type cells, specifically during the last 3 seconds before scission. This suggests that the enlarged actin cytoskeleton at the endocytic site caused by Bbc1 deletion might be able to directly transmit force to the membrane in a Sla2-independent manner. We then observed that the enlarged actin cytoskeleton induced in Bbc1-deleted cells was not able to recover the growth defect induced in hypotonic conditions. This suggests that Bbc1 is not a negative regulator of the force-generating machinery at the endocytic site which function could eventually be inactivated under hypotonic conditions to increase force production. Bbc1 arrives at the endocytic site around 10 seconds before vesicle scission, and Las17 arrives at the endocytic site 20 seconds before Bbc1 (Lu et al., 2016). Recent superresolution imaging revealed the lateral organization of endocytic proteins and found that Las17 forms a ring surrounding the invagination with a radius of around 70 nm, which is significantly expanded upon deletion of Bbc1. In presence of Bbc1, which locates in an outer ring of approx. 98 nm, Las17 remains tethered in an inner ring during the invagination progression (Mund et al., 2018). Together with our data suggesting that Bbc1 deletion does not enhance force production capacity, Bbc1 function might be to keep Las17 in proper position to effectively channel

actin polymerization inwards, which could represent the most effective way to utilize actin-driven force produced during endocytosis.

Deletion of Bbc1 induces an enlarged actin network at the endocytic site, which requires additional ATP energy for its polymerization and therefore could represent an unnecessary waste of energy for the cell. A previous study measured the number of molecules of actin-marker protein Abp1 and the size of the ribosome exclusion zone induced by the actin cytoskeleton at the endocytic site and found an increase of 77% and 68% (assuming the exclusion zone as a cylinder), respectively, in *bbc1Δ* cells compared to wild-type cells (Picco et al., 2018). These results strongly indicate that Bbc1 main function might be to regulate Las17 to efficiently channel actin polymerization and prevent the misuse of energy used for actin polymerization during endocytosis.

Role of physical conditions in endocytic force requirements

In order to understand how the physical cues can affect the force requirements during endocytosis in yeast cells, we followed Sla2 force sensor in cells under conditions of increased extracellular osmotonicity and decreased membrane tension. Besides, we also tested the force-generating potential of the endocytic machinery by following endocytosis under hypotonic conditions.

As other cell-walled organisms, yeast cells have higher turgor pressure compared to animal cells, which makes actin-driven force an absolute requisite for membrane bending during endocytosis. This high turgor pressure counteracts the force needed to invaginate the plasma membrane for endocytosis (Aghamohammadzadeh and Ayscough, 2009). Thus, we decided to increase the external osmotic pressure to test whether force requirements could be lowered. We incubated cells with sorbitol-containing medium and observed less force transmitted over Sla2 during actin-dependent steps of endocytosis. This indicates that the high turgor pressure of yeast cells can be partially compensated by increased external pressure resulting in less force required for endocytosis. This also proves previous hypothesis that sorbitol treatment could counteract the high turgor pressure as observed by the endocytic rescue phenotype observed in several endocytic mutants or after mild actin inhibition (Basu et al., 2014).

Concomitantly with high turgor, yeast cells also have high plasma membrane tension, which was suggested to be a major cause of actin dependency of endocytosis in mammalian cells (Boulant et al, 2011). To test whether force requirements for membrane invagination depend on membrane tension, we aimed to decrease it by addition of soluble lipid PalmC (Riggi et al., 2018). Under this condition, we observed less force transmitted over Sla2, suggesting that decreased plasma membrane tension lowers the force requirements to invaginate the membrane.

Altogether, these results indicate that actin-driven force is essential in yeast endocytosis to counteract the high turgor pressure and high plasma membrane tension. Also, it indicates that force requirements to invaginate the membrane during endocytosis significantly depend on the tonicity of the cell environment, which can influence the total amount of force required to reshape the membrane.

In addition, we analyzed the capacity of the endocytic actin-based force-generating machinery by following force transmission under hypotonic conditions, which intensify cell turgor opposing the inwards movement of the plasma membrane during endocytosis. We induced osmotic shifts in cells deleted of the aquaglyceroporin Fps1, which cannot adapt to hypoosmotic conditions by secretion of the osmo-protectant glycerol. Following Sla2 lifetime at endocytic sites, we found an increasing number of stalled endocytic events with the gradual increase of osmotic shift, leading to almost complete endocytic arrest after shift from 1 M to 0.25 M sorbitol media. Notably, force FRET profiles of successful endocytic events showed no difference compared to cells not shifted to hypotonic conditions. Taken together, this suggests that the endocytic machinery is either not able to produce extra force under hypotonic conditions, leading to an increasing number of stalled endocytic events observed with the gradual increase of osmotic shift, or that Sla2-actin connection cannot sustain such extra force. This is in agreement with previous results suggesting that Sla2-Ent1 linker might fail to transfer the actin-driven force to the plasma membrane under increased plasma membrane tension (Riggi et al., 2019). This adaptor-actin connection might be even less effective in the absence of Ent1 actin-binding domain ACB, whose deletion does not show any phenotype under normal conditions but could represent a disadvantage in conditions when higher force is required.

We hypothesize that to perform the critical endocytic process under hypotonic conditions, probably very common in constantly changing natural environments, yeast cells react by other means. First, the cell rapidly opens Fps1 channels to export glycerol to adapt to lower osmolarity. Besides, gene expression is regulated to adjust cell surface properties through the cell wall integrity (CWI) pathway (Hohmann, 2002). Only when the homeostatic osmotic level is at least partly restored, endocytosis can be revived.

FRET-based endocytic force measurement limitations and project future directions

Despite the potential of FRET-based force measurements to study the role of specific endocytic factors in force transmission, it should be recognized that it comes with certain limitations to be considered. First, a synthetic enhancement phenotype was observed after deleting selected endocytic proteins. Even though Sla2 FS and Sla2 NF constructs showed full complementation of growth defect of Sla2 deletion and no significant difference was observed for Sla2 FS lifetime compared to C-terminally-tagged Sla2 (Fig. 9A and Fig. 9B, respectively), some deletion strains showed an enhanced phenotype in comparison to the one expected for strains containing wild-type Sla2 protein. The strain with deletion of BAR-domain protein Rvs167 was reported to successfully internalize more than 70% of endocytic events and fail and retract roughly around 20% (Kishimoto et al., 2011). We imaged our Sla2 FS strain in *rvs167Δ* background and found that almost all endocytic events were stalled for longer than 75 seconds (less than 1% of events completed, data not shown), precluding the measurement of force transmission in successful events. Similarly, we also aimed to measure force transmission in cells deleted of the actin filaments crosslinking protein Sac6. This strain was previously reported to suffer a severe endocytic phenotype, with only 6.5% and 15% of successful and retracted events, respectively (Picco et al., 2018). The introduction of Sac6 deletion into our Sla2 FS strain induced a severe growth defect and complete block of endocytosis, preventing thus force measurement (data not shown).

Second, force transmission over Sla2 protein in deletion strains might not change even though the deleted endocytic factor is involved in force generation or transmission. Force

required to invaginate the membrane during endocytosis in yeast cells is mainly to overcome the high turgor pressure (Nickaeen et al., 2019). This physical barrier is largely independent to the endocytic coat composition, so upon deletion of specific endocytic factors related to force generation, cells might find alternative pathways to finally produce the same amount of force required to reshape the membrane. In such case, force transmission over Sla2 FS might be identical, but it might come from different sources or transduced in a different manner, not detectable with our system.

Finally, the implementation of an automatized tracking method would permit the force measurement of numerous strains in a fast manner. In this study, tracking of endocytic events was carefully performed manually to ensure reliable selection and proper time alignment of successful endocytic events. However, manual tracking is time-consuming and limits the amount of strains and conditions that can be analyzed. An example of this is force transmission in cells deleted of myosin Myo3/5. As previously discussed, partial loss-of-function mutations should be implemented on the remaining myosin in order to observe some effect on force transmission. Since several partial loss-of-function mutations have been suggested in the different domains of myosin proteins, an automatized system would be required for a relatively fast screen of the mutants. Similarly, the implementation of an automatic analysis protocol would also allow assessing the impact of plasma membrane composition on force requirements. It would be possible to screen for strains with e.g. regulated expression of lipid-modifying enzymes and follow force transmission over Sla2 FS. For instance, $PI(4,5)P_2$ and sphingolipids have been related to endocytosis (Souza and Pichler, 2007), so it would be of remarkable interest to observe force transmission under altered membrane composition. Finally, it would also be of high interest to follow force transmission over Ent1 protein: whereas human Sla2, Hip1R, forms homodimers *in vitro* (Engqvist-Goldstein et al., 2001) and has a more rigid and defined structure, a relevant part of epsin Ent1 is natively unfolded, which provides this protein certain flexibility. Moreover, the number of Ent1 molecules is higher at the endocytic site compared to Sla2. This might distribute the total actin-driven force among more linkers so the force per Ent1 molecule should therefore be lower. In such case, tension sensors F40, HP35, and HP35st could more precisely resolve the force required for endocytosis.

Concluding remarks

Mechanobiology has been of increasing interest in the last decade due to evidence found that mechanical inputs are converted into biochemical signals and therefore play a central role in physiological and pathological conditions. This is also the case for clathrin-mediated endocytosis in budding yeast, in which actin-driven forces are essential to compensate the high turgor pressure and reshape the membrane.

The main goal of this project was to measure actin-generated forces required for endocytic vesicle formation in yeast. We provide the first experimental evidence reporting real force values transmitted during endocytosis *in vivo*. Using FRET-based force sensors, we calculated a force around 10 pN per Sla2 molecule during endocytosis, which indicates that actin transmits a total force of 450-1330 pN per endocytic event.

We could show the effect of selected endocytic proteins in force-dependent steps of endocytosis by following force transmission in deletion strains. We could also provide empirical proof that hypertonic conditions induce a lessening in force requirement for endocytosis, which had been hypothesized previously. And finally, we observed the limitations of the endocytic machinery and actin cytoskeleton to provide enough force for endocytosis under hypotonic conditions.

Importantly, we showed that FRET-based force measurement is sensitive enough to measure force transmission over time during endocytosis, even when following the relatively low copy-number protein Sla2, calculated to be in the range of 45-133 molecules at the endocytic site (Picco et al., 2015; Sun et al., 2019). Moreover, tension sensors are suitable to follow mechanical forces at the very subcellular level, resolving force applied on endocytic invaginations, typically around 100 nm long and 50 nm wide in yeast (Kukulski et al., 2012).

We hope that our data will help to better mechanistically understand the endocytic process. Our experiments represent a starting point to elucidate the role of other force-generating and force-transmitting proteins involved in endocytosis. Moreover, the knowledge of force requirements during endocytosis and the role of specific physical cues on force-dependent steps of endocytosis will contribute to develop more accurate models of membrane reshaping processes during endocytosis. This information is crucial not only

for the endocytic pathway but also for understanding other essential cellular membrane reshaping processes, as well as other cellular events carried out by the actin cytoskeleton.

MATERIALS AND METHODS

Yeast strains and plasmids

Yeast strains and plasmids are listed in Tables 8 and 9, respectively. *Saccharomyces cerevisiae* with strain MSK002 isogenic to S288C strain was used as wild-type. Strains were grown at 25°C or 30°C in standard rich medium YPD or synthetic defined (SD) medium with appropriate supplements. Media were supplied with 100 µg/mL clonNAT, 300 µg/mL G418 and/or 240 µg/mL hygromycin B when applicable.

Plasmids used for yeast expression were derived from pRS416 (Sikorski and Hieter, 1989), yeast shuttle vector containing uracil auxotrophic marker (*URA3*) for yeast and ampicillin selection marker (*AmpR*) for bacteria.

Promoter and coding sequence of *Saccharomyces cerevisiae SLA2*, together with sequence coding for HA-tag, were PCR-amplified and cloned using *SacI-AscI* and *AscI-XmaI* sites, respectively, into pRS416 vector, creating pRS416-*SLA2*-2xHA plasmid. For Sla2 force sensors, tension sensor modules were inserted into *SLA2* in plasmid after *SLA2* codon 702. *SgrAI-XbaI* restrictions sites were first created after this position by overlapping PCR (additional codons for Thr-Gly and Ser-Arg were therefore created). Construction of the tension sensor module F40 (mTurquoise2-F40 linker-mNeonGreen sequence) was achieved by overlapping PCR. Genes coding for fluorophores mTurquoise2 and mNeonGreen were amplified from plasmids pFA6a-mTurquoise2-hphNT1 and pFA6a-mNeonGreen-kanMX6, respectively, with primers introducing F40 linker in between them with *XmaI-XbaI* overhangs. PCR fragment was digested with *XmaI-XbaI* enzymes and cloned into *SgrAI-XbaI* sites of pRS416-*SLA2*-2xHA vector. Sla2 no force control plasmids were constructed following the same protocol, introducing first *XmaI-XbaI* sites between *SLA2* sequence and HA tag. To create the second Sla2 no force control (*SLA2ΔTHATCH* NF plasmid), *SgrAI-XbaI* restrictions sites were again created after position for amino acid 702 by overlapping PCR not amplifying the remaining sequence of *SLA2*. F40 tension sensor module was PCR amplified, digested using *XmaI-XbaI* restriction sites and cloned into pRS416-*SLA2ΔTHATCH*-2xHA plasmid. Later, HP35 and HP35st sequences were synthetized commercially (IDT) and exchanged with F40 sequence (using *SpeI* and *AgeI*

sites generated by codon optimization inside F40 sequence) in plasmids by digestion and ligation.

Table 3 DNA sequences used in this study for linker peptides F40, HP35, and HP35st.

Linker Peptide	DNA sequence (5'-3')
F40	GGGCCCGGTGGGGCGGGTCCGGGCGGTGCAGGTCCTGGTGGCGC GGGTCCAGGGGGTGCTGGTCCAGGTGGCGCCGGGCCTGGTGGGG CCGGCCCAGGTGGTGCCGGTCCAGGTGGTGCA
HP35	TTGTCAGACGAGGATTTTAAGGCAGTGTTTGGAATGACAAGGA GTGCTTTTGCTAATCTTCCACTTTGGAAGCAACAGAATCTAAAG AAAGAGAAAGGTCTATTT
HP35st	CTGTCTGATGAAGACTTCAAAGCTGTTTTTGGTATGACTAGAA GTGCATTTGCCAACCTACCTCTATGGAAACAGCAAGCGCTAATG AAGGAAAAGGGACTTTTC

Integration, deletion, and tagging of yeast genes were made by homologous recombination of respective genes with PCR cassettes (Janke et al., 2004). For this, PCR cassettes were amplified from respective plasmids with primers containing 40-60 base pairs homologous to desired chromosomal loci (S1, S2, S3 primers, see Table 10). PCR cassettes or plasmids were transformed into yeast cells using standard lithium acetate (LiAc) transformation protocol.

Gene deletions, integrations, tagging, and *Escherichia coli* plasmids transformations were verified by colony PCR, locating the first primer in the targeted locus and the second primer in the transformed cassette. Integration of constructs into yeast genome was verified using DNA Sanger sequencing (Microsynth). For this, genomic DNA was first obtained using YeaStar Genomic DNA Kit (Zymo Research) and the desired fragment was then amplified by PCR and purified using GeneJET PCR Purification Kit (Thermo Fisher Scientific).

Once validated by sequencing and/or colony PCR, yeast strains were conserved on glycerol solution at -80°C. For this purpose, fresh yeast cells were grown overnight in YPD medium. 1 mL of grown culture was mixed with 0.5 mL of 45% glycerol (w/v) for a final concentration of 15% glycerol (w/v) and stored in CryoPure tubes (Sarstedt). Tubes were

frozen at -20°C for 24 hours before long-term storage at -80°C. For growth assay, strains were grown on SD medium plates for 24 hours and diluted to Optical density $(OD)_{600}$ 0.6 in sterile deionized H_2O (dH_2O). Four ten-fold serial dilutions were prepared in sterile dH_20 and 10 µL were spotted on indicated plates.

PCR protocols

Two different DNA polymerases were used in this study. PrimeStar GXL DNA Polymerase was used to amplify DNA fragments for genome integration and DNA cloning. MangoMix was used to test genome-integrated DNA cassettes and plasmids transformation by colony PCR. PCR reactions were performed in a Peqstar Thermocycler, PeqLab. The following reaction mixtures and PCR programs were used:

Table 4 PrimeStar GXL DNA Polymerase reaction conditions.

Component	Quantity
5x PrimeStar GXL buffer	10 µL
dNTP mixture (2.5 mM each)	4 µL
Forward primer (100 µM)	0.2 µL
Reverse primer (100 µM)	0.2 µL
DNA template	0.1-10 ng
PrimeStar GXL DNA polymerase	0.5 µL
Sterile dH_2O	To final reaction volume of 50 µL

Table 5 PrimeStar GXL DNA Polymerase PCR program.

Step	Temperature	Time	Cycles
Denaturation	98°C	10 s	
Annealing	55 or 60°C	15 s	33 cycles
Extension	68°C	1 min/kb	

Table 6 MangoMix reaction conditions.

Component	Quantity
MangoMix	12.5 µL
Forward primer (100 µM)	0.25 µL
Reverse primer (100 µM)	0.25 µL
Sterile dH_2O (with resuspended yeast/bacteria cells)	12 µL

Table 7 MangoMix PCR program.

Step	Temperature	Time	Cycles
Initial denaturation	95°C	10 min (yeast) 5 min (bacteria)	
Denaturation	95°C	30 s	34 cycles
Annealing	55°C	25 s	
Extension	72°C	15-30 s/kb	
Final extension	72°C	6 min	

Recombinant DNA

For DNA cloning, standard DNA restriction endonucleases and ligase were used following manufacturer instructions. In general, digestions were performed at 37°C using CutSmart® buffer (New England Biolabs). When available, High-Fidelity (HF®) enzymes were used. DNA fragments were separated on 1% agarose (Sigma-Aldrich) gel in TAE buffer at 100-130 V and purified using GeneJET Gel Extraction Kit (Thermo Fisher Scientific). Ligations were performed incubating DNA mixes at room temperature and at 16°C using T4 DNA Ligase (New England Biolabs). Ligation mixes were transformed into chemically competent DH5α *Escherichia coli* cells, either self-prepared or commercial (New England Biolabs), following a heat-shock protocol. 50 µL of chemically competent cells were mixed with 5 µL of ligation mix and incubated on ice for 30 min. Cells were heat-shocked for 30 seconds at 42°C and incubated on ice for 5 min. Cells were then mixed with 950 µL of LB medium (or SOC outgrowth medium for commercial cells) and incubated by shaking at 37°C for 45 min prior to plating on 100 µg/mL ampicillin-

containing LB plates. After overnight growth at 37°C, isolated colonies were incubated in LB medium with 100 µg/mL ampicillin for 12-16 hours and plasmid was isolated using GeneJET Plasmid Miniprep Kit (Thermo Fisher Scientific).

Preparation of competent *E. coli* cells

Fresh DH5α *Escherichia coli* cells were grown by overnight shaking at 37°C in rich LB medium. 1 mL of inoculum was diluted to 100 mL LB medium and cells were grown by shaking at 37°C to OD_{600} 0.5. Cells were cooled down on ice for 10 min, transferred to 50 mL tubes and centrifuged at 3000-5000 revolutions per minute (rpm) for 10 min at 4°C. Cells were softly resuspended in cold Tfb1 solution and finally diluted with 15 mL of it. Subsequent to 10 min incubation on ice, cells were centrifuged at 3000 rpm for 5 min at 4°C. Cells were softly resuspended in 2 mL cold Tfb2 solution. Aliquots of 50-100 µL were prepared on pre-chilled 1.5 mL tubes and immediately frozen in liquid nitrogen before storage at -80°C.

Yeast transformation

Fresh yeast cells were inoculated and shaken in YPD medium overnight and then diluted to OD_{600} 0.05-0.1. Cells were grown to OD_{600} 0.5-0.9 in YPD medium (10 mL culture per transformation), washed with ½ volume of sterile dH_2O, ⅕ volume 0.1 M lithium acetate and resuspended in 0.1 M lithium acetate (100 µL per transformation). 100 µL of cell suspension were mixed in a 2 mL tube with 7 µL freshly denatured single-stranded DNA (salmon sperm DNA, Sigma-Aldrich), DNA (PCR product: 7-15 µL. Plasmid: >50 ng) and 300 µL 40% PEG solution (40% PEG 3350 w/w in 0.1 M LiAc; Sigma-Aldrich). Samples were gently mixed and incubated for 30 min at 30°C and heat shocked for 15-20 min at 42°C. Mixes were then washed with 1 mL sterile dH_2O to remove excess of PEG solution. Finally, cell pellets were resuspended in the desired amount of sterile dH_2O and plated on indicated auxotrophic plates. For antibiotic resistance selection, cells were resuspended in 2 mL of YPD and incubated 3-4 hours at 30°C or overnight at 25°C prior to plating.

Microscopy

To perform FRET, a wide-field Eclipse Ti-E inverted fluorescence microscope (Nikon) equipped with X-Cite Exacte LED light source, Perfect Focus System (PFS), and NIS-Elements AR software (4.40; Nikon) was used. Images were acquired with Nikon 100x Plan Apo λ NA 1.45 oil immersion objective and iXon 897-X3 EM-CCD camera (Andor) with EM gain set up to 250.

For sample preparation, strains were grown to log phase in low fluorescence SD-Trp, -Ura medium (prepared from LoFlo YNB, Formedium). Cells were attached to Concanavalin A-coated (ConA, Sigma-Aldrich) 8-well glass coverslips (ibidi), which was achieved by 5-10 min incubation with 0.1 mg/mL ConA solution and subsequent washing with medium, and observed at 20 °C.

For hypertonic sorbitol treatment, cells were grown in SD-Trp, -Ura medium and shifted to SD-Trp, -Ura, 250 mM sorbitol. Cells were observed for 10 min, 5 min after shift to medium with sorbitol. For cells shifted to medium containing 500 mM sorbitol, same protocol was applied and cells were observed for 10 min, 15 min after shift to medium with sorbitol. For PalmC treatment, 5 mM PalmC solution was prepared in DMSO and diluted 1:1000 in SD-Trp, -Ura to obtain a final concentration of 5 µM PalmC. Cells were grown in SD-Trp, -Ura medium and then shifted to SD-Trp, -Ura, 5 µM PalmC medium, where they were incubated for 35 min and imaged for 10 min. Respective negative control was imaged on SD-Trp, -Ura, 0.1% DMSO following the same protocol. For hypotonic treatment, cells were first grown overnight in SD-Trp, -Ura, 1 M sorbitol and shifted to lower osmolarity medium SD-Trp, -Ura containing 0.5, 0.4 or 0.25 M sorbitol. Cells were imaged for 30 min, 30 min after medium shift.

Ratiometric FRET

For ratiometric FRET, FRET donor mTurquoise2 was excited using 436/20 excitation filter (Chroma) and donor and acceptor fluorescence was simultaneously collected using an image splitter (Optosplit II, Cairn) equipped with appropriate filters for mTurquoise2 (472/30) and mNeonGreen (542/27) and a dichroic mirror of 520 nm. For every strain,

3-5 independent sessions each one consisting of typically 8-15 acquisitions of 75 seconds streams of 1-s exposures were performed.

Images were analyzed with ImageJ software (Schneider et al., 2012). Images were subtracted of general background, corrected for photobleaching and individual endocytic events were then manually tracked using TrackMate plugin (Tinevez, 2016). Time alignment of endocytic events was performed taking vesicle scission as a reference point (time 0 seconds) characterized by rapid cytoplasmic movement of the fluorescence signal. Normalization for each individual track was performed using the average of FRET ratio values between times -25 to -17 seconds, where mTurquoise2 and mNeonGreen fluorescence intensities and their ratios remained largely unchanged. In total 58-121 endocytic patches (of approx. 55-115 cells) longer than 20 seconds were used for averaging and obtaining the FRET ratio profile.

Live-cell imaging

For live-cell imaging, the following filter sets were used to acquire mNeonGreen (Ex 504/12, dc 520, Em 542/27) and mScarlet-I (Ex 585/29, dc 605, Em 647/57) fluorescence (Chroma, Semrock). For Sla2-mNeonGreen lifetime quantification, mNeonGreen fluorescence was followed for 4 min with 1 second frame rate. For Abp1-mScarlet-I lifetime quantification, mScarlet-I fluorescence was followed for 4 min with 500 ms frame rate. For both experiments, 5-7 acquisitions were taken.

Acceptor photobleaching FRET

For acceptor photobleaching, 60x Plan Apo λ NA 1.45 oil immersion objective and 1.5x tube lens were used. Two acceptor- and three to five donor-channel (mNeonGreen and mTurquoise2, respectively) images were taken before photobleaching of the acceptor by 3-5 seconds pulse of 150 mW 515 nm solid-state laser (CNI) followed by three to five donor- and two acceptor-channel images.

Images were analyzed with ImageJ software (Schneider et al., 2012). Images were subtracted of general background and endocytic patches of each photobleached cell were then manually selected by polygon selection tool. FRET efficiency (calculated as percentage increase in donor fluorescence after acceptor photobleaching) was calculated using FRETCalc plugin (Stepensky, 2007) with the intensity threshold set up to the level of cytoplasmic fluorescence of the analyzed cell. At least 6 cells (each contributing by multiple endocytic patches) of two independent clones were used to calculate mean FRET efficiency.

Statistics and reproducibility

Sample sizes were based on previous quantitative fluorescence microscopy studies of yeast endocytosis (Picco et al., 2015; Sun et al., 2019) and on protocols for FRET-based TSM microscopy (Cost et al., 2019).

Two-tailed Welch's t-test for unpaired datasets of uneven variances was used to compare identical time points of indicated datasets.

Table 8 Strains used in this study.

Strain	Description	Genotype
MSK002	Wild-type, MATα	MATα, *his3Δ200, leu2-3,112, ura3-52, lys2-801*
MSK035	Sla2 deletion	MATα, *his3Δ200, leu2-3,112, ura3-52, lys2-801, sla2Δ::natNT2*
MSK438	Ent1 ACB deletion	MATα, *his3Δ200, leu2-3,112, ura3-52, lys2-801, ent1ΔACB::kanMX6*
MSK439	Ent1 ACB deletion, Sla2-F40 FS	MATα, *his3Δ200, leu2-3,112, ura3-52, lys2-801, ent1ΔACB::kanMX6, sla2(1-2106)-mTq2-F40-mNG-sla2end::URA3*
MSK440	Ent1 ACB deletion, Sla2-HP35 FS	MATα, *his3Δ200, leu2-3,112, ura3-52, lys2-801, ent1ΔACB::kanMX6, sla2(1-2106)-mTq2-HP35-mNG-sla2end::URA3*
MSK441	Ent1 ACB deletion, Sla2-HP35st FS	MATα, *his3Δ200, leu2-3,112, ura3-52, lys2-801, ent1ΔACB::kanMX6, sla2(1-2106)-mTq2-HP35st-mNG-sla2end::URA3*
MSK443	Ent1 ACB deletion, Sla2 NF F40	MATα, *his3Δ200, leu2-3,112, ura3-52, lys2-801, ent1ΔACB::kanMX6, sla2-mTq2-F40-mNG::URA3*
MSK444	Ent1 ACB deletion, Sla2 NF HP35	MATα, *his3Δ200, leu2-3,112, ura3-52, lys2-801, ent1ΔACB::kanMX6, sla2-mTq2-HP35-mNG::URA3*
MSK445	Ent1 ACB deletion, Sla2 NF HP35st	MATα, his3Δ200, *leu2-3,112, ura3-52, lys2-801, ent1ΔACB::kanMX6, sla2-mTq2-HP35st-mNG::URA3*
MSK483	Ent1 ACB deletion, Myo5 deletion, Sla2-F40 FS	MATα, *his3Δ200, leu2-3,112, ura3-52, lys2-801, ent1ΔACB::kanMX6, sla2(1-2106)-mTq2-F40-mNG-sla2end::URA3, myo5Δ::hphNT1*
MSK551	Ent1 ACB deletion, Sla2-HP35 FS, Abp1-mScarlet-I	MATα, *his3Δ200, leu2-3,112, ura3-52, lys2-801, ent1ΔACB::kanMX6, sla2(1-2106)-mTq2-HP35-mNG-*

		sla2end::URA3, ABP1-mScarlet-I::hphNT1
MSK553	Bbc1 deletion	MATα, *his3Δ200, leu2-3,112, ura3-52, lys2-801, bbc1Δ::hph1NT1*
MSK554	Fps1 deletion	MATα, *his3Δ200, leu2-3,112, ura3-52, lys2-801, fps1Δ::natNT2*
MSK555	Bbc1 deletion, Fps1 deletion	MATα, *his3Δ200, leu2-3,112, ura3-52, lys2-801, bbc1Δ::hph1NT1, fps1Δ::natNT2*
MSK557	Ent1 ACB deletion, Bbc1 deletion, Sla2-HP35 FS	MATα, *his3Δ200, leu2-3,112, ura3-52, lys2-801, ent1ΔACB::kanMX6, SLA2(1-2106)-mTq2-HP35-mNG-SLA2end::URA3, bbc1Δ::hphNT1*
MSK560	Sla2ΔTHATCH-F40 NF	MATα, *his3Δ200, leu2-3,112, ura3-52, lys2-801, sla2(1-2106)-mTq2-F40-mNG::URA3*
MSK561	Sla2ΔTHATCH-HP35 NF	MATα, *his3Δ200, leu2-3,112, ura3-52, lys2-801, sla2(1-2106)-mTq2-HP35-mNG::URA3*
MSK567	Ent1 ACB deletion, Rvs167 deletion, Sla2-HP35 FS	MATα, *his3Δ200, leu2-3,112, ura3-52, lys2-801, ent1ΔACB::kanMX6, sla2(1-2106)-mTq2-HP35-mNG-sla2end::URA3, rvs167Δ::hphNT1*
MSK575	Ent1 ACB deletion, Fps1 deletion, Sla2-HP35 FS	MATα, *his3Δ200, leu2-3,112, ura3-52, lys2-801, ent1ΔACB::kanMX6, sla2(1-2106)-mTq2-HP35-mNG-sla2end::URA3, fps1Δ::natNT2*
MSK576	Ent1 ACB deletion, Fps1 deletion, Sla2-HP35st FS	MATα, *his3Δ200, leu2-3,112, ura3-52, lys2-801, ent1ΔACB::kanMX6, sla2(1-2106)-mTq2-HP35st-mNG-sla2end::URA3, fps1Δ::natNT2*

Table 9 Plasmids used in this study.

Name	**Description**
pRS416-*SLA2*-2xHA	*SLA2* promoter (384 bp) was PCR amplified from genomic DNA and cloned into *SacI-AscI* sites of pRS416. *SLA2* coding sequence was similarly amplified and cloned using *AscI-XmaI* sites.
pRS416-*SLA2*(2106_2107insACCGGGTCTAGA)-2xHA	*SLA2* coding sequence containing *SgrAI-XbaI* restriction sites after codon for amino acid V702.
pRS416-*SLA2*(2910_2911insTCGTCTAGA)-2xHA	*SLA2* coding sequence containing *XmaI-XbaI* restriction sites between *SLA2* coding sequence and sequence HA tags.
pRS416-*SLA2ΔTHATCH*(2106insACCGGGTCTAGA)-2xHA	*SLA2* coding sequence (1-2106) containing *SgrAI-XbaI* restriction sites after codon for amino acid V702 and missing THATCH domain.
pRS416-*SLA2*(1-702)-mTurquoise2-linker-mNeonGreen-*SLA2*end-2xHA	Sla2 force sensor containing a tension sensor module with F40/HP35/HP35st after amino acid 702.
pRS416-*SLA2*-mTurquoise2-linker-mNeonGreen-2xHA	Sla2 no force control containing a tension sensor module with F40/HP35/HP35st.
pRS416-*SLA2*(1-702)-mTurquoise2-linker-mNeonGreen-2xHA	Sla2 no force control containing a tension sensor module with F40/HP35/HP35st after amino acid 702 and missing THATCH domain.
pFA6a-kanMX6	Cassette for gene deletion using kanMX6 marker.
pFA6a-hphNT1	Cassette for gene deletion using hphNT1 marker.
pFA6a-natNT2	Cassette for gene deletion using natNT2 marker.
pFA6a-mScarlet-I-hphNT1	Cassette for gene tagging with mScarlet-I protein.
pFA6a-mTurquoise2-hphNT1	Cassette for gene tagging with mTurquoise2 protein.
pFA6a-mNeonGreen-kanMX6	Cassette for gene tagging with mNeonGreen protein.

Table 10 Primers used in this study.

Name	Description	Sequence (5'-3')
AA643	Sequencing of Sla2 FS and Sla2 NF sensor constructs from *URA3* locus	ACGTGAATTCGTTTCTAAGGGTGAAGAAGACAAC
mk221	Deletion of *MYO5* (S2 primer)	TATTTGCTCGTATAGAGTATATACTCGCTAAATACATTTTGATTAATCGATGAATTCGAGCTCG
mk270	Deletion of *RVS167* (S2 primer)	TAGAAGGTAATGAATACAGAGGGATGCAGGGGCCTCCTCTAATCGATGAATTCGAGCTCG
mk363	Deletion of *RVS167* (S1 primer)	GTCATTTAACACCAAGAATCAAGGAGCCAATAAGTGCACATGCGTACGCTGCAGGTCGAC
mk365	Deletion of *MYO5* (S1 primer)	AAGAACAGTGGCCAATACGAATTTAACCGCTTTATAGAAATGCGTACGCTGCAGGTCGAC
mk593	Sequencing of *ENT1* after *ACB* domain deletion	ATGGCGCGCCATGCAACAACAGCAAGGC
oms001	Amplification of mTurquoise2	ATAACCCGGGATGGTGAGCAAGGGCG
oms002	Amplification of mTurquoise2 fused with F40 sequence	CGCCGGGACCAGCACCCCCTGGACCCGCGCCACCAGGACCTGCACCGCCCGGACCCGCCCCACCGGGCCCACTAGTCTTGTACAGCTCGTCCATG
oms004	Amplification of mNeonGreen	AATATGCGGCCGCTCTAGACTTGTACAATTCGTCCATACCC
oms012	Amplification of mNeonGreen fused with F40 sequence	ATTATGGCGCCGGGCCTGGTGGGGCCGGCCCAGGTGGTGCCGGTCCAGGTGGTGCAACCGGTATGGTTTCTAAGGGTGAAGAAG
oms040	Deletion of *ENT1 ACB* domain (S2 primer)	ATCTGATTAGAAATGCGGACTGGAATGACAGAATCACTTCAATCGATGAATTCGAGCTCG

oms074	Sequencing of Sla2 FS and Sla2 NF constructs	AACGCGTCGACATGTCTAAAGGC GAAGAATTGTTTAC
oms092	Sequencing of Sla2 NF construct	CCAGGTCGGTGATGAGGAG
oms124	Sequencing of Sla2 FS construct	GTAATACGACTCACTATAGGGC
oms126	Detection of hphNT1, natNT2 and kanMX6 integration	CAAGACTGTCAAGGAGGG
oms127	Detection of hphNT1, natNT2 and kanMX6 integration	GGGACAATTCAACGCGTCTG
oms131	Deletion of *ENT1 ACB* domain (S3 primer)	CGAAGAACTAGCACAGTTTCAAC AACAACAACAACTACAGGAACAA CAGTACTTAATTGATTTATGACG TACGCTGCAGGTCGAC
oms139	Sequencing of Sla2 FS and Sla2 NF constructs	GCAAAACCGTCTCGAGCAAG
oms143	*SLA2 FS*, *SLA2 NF* and *Sla2ΔTHATCH NF* amplification from pRS416 for genome integration (S2 primer annealing into *URA3* locus of pRS416)	CTTCAAATAAATATATTTATATT AACGTTTATCTTTATATATAAAA AGTACAATTCATGATCATGCACC ATACCACAGC
oms144	*SLA2 FS*, *SLA2 NF* and *Sla2ΔTHATCH NF* amplification from pRS416 for genome integration. Sequencing of Sla2 FS and Sla2 NF	CTCCTTTGAGTTGGTCG
oms170	Verification *MYO5* deletion	TGACATTCTACCAAATCGG
oms172	Verification *RVS167* deletion	CATCTGTAGACATACCTCTATCA AG
oms194	*ABP1* tagging with mScarlet-I (S3)	AAAAGGTCTCTTCCCCAGCAATT ATGTGTCTTTGGGCAACCGTACG CTGCAGGTCGAC
oms195	*ABP1* tagging with mScarlet-I (S2)	ACGTAAGAATAATATAATAGCAT GACGCTGACGTGTGATTATCGAT GAATTCGAGCTCG
oms213	Deletion of *BBC1* (S1 primer)	GTCCCAACTGCAAGAGCTACTAG AAGTAAACACAGTCTTACCCAAA

		CTAAGGATGCGTACGCTGCAGGTCGAC
oms214	Deletion of *BBC1* (S2 primer)	AAATGATGAAATCGAAAGCATTCACAATTTCCCCTTGGAAGCATTGGGTAAATTAATCGATGAATTCGAGCTCG
oms215	Verification *BBC1* deletion	GCCCCTATTTTACCTCC
oms218	Detection of F40 peptide linker	CGGTCCAGGTGGTGC
oms219	Detection of HP35 peptide linker	TTTGGAAGCAACAGAATC
oms220	Detection of HP35st peptide linker	GGAAACAGCAAGCGC
oms266	Deletion of *FPS1* (S1 primer)	GGTTGTTCTTCTTTATTATTTTACCAAGTACGCTCGAGGGTACATTCTAATGCATTAAAAGACATGCGTACGCTGCAGGTCGAC
oms267	Deletion of *FPS1* (S2 primer)	CAGTATTTTTTTCTATCAGTCTATATTATTTGTTTCTTTTTCTTGTCTGTTTTCTCAATCGATGAATTCGAGCTCG
oms268	Verification *FPS1* deletion	GGAACAGTGTGAATCCG

Table 11 Media and buffers used in this study.

Name	**Composition**
YPD	1% yeast extract, 2% glucose, 2% bacteriological peptone (+2% agar for solid medium).
SD-Trp	6.7 g/L yeast nitrogen base - low fluorescence without amino acids, folic acid and riboflavin, 740 mg/L CSM, Single Drop-Out - Trp, 2% glucose.
SD-Trp, -Ura	6.7 g/L yeast nitrogen base - low fluorescence without amino acids, folic acid and riboflavin, 720 mg/L CSM, Double Drop-Out - Trp, -Ura, 2% glucose (+2% agar for solid medium).
LB	1% tryptone, 0.5% yeast extract, 0.5% NaCl (+2% agar for solid medium).
Tfb1	30 mM KOAc, 50 mM $MnCl_2$, 100 mM RbCl, 10 mM $CaCl_2$, in 15% glycerol (w/v). pH adjusted to 5.8 with acetic acid.
Tfb2	10 mM Na-MOPS (pH 7.0), 75 mM $CaCl_2$, 10 mM RbCl, in 15% glycerol (w/v). pH adjusted to 7.0 with NaOH.
TAE	0.4 M Tris, acetic acid 0.2 M, 0.01 M EDTA. pH adjusted to 8.3 with NaOH.

Table 12 Chemicals used in this study with respective manufacturer.

Chemical	**Company**
3-(*N*-morpholino)propanesulfonic acid (MOPS)	Roth
Acetic acid	Roth
Agar	Roth
Ampicillin	Applichem
Calcium chloride ($CaCl_2$)	Sigma-Aldrich
CloNat	Formedium
Concanavalin A	Sigma-Aldrich
CSM, Double Drop-Out –Trp, -Ura	Formedium
CSM, Single Drop-Out –Trp	Formedium
D-sorbitol	Roth
D(+)-glucose	Roth
Ethylenediaminetetraaceitc acid (EDTA)	Roth
Ethanol	Applichem
G418	Formedium
Glycerol	Roth
Hygromycin B	Formedium
LB medium powder	Roth
Lithium Acetate (LiAc)	Sigma-Aldrich
Manganese (II) chloride ($MnCl_2$)	Sigma-Aldrich
Polyethylene glycol (PEG 3350)	Sigma-Aldrich
Potassium acetate (KOAc)	Sigma-Aldrich
Rubidium chloride (RbCl)	Roth
Salmon sperm DNA	Sigma-Aldrich
Sodium chloride (NaCl)	Roth
Sodium hydroxide (NaOH)	Sigma-Aldrich
Tris(hydroxymethyl)aminomethane	Roth
Yeast nitrogen base - low fluorescence	Formedium

YPD medium powder	Roth

REFERENCES

Aghamohammadzadeh S, Ayscough KR (2009). Differential requirements for actin during yeast and mammalian endocytosis. Nat Cell Biol. 11(8), 1039-1042.

Akamatsu M, Vasan R, Serwas D, Ferrin MA, Rangamani P, Drubin DG (2020). Principles of self-organization and load adaptation by the actin cytoskeleton during clathrin-mediated endocytosis. eLife. 9:e49840.

Antonny B, Burd C, De Camilli P, Chen E, Daumke O, Faelber K, Ford M, Frolov VA, Frost A, Hinshaw JE, Kirchhausen T, Kozlov MM, Lenz M, Low HH, McMahon H, Merrifield C, Pollard TD, Robinson PJ, Roux A, Schmid S (2016). Membrane fission by dynamin: what we know and what we need to know. EMBO J. 2;35(21), 2270-2284.

Austen K, Ringer P, Mehlich A, Chrostek-Grashoff A, Kluger C, Klingner C, Sabass B, Zent R, Rief M, Grashoff C (2015). Extracellular rigidity sensing by talin isoform-specific mechanical linkages. Nat Cell Biol. 17(12), 1597-1606.

Ayscough KR (2000). Endocytosis and the development of cell polarity in yeast require a dynamic F-actin cytoskeleton. Curr Biol. 10(24), 1587–1590.

Ayscough KR, Stryker J, Pokala N, Sanders M, Crews P, Drubin DG (1997). High rates of actin filament turnover in budding yeast and roles for actin in establishment and maintenance of cell polarity revealed using the actin inhibitor latrunculin-A. J Cell Biol. 137(2), 399–416.

Boulant S, Kural C, Zeeh JC, Ubelmann F, Kirchhausen T (2011). Actin dynamics counteract membrane tension during clathrin-mediated endocytosis (2011). Nat Cell Biol. 13(9), 1124-1131.

Brach T, Godlee C, Moeller-Hansen I, Boeke D, Kaksonen M (2014). The initiation of clathrin-mediated endocytosis is mechanistically highly flexible. Curr Biol. 24(5), 548-554.

Brett TJ, Legendre-Guillemin V, McPherson PS, Fremont DH (2006). Structural definition of the F-actin-binding THATCH domain from Hip1R. Nat Struct Mol Biol. 13(2), 121-130.

Carlsson AE, Bayly PV (2014). Force generation by endocytic actin patches in budding yeast. Biophys J. 106(8), 1596-1606.

Carroll SY, Stimpson HE, Weinberg J, Toret CP, Sun Y, Drubin DG (2012). Analysis of yeast endocytic site formation and maturation through a regulatory transition point. Mol Biol Cell. 23(4), 657-668. Erratum in: Mol Biol Cell. 23(16), 3275.

Collins A, Warrington A, Taylor KA, Svitkina T (2011). Structural organization of the actin cytoskeleton at sites of clathrin-mediated endocytosis. Curr Biol. 21(14), 1167-1175.

Cossart P, Helenius, A (2014). Endocytosis of viruses and bacteria. Cold Spring Harb Perspect Biol. 6:a016972.

Cost AL, Khalaji S, Grashoff C (2019). Genetically Encoded FRET-Based Tension Sensors. Curr Protoc Cell Biol. 83(1):e85.

Dannhauser PN, Ungewickell EJ (2012). Reconstitution of clathrin-coated bud and vesicle formation with minimal components. Nat Cell Biol. 14(6), 634-639.

Daumke O, Roux A, Haucke V (2014). BAR domain scaffolds in dynamin-mediated membrane fission. Cell. 156(5), 882-892.

Dmitrieff S, Nédélec F (2015). Membrane Mechanics of Endocytosis in Cells with Turgor. PLoS Comput Biol. 11(10):e1004538.

Engqvist-Goldstein AE, Warren RA, Kessels MM, Keen JH, Heuser J, Drubin DG (2001). The actin-binding protein Hip1R associates with clathrin during early stages of endocytosis and promotes clathrin assembly in vitro. J Cell Biol. 154(6), 1209-1223.

Freikamp A, Cost AL, Grashoff C (2016). The piconewton force awakens: quantifying mechanics in cells. Trends Cell Biol. 26(11), 838-847.

Freikamp A, Mehlich A, Klingner C, Grashoff C (2017). Investigating piconewton forces in cells by FRET-based molecular force microscopy. J Struct Biol. 197(1), 37-42.

Fricke R, Gohl C, Bogdan S (2010). The F-BAR protein family Actin' on the membrane. Commun Integr Biol. 3(2), 89-94.

Geli MI, Riezman H (1996). Role of type I myosins in receptor-mediated endocytosis in yeast. Science. 272(5261), 533-535.

Goode BL, Eskin JA, Wendland B (2015). Actin and endocytosis in budding yeast. Genetics. 199(2), 315-358.

Grashoff C, Hoffman BD, Brenner MD, Zhou R, Parsons M, Yang MT, McLean MA, Sligar SG, Chen CS, Ha T, Schwartz MA (2010). Measuring mechanical tension across vinculin reveals regulation of focal adhesion dynamics. Nature. 466(7303), 263-266.

Hassinger JE, Oster G, Drubin DG, Rangamani P (2017). Design principles for robust vesiculation in clathrin-mediated endocytosis. Proc Natl Acad Sci U S A. 114(7), E1118-E1127.

Hohmann S (2002). Osmotic stress signaling and osmoadaptation in yeasts. Microbiol Mol Biol Rev. 66(2), 300-372.

Idrissi FZ, Blasco A, Espinal A, Geli MI (2012). Ultrastructural dynamics of proteins involved in endocytic budding. Proc Natl Acad Sci U S A. 109(39), E2587-2594.

Idrissi FZ, Grötsch H, Fernández-Golbano IM, Presciatto-Baschong C, Riezman H, Geli MI (2008). Distinct acto/myosin-I structures associate with endocytic profiles at the plasma membrane. J Cell Biol. 180(6), 1219-1232.

Ishikawa-Ankerhold HC, Ankerhold R, Drummen GP (2012). Advanced fluorescence microscopy techniques-FRAP, FLIP, FLAP, FRET and FLIM. Molecules. 17(4), 4047-4132.

Janke C, Magiera MM, Rathfelder N, Taxis C, Reber S, Maekawa H, Moreno-Borchart A, Doenges G, Schwob E, Schiebel E, Knop M (2004). A versatile toolbox for PCR-based tagging of yeast genes: new fluorescent proteins, more markers and promoter substitution cassettes. Yeast. 21(11), 947-962.

Kaksonen M, Sun Y, Drubin DG (2003). A pathway for association of receptors, adaptors, and actin during endocytic internalization. Cell. 115(4), 475-487.

Kaksonen M, Toret CP, Drubin DG (2005). A modular design for the clathrin- and actin-mediated endocytosis machinery. Cell. 123(2), 305-320.

Kaksonen M, Toret CP, Drubin DG (2006). Harnessing actin dynamics for clathrin-mediated endocytosis. Nat Rev Mol Cell Biol. 7(6), 404-414.

Kishimoto T, Sun Y, Buser C, Liu J, Michelot A, Drubin DG (2011). Determinants of endocytic membrane geometry, stability, and scission. Proc Natl Acad Sci U S A. 108(44), E979-988.

Kübler E, Riezman H (1993). Actin and fimbrin are required for the internalization step of endocytosis in yeast. EMBO J. 12(7), 2855–2862.

Kukulski W, Schorb M, Kaksonen M, Briggs J (2012). Plasma membrane reshaping during endocytosis is revealed by time-resolved electron tomography. Cell. 150(3), 508–520.

Lamaze C, Fujimoto LM, Yin HL, Schmid SL (1997). The actin cytoskeleton is required for receptor-mediated endocytosis in mammalian cells. J Biol Chem. 272(33), 20332-20335.

Lewellyn EB, Pedersen RT, Hong J, Lu R, Morrison HM, Drubin DG (2015). An Engineered Minimal WASP-Myosin Fusion Protein Reveals Essential Functions for Endocytosis. Dev Cell. 35(3), 281-294.

Maldonado-Báez L, Dores MR, Perkins EM, Drivas TG, Hicke L, Wendland B (2008). Interaction between Epsin/Yap180 adaptors and the scaffolds Ede1/Pan1 is required for endocytosis. Mol Biol Cell. 19(7), 2936-2948.

Manenschijn HE, Picco A, Mund M, Ries J, Kaksonen M (2019). Type-I myosins promote actin polymerization to drive membrane bending in endocytosis. eLife. 8:e44215.

Mastop M, Bindels DS, Shaner NC, Postma M, Gadella TWJ Jr, Goedhart J (2017). Characterization of a spectrally diverse set of fluorescent proteins as FRET acceptors for mTurquoise2. Sci Rep. 7(1), 11999.

McMahon HT, Boucrot E (2011). Molecular mechanism and physiological functions of clathrin-mediated endocytosis. Nat Rev Cell Biol. 12(8), 517-533.

Merrifield CJ, Feldman ME, Wan L, Almers W (2002). Imaging actin and dynamin recruitment during invagination of single clathrin-coated pits. Nat Cell Biol. 4(9), 691-698.

Messa M, Fernández-Busnadiego R, Sun EW, Chen H, Czapla H, Wrasman K, Wu Y, Ko G, Ross T, Wendland B, De Camilli P (2014). Epsin deficiency impairs endocytosis by stalling the actin-dependent invagination of endocytic clathrin-coated pits. eLife. 3:e03311.

Mim C, Cui H, Gawronski-Salerno JA, Frost A, Lyman E, Voth GA, Unger VM (2012). Structural basis of membrane bending by the N-BAR protein endophilin. Cell. 149(1), 137-145.

Mochida J, Yamamoto T, Fujimura-Kamada K, Tanaka K. The novel adaptor protein (2002), Mti1p, and Vrp1p, a homolog of Wiskott-Aldrich syndrome protein-interacting protein (WIP), may antagonistically regulate type I myosins in Saccharomyces cerevisiae. Genetics. 160(3), 923-934.

Mooren OL, Galletta BJ, Cooper JA (2012). Roles for actin assembly in endocytosis. Annu Rev Biochem. 81, 661-686.

Mullins RD, Heuser JA, Pollard TD (1998). The interaction of Arp2/3 complex with actin: nucleation, high affinity pointed end capping, and formation of branching networks of filaments. Proc Natl Acad U S A. 95(11), 6181-6186.

Mund M, van der Beek JA, Deschamps J, Dmitrieff S, Hoess P, Monster JL, Picco A, Nédélec F, Kaksonen M, Ries J (2018). Systematic nanoscale analysis of endocytosis links efficient vesicle formation to patterned actin nucleation. Cell. 174(4), 884-896.

Nickaeen M, Berro J, Pollard TD, Slepchenko BM (2019). Actin assembly produces sufficient forces for endocytosis in yeast. Mol Biol Cell. 30(16), 2014-2024.

Picco A, Kukulski W, Manenschijn HE, Specht T, Briggs JAG, Kaksonen M (2018). The contributions of the actin machinery to endocytic membrane bending and vesicle formation. Mol Biol Cell. 29(11), 1346-1358.

Picco A, Mund M, Ries J, Nédélec F, Kaksonen M (2015). Visualizing the functional architecture of the endocytic machinery. eLife. 4: e04535.

Qualmann B, Kessels MM, Kelly RB (2000). Molecular links between endocytosis and the actin cytoskeleton. J Cell Biol. 150(5), F111–F116.

Riggi M, Bourgoint C, Macchione M, Matile S, Loewith R, Roux A (2019). TORC2 controls endocytosis through plasma membrane tension. J Cell Biol. 218(7), 2265-2276.

Riggi M, Niewola-Staszkowska K, Chiaruttini N, Colom A, Kusmider B, Mercier V, Soleimanpour S, Stahl M, Matile S, Roux A, Loewith R (2018). Decrease in plasma membrane tension triggers PtdIns(4,5)P_2 phase separation to inactivate TORC2. Nat Cell Biol. 20(9), 1043-1051.

Ringer P, Weißl A, Cost A, Freikamp A, Sabass B, Mehlich A, Tramier M, Rief M, Grashoff C (2017). Multiplexing molecular tension sensors reveals piconewton force gradient across talin-1. Nat Methods. 14(11), 1090-1096.

Rodal AA, Manning AL, Goode BL, Drubin DG (2003). Negative regulation of yeast WASp by two SH3 domain-containing proteins. Curr Biol. 13(12), 1000-1008.

Schaber J, Adrover MA, Eriksson E, Pelet S, Petelenz-Kurdziel E, Klein D, Posas F, Goksör M, Peter M, Hohmann S, Klipp E (2010). Biophysical properties of Saccharomyces cerevisiae and their relationship with HOG pathway activation. Eur Biophys J. 39(11), 1547-1556.

Scher-Zagier JK, Carlsson AE (2016). Local Turgor Pressure Reduction via Channel Clustering. Biophys J. 111(12), 2747-2756.

Shupliakov O, Bloom O, Gustafsson JS, Kjaerulff O, Low P, Tomilin N, Pieribone VA, Greengard P, Brodin L (2002). Impaired recycling of synaptic vesicles after acute perturbation of the presynaptic actin cytoskeleton. Proc Natl Acad Sci U S A. 99(22), 14476–14481.

Sikorski RS, Hieter P (1989). A system of shuttle vectors and yeast host strains designed for efficient manipulation of DNA in Saccharomyces cerevisiae. Genetics. 122(1), 19-27.

Skruzny M, Brach T, Ciuffa R, Rybina S, Wachsmuth M, Kaksonen M (2012). Molecular basis for coupling the plasma membrane to the actin cytoskeleton during clathrin-mediated endocytosis. Proc Natl Acad Sci U S A. 109(38), E2533-E2542.

Skruzny M, Desfosses A, Prinz S, Dodonova SO, Gieras A, Uetrecht C, Jakobi AJ, Abella M, Hagen WJ, Schulz J, Meijers R, Rybin V, Briggs JA, Sachse C, Kaksonen M (2015. An

organized co-assembly of clathrin adaptors is essential for endocytosis. Dev Cell. 33(2), 150-162.

Skruzny M, Pohl E, Abella M (2019). FRET microscopy in yeast. Biosensors (Basel). 9(4), 122.

Souza CM, Pichler H. Lipid requirements for endocytosis in yeast (2006). Biochim Biophys Acta. 1771(3), 442-454.

Stimpson HE, Toret CP, Cheng AT, Pauly BS, Drubin DG (2009). Early-arriving Syp1p and Ede1p function in endocytic site placement and formation in budding yeast. Mol Biol Cell. 20(22), 4640-4651.

Stryer L (1978). Fluorescence energy transfer as a spectroscopic ruler. Annu Rev Biochem. 47, 819-846.

Sun Y, Drubin DG (2012). The functions of anionic phospholipids during clathrin-mediated endocytosis site initiation and vesicle formation. J Cell Sci. 125(Pt 24), 6157-6165.

Sun Y, Martin AC, Drubin DG (2006). Endocytic internalization in budding yeast requires coordinated actin nucleation and myosin motor activity. Dev Cell. 11(1), 33-46.

Sun Y, Schöneberg J, Chen X, Jiang T, Kaplan C, Xu K, Pollard TD, Drubin DG (2019). Direct comparison of clathrin-mediated endocytosis in budding and fission yeast reveals conserved and evolvable features. eLife. 8:e50749.

Tamás MJ, Luyten K, Sutherland FC, Hernandez A, Albertyn J, Valadi H, Li H, Prior BA, Kilian SG, Ramos J, Gustafsson L, Thevelein JM, Hohmann S (1999). Fps1p controls the accumulation and release of the compatible solute glycerol in yeast osmoregulation. Mol Microbiol. 31(4), 1087-1104.

Teunissen AJP, Pérez-Medina C, Meijerink A, Mulder WJM (2018). Investigating supramolecular systems using Förster resonance energy transfer. Chem Soc Rev. 47(18), 7027-7044.

Tinevez JY, Perry N, Schindelin J, Hoopes GM, Reynolds GD, Laplantine E, Bednarek SY, Shorte SL, Eliceiri KW (2016). TrackMate: An open and extensible platform for single-particle tracking. Methods. 115, 80-90.

Walani N, Torres J, Agrawal A (2015) Endocytic proteins drive vesicle growth via instability in high membrane tension environment. Proc Natl Acad Sci U S A 112(12), E1423–E1432.

Wang X, Carlsson AE (2017). A master equation approach to actin polymerization applied to endocytosis in yeast. PLoS Comput Biol. 13(12):e1005901.

Yang S, Cope MJ, Drubin DG (1999). Sla2p is associated with the yeast cortical actin cytoskeleton via redundant localization signals. Mol Biol Cell. 10(7), 2265-2283.

Youn JY, Friesen H, Kishimoto T, Henne WM, Kurat CF, Ye W, Ceccarelli DF, Sicheri F, Kohlwein SD, McMahon HT, Andrews BJ (2010). Dissecting BAR domain function in the yeast Amphiphysins Rvs161 and Rvs167 during endocytosis. Mol Biol Cell. 21(17), 3054-3069.

Zhang T, Sknepnek R, Bowick MJ, Schwarz JM (2015). On the modeling of endocytosis in yeast. Biophys J. 108(3), 508-519.

SUPPLEMENTARY MATERIAL

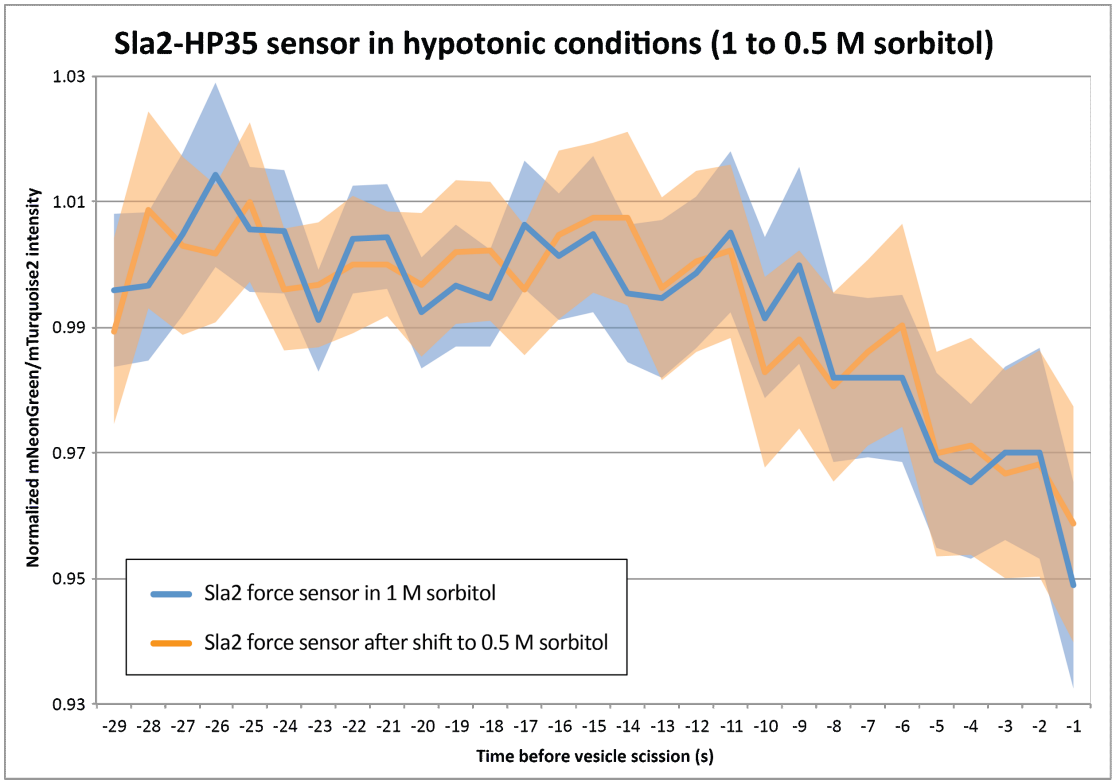

Figure S1 FRET ratio signal of Sla2-HP35 force sensor in cells incubated in 1 M sorbitol medium (blue) and after indicated osmotic shift (orange) before vesicle scission (time 0 s). Average ± 95% confidence intervals of Sla2-HP35 force sensor in cells incubated on 1 M sorbitol (n=81), Sla2-HP35 force sensor after 1 to 0.5 M shift (n=62) are shown. Complete data provided in Supplementary Table S14.

Table S1 FRET ratio data obtained from Sla2-F40 FS and Sla2 NF F40. Normalized FRET ratio (Norm FRET ratio in table) was calculated as described in Ratiometric FRET (Materials and methods). Time before vesicle scission (in seconds, Time in table), standard deviation (SD), sample size (n) and 95% confidence interval (CI 95%) are shown. P-value was calculated using two-tailed Welch's t-test.

	Sla2-F40 FS				Sla2 NF F40				
Time	Norm FRET ratio	SD	n	CI 95%	Norm FRET ratio	SD	n	CI 95%	p-value
-35	0.987	0.051	31	0.019	0.983	0.036	15	0.020	0.75725
-34	0.996	0.050	36	0.017	0.989	0.036	20	0.017	0.52999
-33	0.989	0.046	42	0.014	0.998	0.033	23	0.014	0.39440
-32	0.993	0.051	46	0.015	0.992	0.030	23	0.013	0.94534
-31	1.006	0.042	51	0.012	0.990	0.033	30	0.012	0.06068
-30	0.999	0.046	56	0.012	0.986	0.026	33	0.009	0.09467
-29	1.002	0.047	63	0.012	0.991	0.028	36	0.010	0.12442
-28	1.000	0.050	69	0.012	0.994	0.022	38	0.007	0.40358
-27	1.007	0.045	72	0.011	0.996	0.027	38	0.009	0.13434
-26	1.000	0.037	80	0.008	0.991	0.025	43	0.008	0.09899
-25	1.000	0.032	84	0.007	0.997	0.020	46	0.006	0.64132
-24	1.002	0.028	85	0.006	0.997	0.016	51	0.005	0.18250
-23	0.997	0.026	86	0.005	0.998	0.015	53	0.004	0.76170
-22	0.999	0.023	87	0.005	1.001	0.017	54	0.005	0.57488
-21	1.000	0.021	90	0.004	1.000	0.014	56	0.004	0.91748
-20	0.995	0.022	91	0.005	1.002	0.014	58	0.004	0.03156
-19	1.002	0.023	92	0.005	0.999	0.012	58	0.003	0.27876
-18	1.001	0.026	92	0.005	1.002	0.018	58	0.005	0.76357
-17	1.004	0.026	92	0.005	1.003	0.018	58	0.005	0.89031
-16	0.999	0.031	92	0.006	1.002	0.023	58	0.006	0.42748
-15	0.995	0.039	92	0.008	1.005	0.025	58	0.007	0.06157
-14	0.996	0.039	92	0.008	1.002	0.026	58	0.007	0.30117
-13	0.993	0.040	92	0.008	0.998	0.027	58	0.007	0.43809
-12	0.998	0.040	92	0.008	1.000	0.028	58	0.007	0.64383
-11	0.987	0.039	92	0.008	1.002	0.034	58	0.009	0.01740
-10	0.984	0.042	92	0.009	1.004	0.034	58	0.009	0.00214
-9	0.982	0.045	92	0.009	0.998	0.032	58	0.009	0.01536
-8	0.983	0.046	92	0.009	0.998	0.031	58	0.008	0.01978
-7	0.975	0.047	92	0.010	0.995	0.035	58	0.009	0.00375
-6	0.974	0.044	92	0.009	0.992	0.038	58	0.010	0.00842
-5	0.967	0.048	92	0.010	0.996	0.035	58	0.009	0.00004
-4	0.967	0.051	92	0.011	0.996	0.043	58	0.011	0.00023
-3	0.966	0.048	92	0.010	0.990	0.041	58	0.011	0.00145
-2	0.959	0.050	92	0.010	0.990	0.039	58	0.010	2.81E-05
-1	0.956	0.050	92	0.010	0.993	0.044	58	0.012	5.45E-06

Table S2 FRET ratio data obtained from Sla2-HP35 FS and Sla2 NF HP35. Normalized FRET ratio (Norm FRET ratio in table) was calculated as described in Ratiometric FRET (Materials and methods). Time before vesicle scission (in seconds, Time in table), standard deviation (SD), sample size (n) and 95% confidence interval (CI 95%) are shown. P-value was calculated using two-tailed Welch's t-test.

	Sla2-HP35 FS				Sla2 NF HP35				
Time	Norm FRET ratio	SD	n	CI 95%	Norm FRET ratio	SD	n	CI 95%	p-value
-35	0.987	0.053	24	0.023	0.986	0.014	3	0.035	0.9394
-34	0.994	0.055	29	0.021	0.980	0.031	9	0.024	0.3264
-33	1.003	0.043	41	0.013	0.993	0.031	16	0.016	0.3120
-32	0.998	0.041	46	0.012	0.996	0.036	19	0.017	0.8986
-31	0.999	0.043	52	0.012	1.001	0.034	25	0.014	0.8530
-30	0.998	0.046	56	0.012	1.003	0.032	32	0.012	0.5609
-29	1.000	0.039	63	0.010	0.996	0.035	40	0.011	0.5810
-28	1.004	0.034	70	0.008	0.992	0.025	47	0.007	0.0318
-27	1.004	0.029	75	0.007	0.995	0.025	51	0.007	0.0708
-26	1.004	0.029	78	0.006	0.997	0.020	58	0.005	0.1013
-25	0.998	0.030	82	0.007	0.998	0.017	60	0.004	0.9548
-24	1.000	0.026	92	0.005	0.997	0.018	63	0.004	0.5310
-23	0.999	0.022	98	0.004	0.999	0.015	68	0.004	0.9191
-22	0.997	0.020	102	0.004	1.001	0.014	71	0.003	0.1110
-21	0.999	0.017	106	0.003	0.998	0.018	81	0.004	0.7805
-20	1.000	0.023	108	0.004	1.001	0.012	82	0.003	0.7384
-19	1.002	0.026	108	0.005	1.003	0.016	82	0.003	0.8473
-18	1.003	0.025	108	0.005	1.000	0.015	82	0.003	0.2263
-17	1.000	0.027	108	0.005	1.001	0.016	82	0.004	0.7740
-16	1.003	0.034	108	0.006	1.001	0.018	82	0.004	0.5617
-15	0.999	0.036	108	0.007	1.001	0.023	82	0.005	0.7175
-14	0.999	0.033	108	0.006	1.001	0.024	82	0.005	0.6885
-13	0.993	0.039	108	0.007	0.999	0.023	82	0.005	0.2298
-12	0.990	0.041	108	0.008	0.998	0.024	82	0.005	0.0868
-11	0.989	0.045	108	0.009	0.998	0.026	82	0.006	0.0949
-10	0.983	0.047	108	0.009	1.000	0.027	82	0.006	0.0022
-9	0.974	0.045	108	0.009	0.996	0.031	82	0.007	5.13E-05
-8	0.973	0.049	108	0.009	0.998	0.029	82	0.006	1.56E-05
-7	0.968	0.044	108	0.008	0.994	0.032	82	0.007	3.37E-06
-6	0.968	0.050	108	0.010	0.991	0.032	82	0.007	0.0002
-5	0.964	0.051	108	0.010	0.988	0.033	82	0.007	0.0001
-4	0.962	0.053	108	0.010	0.993	0.033	82	0.007	1.27E-06
-3	0.952	0.049	108	0.009	0.992	0.034	82	0.007	4.28E-10
-2	0.950	0.051	108	0.010	0.988	0.035	82	0.008	8.17E-09
-1	0.944	0.055	108	0.011	0.984	0.038	82	0.008	1.83E-08

Table S3 FRET ratio data obtained from Sla2-HP35st FS and Sla2 NF HP35st. Normalized FRET ratio (Norm FRET ratio in table) was calculated as described in Ratiometric FRET (Materials and methods). Time before vesicle scission (in seconds, Time in table), standard deviation (SD), sample size (n) and 95% confidence interval (CI 95%) are shown. P-value was calculated using two-tailed Welch's t-test.

	Sla2-HP35st FS				Sla2 NF HP35st				
Time	Norm FRET ratio	SD	n	CI 95%	Norm FRET ratio	SD	n	CI 95%	p-value
-35	0.989	0.064	34	0.022	1.006	0.037	21	0.017	0.21204
-34	0.987	0.059	41	0.019	1.011	0.033	27	0.013	0.04049
-33	0.995	0.056	46	0.017	1.007	0.033	28	0.013	0.22977
-32	0.994	0.051	55	0.014	1.004	0.035	30	0.013	0.26270
-31	1.003	0.059	58	0.015	0.999	0.032	34	0.011	0.61709
-30	1.005	0.055	62	0.014	0.998	0.029	43	0.009	0.43872
-29	0.995	0.057	66	0.014	0.998	0.032	46	0.010	0.76726
-28	1.000	0.053	69	0.013	1.004	0.029	46	0.009	0.64988
-27	1.003	0.044	72	0.010	1.003	0.022	47	0.006	0.97014
-26	1.002	0.041	75	0.009	1.003	0.021	50	0.006	0.89726
-25	0.999	0.034	79	0.008	1.003	0.019	51	0.005	0.33103
-24	1.002	0.031	83	0.007	1.002	0.018	53	0.005	0.97296
-23	1.001	0.027	86	0.006	1.001	0.017	57	0.004	0.82370
-22	1.000	0.029	88	0.006	0.999	0.014	58	0.004	0.72333
-21	0.998	0.027	90	0.006	0.998	0.012	60	0.003	0.98313
-20	0.999	0.026	93	0.005	0.999	0.016	61	0.004	0.87871
-19	1.000	0.025	93	0.005	1.001	0.017	61	0.004	0.83868
-18	0.998	0.027	93	0.006	0.998	0.017	61	0.004	0.93800
-17	1.002	0.030	93	0.006	0.999	0.020	61	0.005	0.34986
-16	1.000	0.035	93	0.007	0.998	0.023	61	0.006	0.63013
-15	0.998	0.037	93	0.008	0.998	0.025	61	0.006	0.98186
-14	0.997	0.046	93	0.009	1.001	0.026	61	0.007	0.45394
-13	0.995	0.045	93	0.009	0.999	0.025	61	0.006	0.47173
-12	0.998	0.050	93	0.010	1.001	0.028	61	0.007	0.55819
-11	0.989	0.053	93	0.011	1.001	0.027	61	0.007	0.07146
-10	0.989	0.058	93	0.012	0.997	0.026	61	0.007	0.24817
-9	0.988	0.055	93	0.011	0.996	0.026	61	0.007	0.23349
-8	0.986	0.063	93	0.013	0.997	0.029	61	0.008	0.14719
-7	0.983	0.055	93	0.011	0.994	0.029	61	0.008	0.11782
-6	0.983	0.063	93	0.013	0.993	0.032	61	0.008	0.23211
-5	0.978	0.057	93	0.012	0.988	0.034	61	0.009	0.18912
-4	0.975	0.058	93	0.012	0.989	0.034	61	0.009	0.06239
-3	0.974	0.064	93	0.013	0.993	0.036	61	0.009	0.01756
-2	0.966	0.062	93	0.013	0.993	0.037	61	0.010	0.00090
-1	0.955	0.057	93	0.012	0.989	0.039	61	0.010	0.00003

Table S4 FRET ratio data obtained from Sla2-HP35 FS and Sla2-HP35st FS. Normalized FRET ratio (Norm FRET ratio in table) was calculated as described in Ratiometric FRET (Materials and methods). Time before vesicle scission (in seconds, Time in table), standard deviation (SD), sample size (n) and 95% confidence interval (CI 95%) are shown. P-value was calculated using two-tailed Welch's t-test.

	Sla2-HP35 FS				Sla2-HP35st FS				
Time	Norm FRET ratio	SD	n	CI 95%	Norm FRET ratio	SD	n	CI 95%	p-value
-35	0.987	0.053	24	0.023	0.989	0.064	34	0.022	0.9319
-34	0.994	0.055	29	0.021	0.987	0.059	41	0.019	0.6215
-33	1.003	0.043	41	0.013	0.995	0.056	46	0.017	0.4336
-32	0.998	0.041	46	0.012	0.994	0.051	55	0.014	0.6791
-31	0.999	0.043	52	0.012	1.003	0.059	58	0.015	0.6389
-30	0.998	0.046	56	0.012	1.005	0.055	62	0.014	0.4550
-29	1.000	0.039	63	0.010	0.995	0.057	66	0.014	0.5848
-28	1.004	0.034	70	0.008	1.000	0.053	69	0.013	0.5971
-27	1.004	0.029	75	0.007	1.003	0.044	72	0.010	0.9672
-26	1.004	0.029	78	0.006	1.002	0.041	75	0.009	0.7799
-25	0.998	0.030	82	0.007	0.999	0.034	79	0.008	0.9739
-24	1.000	0.026	92	0.005	1.002	0.031	83	0.007	0.5800
-23	0.999	0.022	98	0.004	1.001	0.027	86	0.006	0.6514
-22	0.997	0.020	102	0.004	1.000	0.029	88	0.006	0.3707
-21	0.999	0.017	106	0.003	0.998	0.027	90	0.006	0.7993
-20	1.000	0.023	108	0.004	0.999	0.026	93	0.005	0.7393
-19	1.002	0.026	108	0.005	1.000	0.025	93	0.005	0.6332
-18	1.003	0.025	108	0.005	0.998	0.027	93	0.006	0.1777
-17	1.000	0.027	108	0.005	1.002	0.030	93	0.006	0.6365
-16	1.003	0.034	108	0.006	1.000	0.035	93	0.007	0.6195
-15	0.999	0.036	108	0.007	0.998	0.037	93	0.008	0.8984
-14	0.999	0.033	108	0.006	0.997	0.046	93	0.009	0.7103
-13	0.993	0.039	108	0.007	0.995	0.045	93	0.009	0.7415
-12	0.990	0.041	108	0.008	0.998	0.050	93	0.010	0.2446
-11	0.989	0.045	108	0.009	0.989	0.053	93	0.011	0.9855
-10	0.983	0.047	108	0.009	0.989	0.058	93	0.012	0.3693
-9	0.974	0.045	108	0.009	0.988	0.055	93	0.011	0.0467
-8	0.973	0.049	108	0.009	0.986	0.063	93	0.013	0.1159
-7	0.968	0.044	108	0.008	0.983	0.055	93	0.011	0.0319
-6	0.968	0.050	108	0.010	0.983	0.063	93	0.013	0.0630
-5	0.964	0.051	108	0.010	0.978	0.057	93	0.012	0.0773
-4	0.962	0.053	108	0.010	0.975	0.058	93	0.012	0.0823
-3	0.952	0.049	108	0.009	0.974	0.064	93	0.013	0.0096
-2	0.950	0.051	108	0.010	0.966	0.062	93	0.013	0.0452
-1	0.944	0.055	108	0.011	0.955	0.057	93	0.012	0.1408

Table S5 FRET ratio data obtained from Sla2ΔTHATCH-F40 and Sla2ΔTHATCH-HP35. Normalized FRET ratio (Norm FRET ratio in table) was calculated as described in Ratiometric FRET (Materials and methods). Time before vesicle scission (in seconds, Time in table), standard deviation (SD), sample size (n) and 95% confidence interval (CI 95%) are shown.

	Sla2ΔTHATCH-F40				Sla2ΔTHATCH-HP35			
Time	Norm FRET ratio	SD	n	CI 95%	Norm FRET ratio	SD	n	CI 95%
-35	0.987	0.027	12	0.017	1.003	0.034	17	0.018
-34	0.995	0.026	15	0.015	1.000	0.037	20	0.017
-33	0.994	0.027	15	0.015	1.001	0.031	20	0.014
-32	0.992	0.023	15	0.013	1.001	0.035	20	0.016
-31	0.996	0.024	15	0.013	1.003	0.028	20	0.013
-30	0.991	0.026	17	0.013	0.999	0.028	23	0.012
-29	0.986	0.025	18	0.012	1.003	0.034	25	0.014
-28	0.981	0.025	20	0.012	1.003	0.031	25	0.013
-27	0.990	0.026	20	0.012	1.002	0.024	26	0.010
-26	0.994	0.023	21	0.010	0.998	0.026	28	0.010
-25	0.995	0.017	22	0.008	0.992	0.018	28	0.007
-24	0.996	0.018	24	0.008	0.999	0.016	29	0.006
-23	0.992	0.009	25	0.004	0.998	0.014	30	0.005
-22	1.000	0.015	25	0.006	1.001	0.018	30	0.007
-21	0.997	0.012	25	0.005	1.003	0.021	31	0.008
-20	1.003	0.014	26	0.006	1.001	0.014	31	0.005
-19	1.007	0.020	26	0.008	1.000	0.020	31	0.007
-18	1.005	0.014	26	0.006	1.004	0.018	31	0.007
-17	1.003	0.018	26	0.007	1.001	0.023	31	0.008
-16	1.007	0.021	26	0.009	0.998	0.023	31	0.008
-15	1.011	0.025	26	0.010	0.998	0.024	31	0.009
-14	1.006	0.020	26	0.008	0.999	0.025	31	0.009
-13	1.005	0.021	26	0.009	1.000	0.029	31	0.010
-12	1.011	0.025	26	0.010	1.003	0.028	31	0.010
-11	1.007	0.023	26	0.009	1.005	0.020	31	0.007
-10	1.009	0.024	26	0.010	1.008	0.027	31	0.010
-9	1.007	0.030	26	0.012	1.003	0.022	31	0.008
-8	1.007	0.033	26	0.013	1.011	0.024	31	0.009
-7	1.012	0.033	26	0.013	1.009	0.030	31	0.011
-6	1.013	0.035	26	0.014	1.006	0.037	31	0.014
-5	1.015	0.038	26	0.015	1.009	0.037	31	0.013
-4	1.014	0.039	26	0.016	1.003	0.042	31	0.015
-3	1.015	0.032	26	0.013	1.007	0.041	31	0.015
-2	1.008	0.032	26	0.013	1.008	0.041	31	0.015
-1	1.009	0.042	26	0.017	1.014	0.046	31	0.017

Table S6 FRET ratio data obtained from Sla2-F40 FS in wild-type strain and Sla2-F40 FS in Myo5 deletion strain. Normalized FRET ratio (Norm FRET ratio in table) was calculated as described in Ratiometric FRET (Materials and methods). Time before vesicle scission (in seconds, Time in table), standard deviation (SD), sample size (n) and 95% confidence interval (CI 95%) are shown. P-value was calculated using two-tailed Welch's t-test.

	Sla2-F40 FS				Sla2-F40 FS in Myo5 deletion				
Time	Norm FRET ratio	SD	n	CI 95%	Norm FRET ratio	SD	n	CI 95%	p-value
-35	0.987	0.051	31	0.019	1.000	0.053	19	0.026	0.3806
-34	0.996	0.050	36	0.017	1.004	0.055	24	0.023	0.5876
-33	0.989	0.046	42	0.014	1.008	0.044	27	0.017	0.0997
-32	0.993	0.051	46	0.015	1.005	0.047	30	0.018	0.2926
-31	1.006	0.042	51	0.012	0.994	0.047	32	0.017	0.2513
-30	0.999	0.046	56	0.012	0.997	0.040	35	0.014	0.8561
-29	1.002	0.047	63	0.012	0.998	0.047	38	0.015	0.6429
-28	1.000	0.050	69	0.012	1.000	0.038	43	0.012	0.9607
-27	1.007	0.045	72	0.011	1.000	0.036	47	0.010	0.3941
-26	1.000	0.037	80	0.008	0.996	0.034	53	0.009	0.5193
-25	1.000	0.032	84	0.007	1.002	0.031	55	0.008	0.6032
-24	1.002	0.028	85	0.006	1.002	0.032	57	0.009	0.9517
-23	0.997	0.026	86	0.005	1.001	0.024	57	0.006	0.3106
-22	0.999	0.023	87	0.005	0.997	0.018	58	0.005	0.6885
-21	1.000	0.021	90	0.004	0.998	0.019	63	0.005	0.5460
-20	0.995	0.022	91	0.005	1.003	0.025	64	0.006	0.0588
-19	1.002	0.023	92	0.005	1.003	0.021	66	0.005	0.7431
-18	1.001	0.026	92	0.005	0.997	0.024	66	0.006	0.3311
-17	1.004	0.026	92	0.005	0.996	0.024	67	0.006	0.0506
-16	0.999	0.031	92	0.006	0.994	0.029	67	0.007	0.3789
-15	0.995	0.039	92	0.008	0.994	0.036	67	0.009	0.8426
-14	0.997	0.039	92	0.008	0.988	0.038	67	0.009	0.1724
-13	0.993	0.040	92	0.008	0.985	0.040	67	0.010	0.2152
-12	0.998	0.040	92	0.008	0.983	0.048	67	0.012	0.0383
-11	0.987	0.039	92	0.008	0.985	0.050	67	0.012	0.7564
-10	0.984	0.042	92	0.009	0.980	0.050	67	0.012	0.5506
-9	0.983	0.045	92	0.009	0.977	0.056	67	0.014	0.4807
-8	0.983	0.046	92	0.009	0.974	0.058	67	0.014	0.2972
-7	0.975	0.047	92	0.010	0.970	0.061	67	0.015	0.5524
-6	0.974	0.044	92	0.009	0.970	0.066	67	0.016	0.6500
-5	0.967	0.048	92	0.010	0.963	0.067	67	0.016	0.6697
-4	0.967	0.051	92	0.011	0.958	0.067	67	0.016	0.3976
-3	0.966	0.048	92	0.010	0.952	0.062	67	0.015	0.1147
-2	0.959	0.050	92	0.010	0.953	0.068	67	0.017	0.5798
-1	0.956	0.050	92	0.010	0.942	0.067	67	0.016	0.1550

Table S7 FRET ratio data obtained from Sla2-HP35 FS in Rvs167 deletion strain. Normalized FRET ratio (Norm FRET ratio in table) was calculated as described in Ratiometric FRET (Materials and methods). Time before vesicle scission (in seconds, Time in table), standard deviation (SD), sample size (n) and 95% confidence interval (CI 95%) are shown.

	Sla2-HP35 FS in Rvs167 deletion								
Time	Norm FRET ratio	SD	n	CI 95%	Time	Norm FRET ratio	SD	n	CI 95%
-35	1.014	0.044	35	0.0153	0	0.969	0.057	59	0.0150
-34	1.007	0.040	37	0.0133	1	0.967	0.055	59	0.0142
-33	1.000	0.039	38	0.0128	2	0.967	0.059	59	0.0154
-32	1.000	0.035	39	0.0113	3	0.966	0.059	59	0.0153
-31	1.004	0.035	41	0.0111	4	0.965	0.059	59	0.0155
-30	1.008	0.043	43	0.0133	5	0.961	0.060	58	0.0158
-29	1.006	0.036	44	0.0110	6	0.961	0.060	57	0.0160
-28	1.009	0.037	48	0.0106	7	0.955	0.062	55	0.0167
-27	1.008	0.042	52	0.0116	8	0.957	0.067	51	0.0189
-26	1.009	0.035	52	0.0099					
-25	1.001	0.030	53	0.0084					
-24	1.007	0.024	56	0.0065					
-23	1.001	0.022	58	0.0058					
-22	0.999	0.019	59	0.0049					
-21	0.997	0.020	59	0.0053					
-20	0.999	0.026	59	0.0069					
-19	1.004	0.026	59	0.0067					
-18	0.997	0.029	59	0.0075					
-17	0.994	0.031	59	0.0081					
-16	0.987	0.035	59	0.0091					
-15	0.986	0.038	59	0.0100					
-14	0.983	0.040	59	0.0105					
-13	0.975	0.041	59	0.0107					
-12	0.979	0.042	59	0.0109					
-11	0.975	0.045	59	0.0117					
-10	0.971	0.046	59	0.0121					
-9	0.975	0.041	59	0.0107					
-8	0.976	0.045	59	0.0116					
-7	0.979	0.048	59	0.0126					
-6	0.973	0.047	59	0.0123					
-5	0.972	0.051	59	0.0134					
-4	0.970	0.048	59	0.0125					
-3	0.970	0.052	59	0.0136					
-2	0.974	0.052	59	0.0135					
-1	0.963	0.058	59	0.0150					

Table S8 FRET ratio data obtained from Sla2-HP35 FS in wild-type strain and Sla2-HP35 FS in Bbc1 deletion strain. Normalized FRET ratio (Norm FRET ratio in table) was calculated as described in Ratiometric FRET (Materials and methods). Time before vesicle scission (in seconds, Time in table), standard deviation (SD), sample size (n) and 95% confidence interval (CI 95%) are shown. P-value was calculated using two-tailed Welch's t-test.

	Sla2-HP35 FS				Sla2-HP35 FS in Bbc1 deletion				
Time	Norm FRET ratio	SD	n	CI 95%	Norm FRET ratio	SD	n	CI 95%	p-value
-35	0.987	0.053	24	0.023	1.000	0.050	38	0.017	0.3365
-34	0.994	0.055	29	0.021	1.011	0.049	41	0.015	0.1926
-33	1.003	0.043	41	0.013	1.011	0.049	43	0.015	0.4129
-32	0.998	0.041	46	0.012	1.012	0.039	43	0.012	0.0946
-31	0.999	0.043	52	0.012	1.012	0.044	45	0.013	0.1302
-30	0.998	0.046	56	0.012	1.010	0.040	46	0.012	0.1576
-29	1.000	0.039	63	0.010	1.010	0.040	49	0.012	0.1947
-28	1.004	0.034	70	0.008	1.007	0.036	49	0.010	0.6773
-27	1.004	0.029	75	0.007	1.005	0.029	50	0.008	0.7697
-26	1.004	0.029	78	0.006	1.000	0.029	52	0.008	0.4756
-25	0.998	0.030	82	0.007	1.003	0.023	55	0.006	0.3060
-24	1.000	0.026	92	0.005	1.004	0.021	56	0.006	0.3148
-23	0.999	0.022	98	0.004	1.004	0.017	56	0.005	0.1060
-22	0.997	0.020	102	0.004	1.001	0.017	59	0.004	0.1583
-21	0.999	0.017	106	0.003	1.000	0.015	61	0.004	0.6964
-20	1.000	0.023	108	0.004	0.998	0.013	62	0.003	0.3016
-19	1.002	0.026	108	0.005	0.998	0.018	62	0.004	0.2111
-18	1.003	0.025	108	0.005	0.997	0.019	62	0.005	0.0981
-17	1.000	0.027	108	0.005	0.996	0.023	62	0.006	0.2821
-16	1.003	0.034	108	0.006	0.998	0.025	62	0.006	0.3277
-15	0.999	0.036	108	0.007	0.993	0.030	62	0.008	0.2785
-14	0.999	0.033	108	0.006	0.991	0.034	62	0.009	0.1327
-13	0.993	0.039	108	0.007	0.985	0.034	62	0.009	0.1863
-12	0.990	0.041	108	0.008	0.986	0.035	62	0.009	0.4769
-11	0.989	0.045	108	0.009	0.984	0.037	62	0.009	0.4246
-10	0.983	0.047	108	0.009	0.981	0.038	62	0.010	0.7482
-9	0.974	0.045	108	0.009	0.981	0.040	62	0.010	0.2574
-8	0.973	0.049	108	0.009	0.980	0.042	62	0.011	0.2999
-7	0.968	0.044	108	0.008	0.981	0.044	62	0.011	0.0659
-6	0.968	0.050	108	0.010	0.975	0.049	62	0.012	0.3721
-5	0.964	0.051	108	0.010	0.973	0.048	62	0.012	0.2950
-4	0.962	0.053	108	0.010	0.971	0.049	62	0.012	0.2426
-3	0.952	0.049	108	0.009	0.972	0.049	62	0.012	0.0117
-2	0.950	0.051	108	0.010	0.969	0.049	62	0.012	0.0177
-1	0.944	0.055	108	0.011	0.961	0.048	62	0.012	0.0309

Table S9 FRET ratio data obtained from Sla2-HP35 FS under normal conditions and Sla2-HP35 FS after shift to 250 mM sorbitol. Normalized FRET ratio (Norm FRET ratio in table) was calculated as described in Ratiometric FRET (Materials and methods). Time before vesicle scission (in seconds, Time in table), standard deviation (SD), sample size (n) and 95% confidence interval (CI 95%) are shown. P-value was calculated using two-tailed Welch's t-test.

	Sla2-HP35 FS				Sla2-HP35 FS after shift to 250 mM sorbitol				
Time	**Norm FRET ratio**	**SD**	**n**	**CI 95%**	**Norm FRET ratio**	**SD**	**n**	**CI 95%**	**p-value**
-35	0.987	0.053	24	0.023	1.000	0.056	69	0.014	0.3274
-34	0.994	0.055	29	0.021	1.007	0.053	72	0.012	0.2756
-33	1.003	0.043	41	0.013	0.999	0.054	73	0.013	0.6521
-32	0.998	0.041	46	0.012	1.000	0.058	76	0.013	0.8246
-31	0.999	0.043	52	0.012	0.993	0.059	82	0.013	0.5327
-30	0.998	0.046	56	0.012	0.997	0.049	86	0.011	0.9368
-29	1.000	0.039	63	0.010	1.004	0.050	89	0.011	0.5209
-28	1.004	0.034	70	0.008	0.998	0.046	91	0.009	0.3638
-27	1.004	0.029	75	0.007	1.000	0.051	94	0.011	0.6084
-26	1.004	0.029	78	0.006	1.002	0.046	97	0.009	0.7189
-25	0.998	0.030	82	0.007	1.001	0.039	98	0.008	0.6347
-24	1.000	0.026	92	0.005	0.997	0.039	99	0.008	0.5185
-23	0.999	0.022	98	0.004	1.007	0.042	100	0.008	0.0938
-22	0.997	0.020	102	0.004	1.009	0.041	100	0.008	0.0109
-21	0.999	0.017	106	0.003	1.002	0.033	101	0.006	0.5050
-20	1.000	0.023	108	0.004	1.000	0.035	101	0.007	0.8376
-19	1.002	0.026	108	0.005	0.995	0.034	101	0.007	0.0876
-18	1.003	0.025	108	0.005	0.996	0.035	101	0.007	0.0793
-17	1.000	0.027	108	0.005	0.995	0.036	101	0.007	0.2382
-16	1.003	0.034	108	0.006	0.998	0.049	101	0.010	0.3895
-15	0.999	0.036	108	0.007	0.999	0.050	101	0.010	0.9415
-14	0.999	0.033	108	0.006	0.995	0.049	101	0.010	0.5410
-13	0.993	0.039	108	0.007	0.986	0.048	101	0.009	0.2342
-12	0.990	0.041	108	0.008	0.985	0.053	101	0.010	0.4435
-11	0.989	0.045	108	0.009	0.989	0.043	101	0.008	0.9123
-10	0.983	0.047	108	0.009	0.991	0.048	101	0.010	0.2173
-9	0.974	0.045	108	0.009	0.987	0.050	101	0.010	0.0363
-8	0.973	0.049	108	0.009	0.988	0.055	101	0.011	0.0389
-7	0.968	0.044	108	0.008	0.986	0.050	101	0.010	0.0056
-6	0.968	0.050	108	0.010	0.986	0.053	101	0.010	0.0154
-5	0.964	0.051	108	0.010	0.975	0.049	101	0.010	0.1230
-4	0.962	0.053	108	0.010	0.979	0.054	101	0.011	0.0197
-3	0.952	0.049	108	0.009	0.975	0.055	101	0.011	0.0014
-2	0.950	0.051	108	0.010	0.971	0.057	101	0.011	0.0050
-1	0.944	0.055	108	0.011	0.965	0.062	101	0.012	0.0102

Table S10 FRET ratio data obtained from Sla2-HP35 FS under normal conditions and Sla2-HP35 FS after shift to 500 mM sorbitol. Normalized FRET ratio (Norm FRET ratio in table) was calculated as described in Ratiometric FRET (Materials and methods). Time before vesicle scission (in seconds, Time in table), standard deviation (SD), sample size (n) and 95% confidence interval (CI 95%) are shown. P-value was calculated using two-tailed Welch's t-test.

	Sla2-HP35 FS				Sla2-HP35 FS after shift to 500 mM sorbitol				
Time	Norm FRET ratio	SD	n	CI 95%	Norm FRET ratio	SD	n	CI 95%	p-value
-35	0.987	0.053	24	0.023	0.991	0.070	53	0.019	0.7676
-34	0.994	0.055	29	0.021	0.984	0.060	61	0.015	0.4392
-33	1.003	0.043	41	0.013	0.999	0.063	65	0.016	0.6814
-32	0.998	0.041	46	0.012	0.998	0.053	66	0.013	0.9836
-31	0.999	0.043	52	0.012	0.984	0.052	66	0.013	0.0955
-30	0.998	0.046	56	0.012	1.004	0.047	66	0.011	0.4339
-29	1.000	0.039	63	0.010	0.995	0.057	69	0.014	0.5600
-28	1.004	0.034	70	0.008	0.997	0.042	70	0.010	0.2612
-27	1.004	0.029	75	0.007	0.999	0.053	71	0.013	0.5535
-26	1.004	0.029	78	0.006	0.995	0.048	71	0.011	0.1811
-25	0.998	0.030	82	0.007	1.004	0.049	75	0.011	0.4397
-24	1.000	0.026	92	0.005	1.000	0.041	77	0.009	0.9947
-23	0.999	0.022	98	0.004	1.003	0.039	79	0.009	0.3812
-22	0.997	0.020	102	0.004	0.990	0.042	80	0.009	0.1573
-21	0.999	0.017	106	0.003	0.993	0.032	80	0.007	0.1331
-20	1.000	0.023	108	0.004	0.998	0.038	80	0.008	0.6136
-19	1.002	0.026	108	0.005	1.001	0.041	80	0.009	0.8319
-18	1.003	0.025	108	0.005	1.007	0.042	80	0.009	0.4176
-17	1.000	0.027	108	0.005	1.004	0.041	80	0.009	0.4452
-16	1.003	0.034	108	0.006	0.996	0.044	80	0.010	0.2604
-15	0.999	0.036	108	0.007	0.997	0.047	80	0.011	0.7270
-14	0.999	0.033	108	0.006	1.000	0.046	80	0.010	0.8432
-13	0.993	0.039	108	0.007	1.006	0.048	80	0.011	0.0460
-12	0.990	0.041	108	0.008	0.994	0.056	80	0.013	0.6048
-11	0.989	0.045	108	0.009	0.996	0.049	80	0.011	0.3334
-10	0.983	0.047	108	0.009	0.992	0.054	80	0.012	0.2404
-9	0.974	0.045	108	0.009	0.993	0.051	80	0.011	0.0067
-8	0.973	0.049	108	0.009	0.993	0.051	80	0.011	0.0081
-7	0.968	0.044	108	0.008	0.984	0.057	80	0.013	0.0390
-6	0.968	0.050	108	0.010	0.978	0.051	80	0.011	0.2000
-5	0.964	0.051	108	0.010	0.980	0.061	80	0.014	0.0704
-4	0.962	0.053	108	0.010	0.981	0.060	80	0.013	0.0237
-3	0.952	0.049	108	0.009	0.974	0.060	80	0.013	0.0077
-2	0.950	0.051	108	0.010	0.961	0.063	80	0.014	0.2110
-1	0.944	0.055	108	0.011	0.955	0.059	80	0.013	0.1999

Table S11 FRET ratio data obtained from Sla2-HP35 FS in 0.1% DMSO and Sla2-HP35 FS in 5 µM PalmC, 0.1% DMSO. Normalized FRET ratio (Norm FRET ratio in table) was calculated as described in Ratiometric FRET (Materials and methods). Time before vesicle scission (in seconds, Time in table), standard deviation (SD), sample size (n) and 95% confidence interval (CI 95%) are shown. P-value was calculated using two-tailed Welch's t-test.

	Sla2-HP35 FS in 0.1% DMSO				Sla2-HP35 FS in 5 µM PalmC, 0.1% DMSO				
Time	Norm FRET ratio	SD	n	CI 95%	Norm FRET ratio	SD	n	CI 95%	p-value
-35	0.990	0.062	61	0.016	0.984	0.064	63	0.016	0.6139
-34	0.987	0.051	65	0.013	1.001	0.059	66	0.014	0.1709
-33	0.992	0.061	65	0.015	0.980	0.062	71	0.015	0.2486
-32	0.995	0.055	65	0.014	0.985	0.063	74	0.015	0.3256
-31	0.999	0.051	67	0.013	0.994	0.063	75	0.015	0.6135
-30	0.994	0.051	70	0.012	0.990	0.054	76	0.012	0.6364
-29	1.000	0.049	71	0.012	0.989	0.058	81	0.013	0.2226
-28	1.001	0.046	72	0.011	0.995	0.058	82	0.013	0.4602
-27	0.992	0.052	73	0.012	0.987	0.062	85	0.013	0.5939
-26	0.992	0.055	75	0.013	0.993	0.054	89	0.011	0.9619
-25	0.992	0.049	75	0.011	0.999	0.052	92	0.011	0.3809
-24	0.994	0.044	80	0.010	0.991	0.047	96	0.009	0.7106
-23	0.994	0.033	82	0.007	0.989	0.040	96	0.008	0.3459
-22	1.000	0.039	85	0.008	0.998	0.044	97	0.009	0.7245
-21	1.009	0.042	85	0.009	1.001	0.045	99	0.009	0.1919
-20	1.002	0.037	87	0.008	0.998	0.044	99	0.009	0.5249
-19	1.000	0.046	87	0.010	1.010	0.041	99	0.008	0.1199
-18	1.003	0.043	87	0.009	1.006	0.050	99	0.010	0.7132
-17	1.005	0.045	87	0.010	1.008	0.050	99	0.010	0.6077
-16	0.996	0.042	87	0.009	1.004	0.058	99	0.011	0.2470
-15	1.002	0.048	87	0.010	1.001	0.056	99	0.011	0.9154
-14	1.002	0.056	87	0.012	0.999	0.053	99	0.011	0.7631
-13	0.993	0.042	87	0.009	1.001	0.061	99	0.012	0.3326
-12	0.987	0.052	87	0.011	0.992	0.053	99	0.011	0.5119
-11	0.998	0.057	87	0.012	0.995	0.062	99	0.012	0.7148
-10	0.992	0.053	87	0.011	0.996	0.069	99	0.014	0.5956
-9	0.983	0.053	87	0.011	0.987	0.068	99	0.013	0.7286
-8	0.983	0.050	87	0.011	0.988	0.060	99	0.012	0.5973
-7	0.979	0.061	87	0.013	0.987	0.063	99	0.013	0.3824
-6	0.975	0.061	87	0.013	0.985	0.057	99	0.011	0.2618
-5	0.971	0.060	87	0.013	0.996	0.071	99	0.014	0.0111
-4	0.966	0.068	87	0.015	0.988	0.077	99	0.015	0.0391
-3	0.957	0.065	87	0.014	0.986	0.070	99	0.014	0.0037
-2	0.956	0.061	87	0.013	0.988	0.071	99	0.014	0.0011
-1	0.955	0.068	87	0.015	0.971	0.071	99	0.014	0.1032

Table S12 FRET ratio data obtained from Sla2-HP35st FS in 1 M sorbitol and Sla2-HP35st FS after shift from 1 to 0.5 M sorbitol. Normalized FRET ratio (Norm FRET ratio in table) was calculated as described in Ratiometric FRET (Materials and methods). Time before vesicle scission (in seconds, Time in table), standard deviation (SD), sample size (n) and 95% confidence interval (CI 95%) are shown. P-value was calculated using two-tailed Welch's t-test.

	Sla2-HP35st FS in 1 M sorbitol				Sla2-HP35st FS after shift from 1 to 0.5 M sorbitol				
Time	Norm FRET ratio	SD	n	CI 95%	Norm FRET ratio	SD	n	CI 95%	p-value
-35	0.988	0.065	46	0.019	0.985	0.071	39	0.023	0.8244
-34	0.991	0.058	46	0.017	0.999	0.059	40	0.019	0.5261
-33	0.999	0.059	48	0.017	0.989	0.057	40	0.018	0.4472
-32	0.997	0.064	48	0.018	1.005	0.055	41	0.017	0.5723
-31	0.990	0.049	49	0.014	0.998	0.059	43	0.018	0.4600
-30	1.003	0.046	54	0.013	0.995	0.059	44	0.018	0.4857
-29	1.006	0.050	56	0.013	1.002	0.063	46	0.019	0.7461
-28	0.993	0.052	57	0.014	0.998	0.046	47	0.013	0.6319
-27	1.007	0.052	58	0.014	0.993	0.057	50	0.016	0.1723
-26	1.006	0.048	59	0.013	0.993	0.053	52	0.015	0.1646
-25	1.006	0.047	59	0.012	0.996	0.043	55	0.012	0.2399
-24	0.997	0.043	61	0.011	0.991	0.042	55	0.011	0.4673
-23	1.001	0.042	62	0.011	0.993	0.039	56	0.010	0.2521
-22	0.988	0.042	63	0.011	1.007	0.045	57	0.012	0.0177
-21	1.000	0.041	63	0.010	1.003	0.040	60	0.010	0.6303
-20	0.994	0.046	64	0.011	1.000	0.041	61	0.010	0.4594
-19	1.005	0.046	64	0.012	1.003	0.043	61	0.011	0.7190
-18	0.999	0.041	64	0.010	0.996	0.044	61	0.011	0.6688
-17	1.010	0.046	64	0.011	1.010	0.055	61	0.014	0.9611
-16	0.998	0.051	64	0.013	0.994	0.052	61	0.013	0.6741
-15	0.993	0.065	64	0.016	0.994	0.056	61	0.014	0.9488
-14	0.999	0.062	64	0.015	0.996	0.046	61	0.012	0.7487
-13	0.989	0.061	64	0.015	0.998	0.052	61	0.013	0.3873
-12	0.990	0.053	64	0.013	1.007	0.057	61	0.015	0.0864
-11	0.984	0.062	64	0.015	0.999	0.059	61	0.015	0.1731
-10	0.986	0.063	64	0.016	1.001	0.067	61	0.017	0.2058
-9	0.982	0.070	64	0.018	0.986	0.055	61	0.014	0.7358
-8	0.978	0.068	64	0.017	0.984	0.058	61	0.015	0.5876
-7	0.990	0.061	64	0.015	0.993	0.061	61	0.016	0.7837
-6	0.974	0.066	64	0.016	0.973	0.064	61	0.016	0.9629
-5	0.966	0.065	64	0.016	0.964	0.063	61	0.016	0.8706
-4	0.964	0.067	64	0.017	0.974	0.071	61	0.018	0.4036
-3	0.964	0.061	64	0.015	0.961	0.060	61	0.015	0.8167
-2	0.964	0.073	64	0.018	0.978	0.065	61	0.017	0.2471
-1	0.959	0.073	64	0.018	0.961	0.063	61	0.016	0.8962

Table S13 FRET ratio data obtained from Sla2-HP35st FS in 1 M sorbitol and Sla2-HP35st FS after shift from 1 to 0.4 M sorbitol. Normalized FRET ratio (Norm FRET ratio in table) was calculated as described in Ratiometric FRET (Materials and methods). Time before vesicle scission (in seconds, Time in table), standard deviation (SD), sample size (n) and 95% confidence interval (CI 95%) are shown. P-value was calculated using two-tailed Welch's t-test.

	Sla2-HP35st FS in 1 M sorbitol				Sla2-HP35st FS after shift from 1 to 0.4 M sorbitol				
Time	Norm FRET ratio	SD	n	CI 95%	Norm FRET ratio	SD	n	CI 95%	p-value
-35	0.988	0.065	46	0.019	0.993	0.068	45	0.020	0.7398
-34	0.991	0.058	46	0.017	1.005	0.072	49	0.021	0.3168
-33	0.999	0.059	48	0.017	1.001	0.064	52	0.018	0.8614
-32	0.997	0.064	48	0.018	1.008	0.077	54	0.021	0.4279
-31	0.990	0.049	49	0.014	0.999	0.064	54	0.018	0.4027
-30	1.003	0.046	54	0.013	1.009	0.070	57	0.019	0.6008
-29	1.006	0.050	56	0.013	0.991	0.077	59	0.020	0.2151
-28	0.993	0.052	57	0.014	0.993	0.066	61	0.017	0.9847
-27	1.007	0.052	58	0.014	0.986	0.072	63	0.018	0.0619
-26	1.006	0.048	59	0.013	0.991	0.067	63	0.017	0.1620
-25	1.006	0.047	59	0.012	0.995	0.046	65	0.011	0.1925
-24	0.997	0.043	61	0.011	0.999	0.051	65	0.013	0.8738
-23	1.001	0.042	62	0.011	0.993	0.036	66	0.009	0.2154
-22	0.988	0.042	63	0.011	1.002	0.040	67	0.010	0.0458
-21	1.000	0.041	63	0.010	0.993	0.042	67	0.010	0.3919
-20	0.994	0.046	64	0.011	1.004	0.040	70	0.009	0.1952
-19	1.005	0.046	64	0.012	1.003	0.043	72	0.010	0.8004
-18	0.999	0.041	64	0.010	1.003	0.043	72	0.010	0.6202
-17	1.010	0.046	64	0.011	1.007	0.044	72	0.010	0.7250
-16	0.998	0.051	64	0.013	1.007	0.056	72	0.013	0.3246
-15	0.993	0.065	64	0.016	1.003	0.061	72	0.014	0.3639
-14	0.999	0.062	64	0.015	1.006	0.064	72	0.015	0.5108
-13	0.989	0.061	64	0.015	0.995	0.064	72	0.015	0.5634
-12	0.990	0.053	64	0.013	0.999	0.060	72	0.014	0.3383
-11	0.984	0.062	64	0.015	0.990	0.072	72	0.017	0.6131
-10	0.986	0.063	64	0.016	1.002	0.074	72	0.017	0.1799
-9	0.982	0.070	64	0.018	0.999	0.067	72	0.016	0.1449
-8	0.978	0.068	64	0.017	0.982	0.069	72	0.016	0.7184
-7	0.990	0.061	64	0.015	0.986	0.075	72	0.018	0.7873
-6	0.974	0.066	64	0.016	0.979	0.078	72	0.018	0.6580
-5	0.966	0.065	64	0.016	0.958	0.068	72	0.016	0.4900
-4	0.964	0.067	64	0.017	0.972	0.070	72	0.016	0.4917
-3	0.964	0.061	64	0.015	0.956	0.074	72	0.017	0.5289
-2	0.964	0.073	64	0.018	0.944	0.077	72	0.018	0.1361
-1	0.959	0.073	64	0.018	0.945	0.075	72	0.018	0.2764

Table S14 FRET ratio data obtained from Sla2-HP35 FS in 1 M sorbitol and Sla2-HP35 FS after shift from 1 to 0.5 M sorbitol. Normalized FRET ratio (Norm FRET ratio in table) was calculated as described in Ratiometric FRET (Materials and methods). Time before vesicle scission (in seconds, Time in table), standard deviation (SD), sample size (n) and 95% confidence interval (CI 95%) are shown. P-value was calculated using two-tailed Welch's t-test.

	Sla2-HP35 FS in 1 M sorbitol				Sla2-HP35 FS after shift from 1 to 0.5 M sorbitol				
TIME	Norm FRET ratio	SD	n	CI 95%	Norm FRET ratio	SD	n	CI 95%	p-value
-35	1.000	0.070	56	0.019	0.982	0.060	44	0.018	0.1908
-34	0.991	0.056	61	0.014	0.995	0.068	48	0.020	0.7459
-33	0.993	0.057	62	0.014	0.999	0.055	50	0.016	0.5786
-32	0.999	0.056	63	0.014	0.982	0.051	50	0.015	0.0957
-31	1.000	0.050	65	0.012	0.991	0.059	52	0.017	0.3756
-30	0.995	0.061	67	0.015	0.995	0.057	54	0.016	0.9888
-29	0.996	0.051	68	0.012	0.989	0.054	55	0.015	0.5055
-28	0.997	0.050	72	0.012	1.009	0.059	56	0.016	0.2141
-27	1.005	0.056	73	0.013	1.003	0.053	56	0.014	0.8500
-26	1.014	0.064	76	0.015	1.002	0.041	56	0.011	0.1813
-25	1.006	0.044	78	0.010	1.010	0.048	58	0.013	0.5873
-24	1.005	0.043	78	0.010	0.996	0.037	59	0.010	0.1873
-23	0.991	0.036	78	0.008	0.997	0.039	60	0.010	0.3659
-22	1.004	0.039	80	0.009	1.000	0.042	60	0.011	0.5657
-21	1.004	0.037	80	0.008	1.000	0.033	62	0.008	0.4713
-20	0.992	0.040	81	0.009	0.997	0.045	62	0.011	0.5252
-19	0.997	0.044	81	0.010	1.002	0.045	62	0.011	0.4661
-18	0.995	0.035	81	0.008	1.002	0.044	62	0.011	0.2607
-17	1.006	0.046	81	0.010	0.996	0.041	62	0.010	0.1575
-16	1.001	0.046	81	0.010	1.005	0.053	62	0.013	0.6736
-15	1.005	0.056	81	0.012	1.008	0.047	62	0.012	0.7554
-14	0.995	0.049	81	0.011	1.007	0.055	62	0.014	0.1730
-13	0.995	0.057	81	0.013	0.996	0.057	62	0.014	0.8561
-12	0.999	0.054	81	0.012	1.001	0.057	62	0.014	0.8319
-11	1.005	0.058	81	0.013	1.002	0.054	62	0.014	0.7578
-10	0.991	0.058	81	0.013	0.983	0.060	62	0.015	0.3929
-9	1.000	0.071	81	0.016	0.988	0.056	62	0.014	0.2766
-8	0.982	0.061	81	0.013	0.981	0.059	62	0.015	0.8997
-7	0.982	0.058	81	0.013	0.986	0.058	62	0.015	0.6684
-6	0.982	0.060	81	0.013	0.990	0.064	62	0.016	0.4136
-5	0.969	0.063	81	0.014	0.970	0.064	62	0.016	0.9137
-4	0.965	0.056	81	0.012	0.971	0.068	62	0.017	0.5865
-3	0.970	0.062	81	0.014	0.967	0.065	62	0.016	0.7676
-2	0.970	0.076	81	0.017	0.968	0.071	62	0.018	0.8973
-1	0.949	0.075	81	0.017	0.959	0.074	62	0.019	0.4326